



**AFRL-RZ-WP-TR-2009-2111**

## **PROPULSION AND POWER RAPID RESPONSE R&D SUPPORT**

**Task Order 0006 : Engineering Research, Testing, and  
Technical Analyses of Advanced Propulsion Combustion  
Concepts, Mechanical Systems, Lubricants and Fuels :  
Mechanical Systems**

**James K. Klein**

**Klein Consulting, LLC**

**FEBRUARY 2009**

**Approved for public release; distribution unlimited.**

*See additional restrictions described on inside pages*

**STINFO COPY**

**AIR FORCE RESEARCH LABORATORY  
PROPULSION DIRECTORATE  
WRIGHT-PATTERSON AIR FORCE BASE, OH 45433-7251  
AIR FORCE MATERIEL COMMAND  
UNITED STATES AIR FORCE**

## NOTICE AND SIGNATURE PAGE

Using Government drawings, specifications, or other data included in this document for any purpose other than Government procurement does not in any way obligate the U.S. Government. The fact that the Government formulated or supplied the drawings, specifications, or other data does not license the holder or any other person or corporation; or convey any rights or permission to manufacture, use, or sell any patented invention that may relate to them.

This report was cleared for public release by the Wright-Patterson Public Affairs Office and is available to the general public, including foreign nationals. Copies may be obtained from the Defense Technical Information Center (DTIC) (<http://www.dtic.mil>).

AFRL-RZ-WP-TR-2009-2111 HAS BEEN REVIEWED AND IS APPROVED FOR PUBLICATION IN ACCORDANCE WITH THE ASSIGNED DISTRIBUTION STATEMENT.

                    // s //                      
DR. JAMES T. EDWARDS  
AFRL/RZPF

                    // s //                      
JERMONT CHEN, Maj., USAF  
AFRL/RZPF

This report is published in the interest of scientific and technical information exchange, and its publication does not constitute the Government's approval or disapproval of its ideas or findings.

\*Disseminated copies will show “//signature//” stamped or typed above the signature blocks.

REPORT DOCUMENTATION PAGE				Form Approved OMB No. 0704-0188	
<p>The public reporting burden for this collection of information is estimated to average 1 hour per response, including the time for reviewing instructions, searching existing data sources, gathering and maintaining the data needed, and completing and reviewing the collection of information. Send comments regarding this burden estimate or any other aspect of this collection of information, including suggestions for reducing this burden, to Department of Defense, Washington Headquarters Services, Directorate for Information Operations and Reports (0704-0188), 1215 Jefferson Davis Highway, Suite 1204, Arlington, VA 22202-4302. Respondents should be aware that notwithstanding any other provision of law, no person shall be subject to any penalty for failing to comply with a collection of information if it does not display a currently valid OMB control number. <b>PLEASE DO NOT RETURN YOUR FORM TO THE ABOVE ADDRESS.</b></p>					
1. REPORT DATE (DD-MM-YY) February 2009		2. REPORT TYPE Interim		3. DATES COVERED (From - To) 27 May 2003 – 27 Nov 2008	
4. TITLE AND SUBTITLE PROPULSION AND POWER RAPID RESPONSE R&D SUPPORT  Task Order 0006 : Engineering Research, Testing, and Technical Analyses of Advanced Propulsion Combustion Concepts, Mechanical Systems, Lubricants and Fuels : Mechanical Systems				5a. CONTRACT NUMBER F33615-02-D-2299-0006	
				5b. GRANT NUMBER	
				5c. PROGRAM ELEMENT NUMBER 62203F	
6. AUTHOR(S) James K. Klein				5d. PROJECT NUMBER 3048	
				5e. TASK NUMBER 05	
				5f. WORK UNIT NUMBER 30480506	
7. PERFORMING ORGANIZATION NAME(S) AND ADDRESS(ES) <div style="display: flex; justify-content: space-between;"> <div style="width: 45%;"> Klein Consulting, LLC  4479 E. Helenwood Drive  Beavercreek, OH 45431 </div> <div style="width: 45%;"> Universal Technology Corporation  1270 N. Fairfield Road  Dayton, OH 45432-2600 </div> </div>				8. PERFORMING ORGANIZATION REPORT NUMBER	
9. SPONSORING/MONITORING AGENCY NAME(S) AND ADDRESS(ES) Air Force Research Laboratory Propulsion Directorate Wright-Patterson Air Force Base, OH 45433-7251 Air Force Materiel Command United States Air Force				10. SPONSORING/MONITORING AGENCY ACRONYM(S) AFRL/RZPF	
				11. SPONSORING/MONITORING AGENCY REPORT NUMBER(S) AFRL-RZ-WP-TR-2009-2111	
12. DISTRIBUTION/AVAILABILITY STATEMENT Approved for public release; distribution unlimited.					
13. SUPPLEMENTARY NOTES Technical paper contains color. This report is also published as Appendix E to AFRL-RZ-WP-TR-2009-2050 PAO Case Number and clearance date: 88ABW2009-2166, 22 May 2009.					
14. ABSTRACT The objective of this delivery order was to fully support and accomplish research and development, planning, program management, test and analyses of advanced combustion concepts, mechanical systems, lubricants and fuels for aerospace propulsion and power programs for the Air Force Research Laboratory (AFRL)					
15. SUBJECT TERMS Foil bearing, bearing performance, ball-raceway spall interaction, ball bearing dynamics					
16. SECURITY CLASSIFICATION OF:			17. LIMITATION OF ABSTRACT: SAR	18. NUMBER OF PAGES 158	19a. NAME OF RESPONSIBLE PERSON (Monitor) Dr. James T. Edwards 19b. TELEPHONE NUMBER (Include Area Code) N/A
a. REPORT Unclassified	b. ABSTRACT Unclassified	c. THIS PAGE Unclassified			

## TABLE OF CONTENTS

<b><u>Section</u></b>	<b><u>Page</u></b>
1.0 Summary .....	1
2.0 Introduction.....	2
3.0 Methods, Assumptions, and Procedures .....	3
4.0 Results and Discussions.....	4
4.1 Identification of Stiffness & Damping Coefficients in Foil Bearings .....	4
4.2 Numerical Analysis of Bearing Performance and Power Loss.....	4
4.3 Ball Bearing Dynamics as Affected by Raceway Defects.....	4
4.4 Determination of Ball-Raceway Spall Integration Forces Using ADORE and Ball- Raceway Stresses Using FEA in Hybrid Bearings .....	4
5.0 Conclusions.....	5
6.0 Recommendations.....	6



## **PREFACE**

This report was prepared by the Universal Technology Corporation (UTC), 1270 North Fairfield Road, Dayton, Ohio, 45432-2600 under Contract Number F33615-02-D-2299 with the Air Force Research Laboratory's Propulsion Directorate (AFRL/RZ). Mrs. Michele Puterbaugh (Contractor, UTC) was the project manager for this effort. Mr. James K. Klein (Contractor, UTC) was the technical team leader. The research reported herein covers the period of 27 May 2003 through 27 November 2008. This effort was funded by the Air Force Research Laboratory.

## **ACKNOWLEDGEMENTS**

The authors would like to acknowledge the support of a number of individuals who made it possible to obtain the data and results described in this report:

Mrs. Tonita Hudson (UTC)

Mrs. Kim Rhoads (UTC)

Mr. Mike Hoeprich (The Timken Company)

Dr. Luis San Andres (Texas A&M University)

Mr. Lyn Greenhill (DynaTech Engineering, Inc.)

Dr. Pradeep Gupta (PKG Inc.)

Mr. Joseph V. Poplawski, (J.V. Poplawski & Associates)

Dr. Farshid Sadeghi, (Purdue University)

Professor Jane Wang, (Northwestern University)

Mr. Charles Grott, (EDS PLM Solutions)

Dr. James Bielk, (Concepts NREC Product Center)

Mr. Alex Krulikowski, (GM Powertrain)

Mr. Anthony Breedlove, (Texas A&M University)

Mr. Bradley Pederson, (Purdue University)

## 1.0 SUMMARY

This report is a compilation of four separate studies accomplished under subcontract to UTC. The four subcontractors include Texas A&M University, Purdue University, Dr. Pradeep Gupta (PKG Inc), and the University of Florida. Summaries for each of the four studies is reported below:

- (1) The objective of the first study conducted by Texas A&M University was to measure the (bump) structure deflections for increasing applied static loads on a foil gas bearing (FB) and to estimate the static stiffness of the whole FB with and without a shaker connection. Displacement versus static force testing was performed and data is reported.
- (2) The objective of the second study conducted by Purdue University was to investigate bearing performance and power loss for various cage, race and rolling element materials. The investigation focused on the power loss at the race-to-cage and ball-to-cage contacts. Power loss parameters and bearing element state data are provided.
- (3) The objective of the third study conducted by PKG, Inc. was to conduct geometric modeling of race defects. ADORE software was used as the baseline tool. Results, (defect, heat generation ratio, and cage wear ratio) were tabulated and were reported in a presentation type final report.
- (4) The objective of the fourth study conducted by the University of Florida was to model the elastic-plastic stress field associated with the loaded region undergoing spall propagation using 3D FEA and gain a mechanistic understanding of the damage evolution due to RCF in the spall region. 3D FE stress analysis in the spall neighborhood, simplified trailing edge impact stress analysis, dynamic finite element impact analysis of the ball with the spall edge using ABAQUS Explicit, and spall propagation testing was accomplished; results and hypotheses are reported.

## **2.0 INTRODUCTION**

This Research and Development (R&D) report summarizes the work performed by the Universal Technology Corporation (UTC) toward achieving the objectives of contract F33615-02-D-2299, Propulsion and Power Rapid Response R&D Support for the Air Force Research Laboratory Mechanical Systems Branch, (AFRL/RZTM). The objective of this delivery order was to fully support and accomplish research and development, planning, program management, test and analyses of advanced combustion concepts, mechanical systems, lubricants and fuels for aerospace propulsion and power programs, applications, and systems.

The Virtual Machine Design Workshop held at Purdue University in West Lafayette, IN during the period of August 5, 2003 through August 6, 2003 was supported by UTC through letter agreements with the 10 speakers. In addition, four subcontractor efforts were issued for ball bearing and raceway research. These studies have been successfully completed and are provided as appendices to this report.

### **3.0 METHODS, ASSUMPTIONS, AND PROCEDURES**

UTC accomplished this work effort using on-site and off-site contractors and subcontractors possessing expert qualifications in the various technical areas to be explored. Extensive use was made of widely available project management and systems engineering standards, tools and methodologies, including ADORE software. Progress towards completing the various study objectives was carefully tracked through the use of monthly reports. Close coordination with Government Program Managers and suppliers was maintained throughout the period of performance to ensure delivery schedules were met.

## **4.0 RESULTS AND DISCUSSIONS**

The Universal Technology Corporation (UTC) and their subcontractors accomplished and supported a variety of research studies and research projects related to mechanical systems. The following discussion is organized by activity and project.

### **4.1 Identification of Stiffness & Damping Coefficients in Foil Bearings**

The Texas Engineering Experiment Station of Texas A&M University accomplished research to characterize quantitatively (gas) foil bearing rotordynamic performance, reliability, and durability. Reliable methods for identification of stiffness and equivalent (viscous) damping force coefficients in foil gas bearings (FB) were developed. Rotor imbalance response tests to extract the equivalent stiffness and (viscous) damping coefficients of the test FBs were conducted. The experimentally identified FB force coefficients to predictions derived from a parallel computational analysis effort were correlated. This study is provided as Appendix A.

### **4.2 Numerical Analysis of Bearing Performance and Power Loss**

Purdue University conducted an investigation of the bearing performance and power loss of a specified bearing geometry that was to be tested in the AFRL/PRTM High Mach# Engine bearing test facility using the subcontractor's bearing analysis software tools. The effect of several factors including cage material, ball material, and lubricant for various bearing load and speed conditions were evaluated. This study is provided as Appendix B.

### **4.3 Ball Bearing Dynamics as Affected by Raceway Defects**

Dr. Pradeep K. Gupta (PKG Inc.), provided R&D support to AFRL/PZTM with an investigation involving ball bearing dynamics as affected by raceway defects. A geometrical model for a raceway defect for use with ADORE software was developed and tested. Test cases to confirm proper operation of the model were evaluated and a presentation type report was presented to the Air Force Laboratories at Wright-Patterson Air Force Base, Ohio. This study is provided as Appendix C.

### **4.4 Determination of Ball-Raceway Spall Integration Forces Using ADORE and Ball-Raceway Stresses Using FEA in Hybrid Bearings**

The University of Florida, conducted a research investigation involving ball-raceway spall interaction forces and ball-raceway stresses. This work included acquisition of the rolling-element bearing dynamics program from ADORE, Inc, and modeling of AFRL's 40-mm test hybrid bearing using ADORE. The kinematics and kinetics of ball-raceway spall interaction was modeled. This study is provided as Appendix D.

## **5.0 CONCLUSIONS**

Comprehensive investigations of bearing performance and power loss, foil bearing stiffness, ball-raceway spall interaction and ball bearing dynamics have been completed and numerical methods developed. Specific conclusions for each study are provided in the appropriate appendices.

## **6.0 RECOMMENDATIONS**

Further investigations with additional and expanded correlations, parametric evaluations and life modeling are recommended in the appropriate appendices.



**APPENDIX A**  
**Texas A&M University Contribution**

Mechanical Engineering Department  
Texas A&M University

# **Estimation of Static Structural Stiffness in a Bump Type Foil Bearing**

**Final Technical Progress Report**  
**To**  
***Universal Technology Corp.***

by  
Anthony Breedlove  
Research Assistant  
Revised  
Luis San Andrés  
Principal Investigator  
May 31, 2005

TEES Project # 32525/21960/ME

**IDENTIFICATION OF STIFFNESS AND DAMPING COEFFICIENTS IN FOIL BEARINGS**

# **Estimation of Static Structural Stiffness in a Bump Type Foil Bearing**

## ***Executive Summary***

Static load test results and analysis for the estimation of the structural stiffness in a bump-type foil gas bearing (FB) follow. The FB is 38.1 mm in axial length and inner diameter. There is a radial clearance between shaft and inner diameter of test shaft. The Teflon-coated (0.10 mm) top foil rests on 25 structural bumps, whose nominal height and pitch equal 0.38 mm and 4.57 mm, respectively.

The objective is to measure the (bump) structure deflections for increasing applied static loads on the *FB*, and to estimate the static stiffness of the whole *FB* with and without a shaker connection. The load and displacements are recorded using an eddy current sensor and a hand held dynamometer. The derived static stiffness should be a benchmark for later experiments to be conducted with a periodic load over a frequency range.

Bearing displacements were recorded for applied loads up to 44 N (10 lb). Loading and unloading test data showed hysteresis. The relationship between load and structural deflection is nonlinear with a typical hardening effect as the deflection increases. The estimated structural stiffness of the bearing increases greatly as the *FB* deflection increases. Tests conducted with loads oriented away from the top foil spot weld (0°) and 90° away reveal different stiffness magnitudes. At low loads, the *FB* is very soft due to the large initial clearance. The identified *FB* structural stiffnesses, over a range of bearing deflections, do not reproduce values determined in a prior effort [2] due to test set up limitations and human error.

## ***Table of Contents***

	<u>page</u>
Executive Summary .....	i
List of Figures .....	iii
List of Tables .....	iii
Nomenclature .....	iv
 Introduction .....	 1
Test Procedure .....	2
Experimental Results .....	3
Preliminary conclusions .....	14
References .....	14
Appendix A. Uncertainty Analysis .....	15
Appendix B. Precision Limit of the Mean of the Trials .....	16

## List of Figures

	<u>page</u>
Figure 1 Schematic view of test foil bearing .....	1
Figure 2 Test set up for static loading of foil bearing.....	2
Figure 3 Foil bearing displacement versus applied static load for tests with shaker attached at 0° position .....	4
Figure 4 Foil bearing displacement versus applied static load for tests without shaker attached at 0° position .....	4
Figure 5 Foil bearing displacement versus applied static load for tests with shaker attached at 90° position .....	5
Figure 6 Bearing Foil bearing displacement versus applied static load for tests without shaker attached at 90° position.....	5
Figure 7 Estimated foil bearing structural stiffness versus displacement. Test case: bearing with shaker attached, 0° position.....	8
Figure 8 Estimated foil bearing structural stiffness versus displacement. Test case: bearing without shaker attached, 0° position .....	8
Figure 9 Estimated foil bearing structural stiffness versus displacement. Test case: bearing with shaker attached, 90° position .....	9
Figure 10 Estimated foil bearing structural stiffness versus displacement. Test case: bearing without shaker attached, 90° position .....	9
Figure 11 Applied force versus bearing displacement and third-order polynomial fit for Trial 3 of 0° Position .....	12
Figure 12 Applied force versus bearing displacement and third-order polynomial fit Trial 3 of 90° Position.....	12

## List of Tables

Table 1 Curve fit equations for force as a function of displacement for four load cases – Loading condition only.....	7
Table 2 Structural stiffness derived from displacement vs force measurements .....	7
Table 3 Deflection and structural stiffness data for the 0° and 90° positions. Taken from [2] .....	10
Table 4 Present deflection and structural stiffness data for the 0° and 90° positions, without shaker attached, Trial 3 of each case .....	11
Table 5 FB structural stiffness at 22.3 N and 44.5 N for four test cases.....	13
Table 6 Tabulated average values of structural stiffness and precision limit intervals for two static loads .....	13
Table 7 Estimated FB structural stiffness at 44.5 N load, one with highest correlation coefficient and one with maximum magnitude for each test case.....	14

## ***Nomenclature***

$F$	Static load [N]
$G$	Gain of eddy current sensor [mV/ $\mu\text{m}$ ]
$k$	Estimated bearing stiffness [N/ $\mu\text{m}$ ]
$\bar{k}$	Average (mean) of stiffness values [N/ $\mu\text{m}$ ]
$k_i$	i-th sample of estimated bearing stiffness [N/ $\mu\text{m}$ ]
$L$	Loading portion of test cycle
$N$	Number of stiffness samples
$P_k$	Precision limit of the average (mean) of the stiffness values [N/ $\mu\text{m}$ ]
$S_k$	Precision index of the stiffness sample population [N/ $\mu\text{m}$ ]
$S_{\bar{k}}$	Precision index of the average (mean) stiffness [N/ $\mu\text{m}$ ]
$t$	Value of t-distribution for confidence level
$T$	Trial number
$U$	Unloading portion of test cycle
$U_k$	Uncertainty of estimated bearing stiffness [N/ $\mu\text{m}$ ]
$u_F$	Uncertainty of hand-held dynamometer [N]
$u_V$	Uncertainty of voltmeter [V]
$V$	Voltage reading [V]
$x$	Bearing displacement in horizontal direction [ $\mu\text{m}$ ]
$\nu$	Degrees of freedom, $N - 1$

## Introduction

Displacement versus static force tests were performed on a bump-type foil gas bearing (Foster-Miller Part Number 2015-007-REV B 048). The structural stiffness ( $k$ ) of the bearing estimated from the test results will serve to verify structural stiffnesses to be obtained from single frequency dynamic load tests to be performed in the near future. The bearing has an inner diameter of  $38.35 \pm 0.09$  mm ( $1.510 \pm 0.0037$  in.) and weighs 0.285 kg. The test shaft has an outer diameter of  $38.05 \pm 0.03$  mm ( $1.498 \pm 0.0011$  in.). The bearing radial clearance is  $\sim 0.15$  mm with null preload.

A piezoelectric load cell is attached to the bearing housing with a threaded stud. Figure 1 shows the bearing and the specified orientations for load cell attachment. One location coincides with the angular location of the spot weld, hereby designated as “0° position”. The other location is 90°, counter-clockwise from free end of top foil. A stinger rigidly attaches an electromagnetic shaker to the bearing through a load cell at each of these positions.

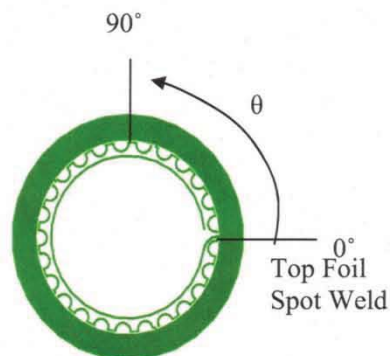


**Figure 1 Schematic view of test foil bearing**

Two measurements tests (1 and 2) were performed on one day; and on another day, two more tests (3 and 4) were conducted to verify repeatability. The test cases are as follows:

1. With shaker attached--0° load orientation
2. Without shaker attached--0°
3. With shaker attached--90° load orientation
4. Without shaker attached--90°



## Test Procedure

Figure 2 shows the test set up. The static pull force is applied horizontally on the bearing, away from the shaker and towards the eddy current sensor [10.7 mV/ $\mu\text{m}$  (271 mV/mil)] [1]. Voltage changes from the eddy currents sensor are recorded as the static load changes. A handheld dynamometer is used to record visually the applied load.

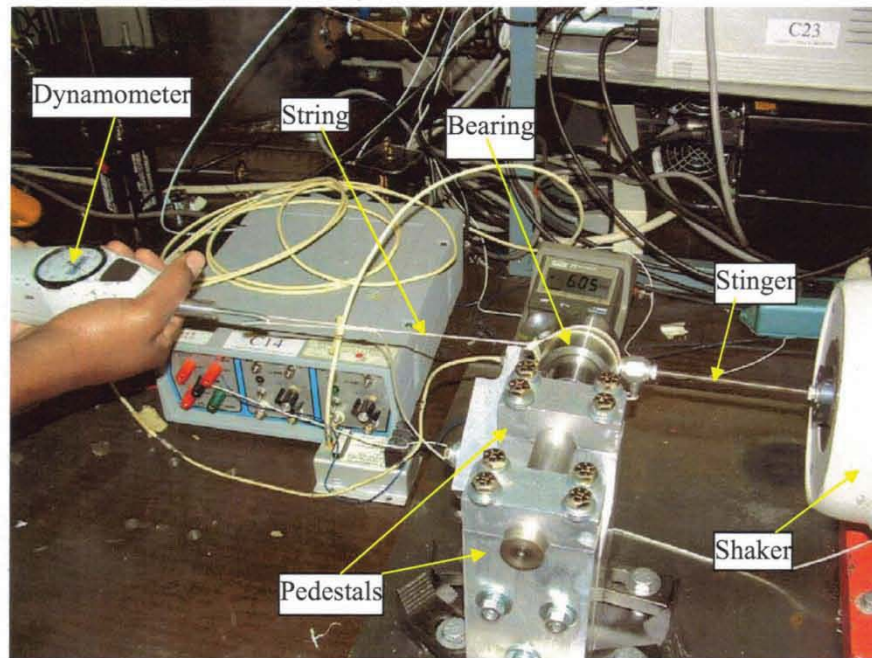


**Figure 2 Test set up for static loading of foil bearing**

The influence of the shaker and its attachment is determined from observed differences in tests 1 and 2, for example. During tests without the shaker attached, the bearing is placed on the test shaft and any dry friction between the bumps and the top foil or the housing is overcome by tapping slightly with a wrench the shaft along its axial direction. The vibrations through the shaft cause the foils to relax around the shaft. A distance between the bearing housing and the eddy current sensor tip is noted when the voltage readout stops changing. This condition is assumed to be the equilibrium initial position for testing.

During tests with the shaker attached, the bearing is placed on the shaft and its starting position is determined from the procedure presented above. The eddy current sensor voltage



readout is noted. The shaker stinger is then attached to the load cell, and the nuts on the stinger are tightened to prevent relative movement between the shaker and the bearing. Inserting the stinger into the load cell puts tension on the nuts and moves the bearing toward the eddy current sensor. The sensor voltage readout is different due to movement of the bearing housing in relation to the eddy current sensor tip. Therefore, the shaker must be moved away from the pedestals to bring the bearing to the same equilibrium position as in the tests without the shaker.

The dynamometer loads the bearing at 4.4 N (1 lb) increments up to 44.5 N (10 lb) with eddy current sensor voltage readings recorded at each increment. Then, the applied force is reduced at 4.4 N (1 lb) decrements towards the unloaded condition while recording the ensuing voltages from the displacement sensors.

### ***Experimental Results***

Figures 3 thru 6 depict the bearing displacements ( $\mu\text{m}$ ) versus applied static force (N) for each case described above during loading and unloading conditions. Arrows indicate the test number (T#) and either loading or unloading (L or U). For example, the loading case for the third test case is denoted as “T3-L.” A non linear relationship is apparent between the bearing displacements and applied load. There is hysteresis between the loading and unloading portions of each test. In general, after removing the load applied, the bearing did not return to its initial equilibrium position, presumably due to dry-friction effects and also due to inherent inaccuracies in the static loading process; i.e. difficulties in maintaining the load horizontal, for example.

A third order polynomial curve fit establishes a relationship between the static load and bearing displacement; i.e.  $F = f(x)$  [2].

As shown in Figures 3 thru 6, there is good repeatability for the measurements conducted on the same day, i.e. results for Trials 1 and 2 are close to each other, idem for Trials 3 and 4. Human error during the loading and unloading process, as well as not accurately eliminating any initial eccentricity between the shaft and bearing, may have contributed to the apparent differences in the data gathered on separate days, i.e. trials 1 and 3, for example.

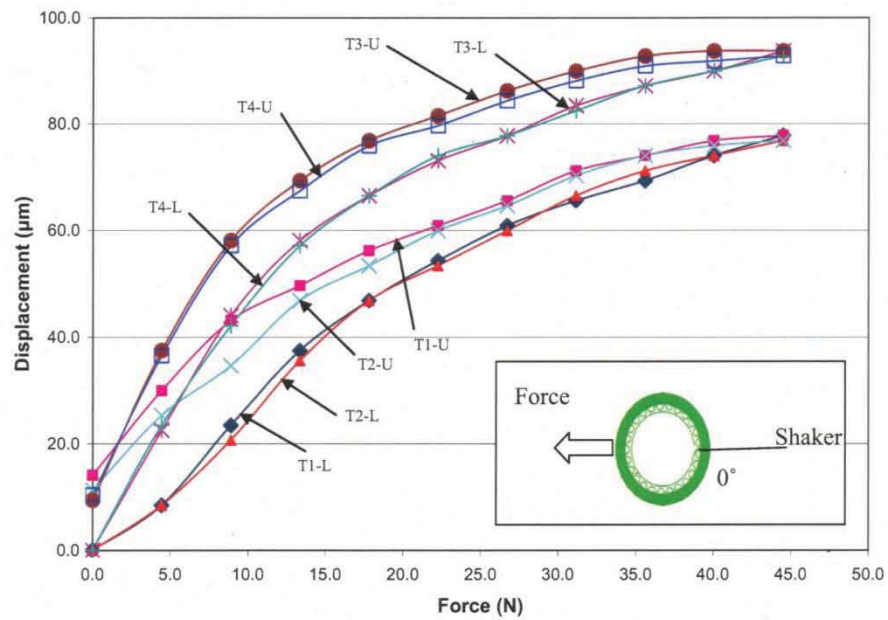


Figure 3 Foil bearing displacement versus applied static load for tests with shaker attached at  $0^\circ$  position

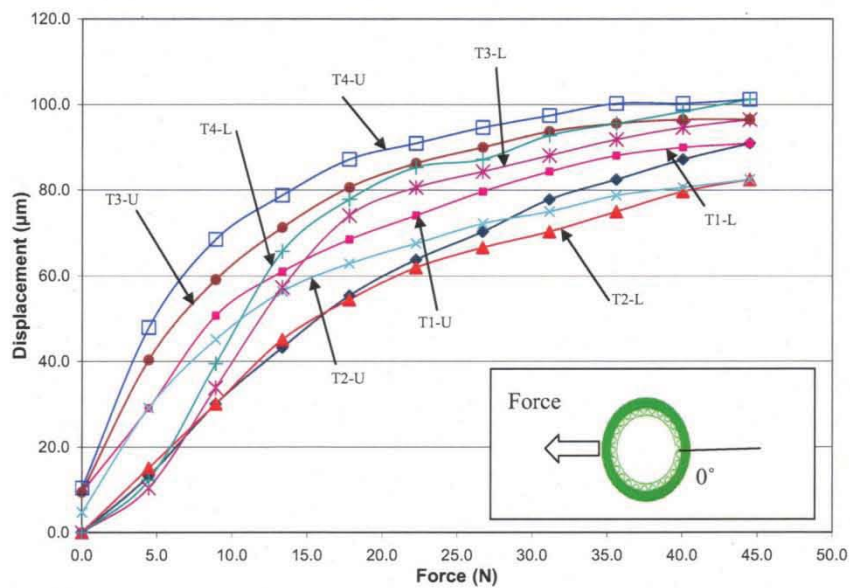
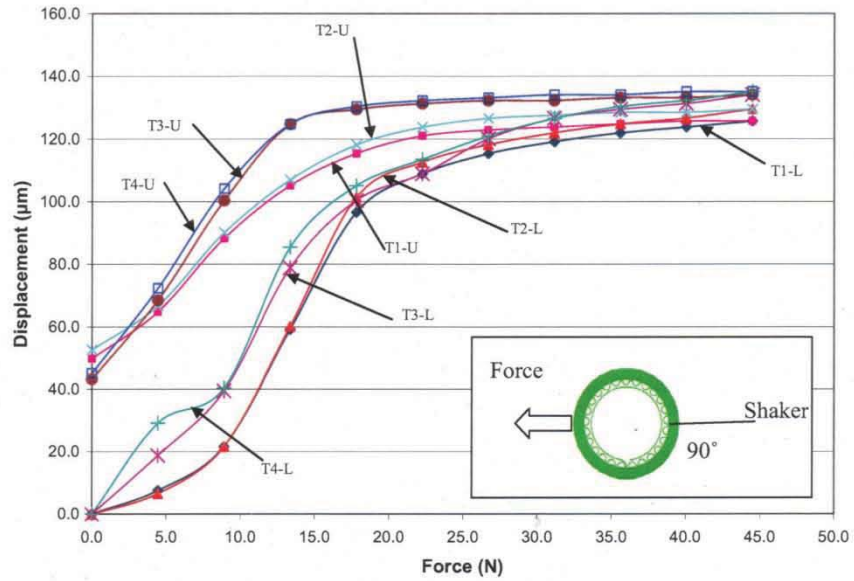
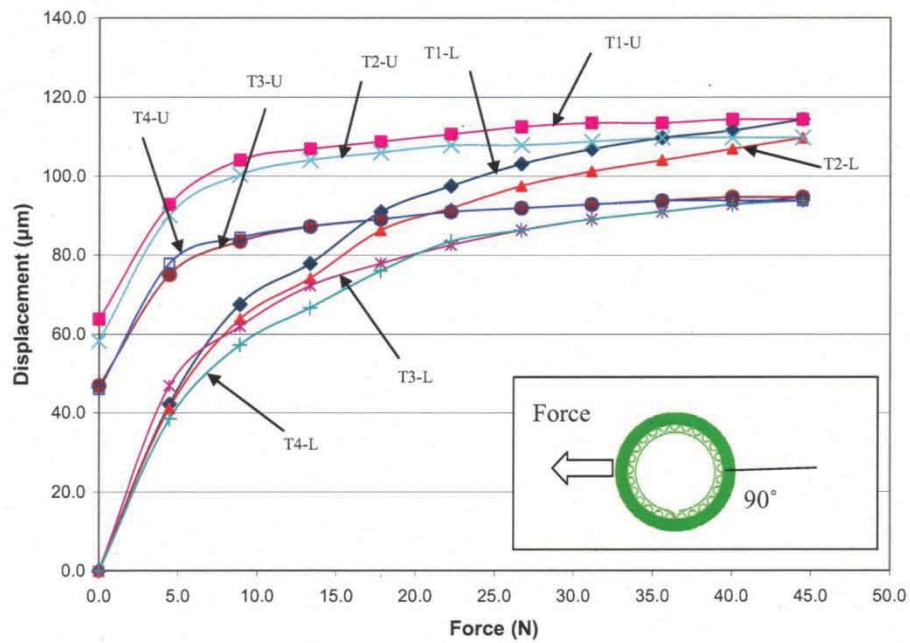


Figure 4 Foil bearing displacement versus applied static load for tests without shaker attached at  $0^\circ$  position



**Figure 5** Foil bearing displacement versus applied static load for tests with shaker attached at  $90^\circ$  position



**Figure 6** Bearing Foil bearing displacement versus applied static load for tests without shaker attached at  $90^\circ$  position

The non linear relationship between the displacement and applied force is evident in each of the test results. The foil bearing construction results in a varying stiffness as the applied load changes [2]. At low loads, the bearing moves relatively freely until the “clearance” between the shaft and top foil is traversed. As the applied load increases, the shaft forces the top foil radially outward, and the top foil engages more bumps. At higher loads, even more bumps are engaged and the stiffness increases further. Since this investigation is only up to 44.5 N of applied load, the maximum stiffness of the bearing is not determined.

Table 1 shows the formula for the third order polynomials obtained from the test data for all four test cases. The polynomials represent only the loading portion of each load cycle. Displacement ranges are different in each test. The correlation coefficient ( $R^2$ ) indicates the goodness of fit to the actual data.

Table 2 shows the formula for the derived structural stiffness,  $k = \partial F / \partial x$ , for each test case. The term associated to  $x^0$  represents the stiffness at equilibrium (null load). As the load (displacement) increases, some small negative stiffnesses are apparent. These values are not actual (real) and refer to the limitation in the curve fit equation for certain test cases.

Notice the lack of repeatability between the trials performed on each day on the estimated stiffness versus displacement, see Figures 7 thru 10. The estimated stiffness magnitudes vary by as much as 0.6 N/ $\mu\text{m}$ . Trials 1 and 2 show good agreements in all cases except at the 0° position without shaker attachment, which is also the case for the force versus displacement curves (Figure 4). Trial 3 and Trial 4 match closely for all cases except at the 0° position without shaker attachment. The variability in these trials for this specific case may be due to the loading procedure. Also, note the significant variability in FB stiffness magnitude from tests conducted in different days. Loading the bearing with the dynamometer oriented in a way not exactly perpendicular with the axis of the bearing, or not perfectly level with the horizontal plane, could have lead to the observed discrepancies.



**Table 1 Curve fit equations for force as a function of displacement for four load cases – Loading condition only**

Case	Trial #	Force F (N) versus Displacement x (μm) Equations	x Range (μm)	R <sup>2</sup>
<b>With Shaker</b> <b>0 Degrees</b>	1	$F = 1.121\text{E-}04x^3 - 7.548\text{E-}03x^2 + 0.4813x + 0.3261$	[0 , 77.8]	0.9994
	2	$F = 1.418\text{E-}04x^3 - 1.141\text{E-}02x^2 + 0.6083x - 5.456\text{E-}03$	[0 , 76.9]	0.9985
	3	$F = 8.868\text{E-}05x^3 - 6.610\text{E-}03x^2 + 0.3159x - 0.06871$	[0 , 93.7]	0.9994
	4	$F = 9.880\text{E-}05x^3 - 7.920\text{E-}03x^2 + 0.3591x - 0.1793$	[0 , 93.8]	0.9986
<b>No Shaker</b> <b>0 Degrees</b>	1	$F = 6.269\text{E-}05x^3 - 4.619\text{E-}03x^2 + 0.3877x - 0.02080$	[0 , 90.9]	0.9996
	2	$F = 1.018\text{E-}04x^3 - 6.560\text{E-}03x^2 + 0.3878x - 0.02466$	[0 , 82.5]	0.9989
	3	$F = 1.587\text{E-}04x^3 - 1.817\text{E-}02x^2 + 0.7293x - 0.5652$	[0 , 96.5]	0.9963
	4	$F = 1.373\text{E-}04x^3 - 1.599\text{E-}02x^2 + 0.6517x - 0.5070$	[0 , 101.2]	0.9966
<b>With Shaker</b> <b>90 Degrees</b>	1	$F = 1.010\text{E-}04x^3 - 1.685\text{E-}02x^2 + 0.8604x - 0.9547$	[0 , 125.6]	0.9854
	2	$F = 9.909\text{E-}05x^3 - 1.693\text{E-}02x^2 + 0.8671x - 0.7756$	[0 , 129.3]	0.9886
	3	$F = 5.329\text{E-}05x^3 - 8.521\text{E-}03x^2 + 0.5014x - 0.8388$	[0 , 134.0]	0.9860
	4	$F = 5.448\text{E-}05x^3 - 8.414\text{E-}03x^2 + 0.4596x - 0.6823$	[0 , 135.0]	0.9870
<b>No Shaker</b> <b>90 Degrees</b>	1	$F = 8.740\text{E-}05x^3 - 1.048\text{E-}02x^2 + 0.4309x - 0.2224$	[0 , 114.3]	0.9904
	2	$F = 9.054\text{E-}05x^3 - 9.884\text{E-}03x^2 + 0.3925x - 0.1610$	[0 , 109.7]	0.9953
	3	$F = 2.135\text{E-}04x^3 - 2.317\text{E-}02x^2 + 0.7361x - 0.06556$	[0 , 94.7]	0.9951
	4	$F = 1.844\text{E-}04x^3 - 1.947\text{E-}02x^2 + 0.6444x - 0.2228$	[0 , 93.7]	0.9810

**Table 2 Structural stiffness derived from displacement vs force measurements**

Case	Trial #	Structural Stiffness k (N/μm) versus Displacement x (μm) Equations	x Range (μm)
<b>With Shaker</b> <b>0 Degrees</b>	1	$k = 3.363\text{E-}04x^2 - 1.5096\text{E-}02x + 0.4813$	[0 , 77.8]
	2	$k = 4.254\text{E-}04x^2 - 2.282\text{E-}02x + 0.6083$	[0 , 76.9]
	3	$k = 2.6604\text{E-}04x^2 - 1.322\text{E-}02x + 0.3159$	[0 , 93.7]
	4	$k = 2.964\text{E-}04x^2 - 1.584\text{E-}02x + 0.3591$	[0 , 93.8]
<b>No Shaker</b> <b>0 Degrees</b>	1	$k = 1.8807\text{E-}04x^2 - 3.168\text{E-}02x + 0.3877$	[0 , 90.9]
	2	$k = 3.054\text{E-}04x^2 - 1.312\text{E-}02x + 0.3878$	[0 , 82.5]
	3	$k = 4.761\text{E-}04x^2 - 3.634\text{E-}02x + 0.7293$	[0 , 96.5]
	4	$k = 4.119\text{E-}04x^2 - 3.198\text{E-}02x + 0.6517$	[0 , 101.2]
<b>With Shaker</b> <b>90 Degrees</b>	1	$k = 3.030\text{E-}04x^2 - 3.370\text{E-}02x + 0.8604$	[0 , 125.6]
	2	$k = 2.9727\text{E-}04x^2 - 3.3860\text{E-}02x + 0.8671$	[0 , 129.3]
	3	$k = 1.5987\text{E-}04x^2 - 1.7042\text{E-}02x + 0.5014$	[0 , 134.0]
	4	$k = 1.6344\text{E-}04x^2 - 1.6828\text{E-}02x + 0.4596$	[0 , 135.0]
<b>No Shaker</b> <b>90 Degrees</b>	1	$k = 2.622\text{E-}04x^2 - 2.096\text{E-}02x + 0.4309$	[0 , 114.3]
	2	$k = 2.7162\text{E-}04x^2 - 1.9768\text{E-}02x + 0.3925$	[0 , 109.7]
	3	$k = 6.405\text{E-}04x^2 - 4.634\text{E-}02x + 0.7361$	[0 , 94.7]
	4	$k = 5.532\text{E-}04x^2 - 3.894\text{E-}02x + 0.6444$	[0 , 93.7]

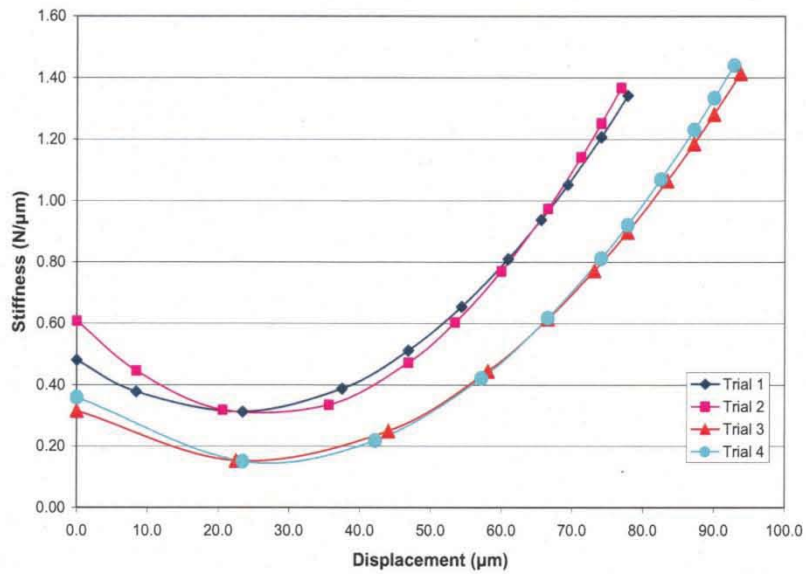


**Figure 7** Estimated foil bearing structural stiffness versus displacement. Test case: bearing with shaker attached, 0° position

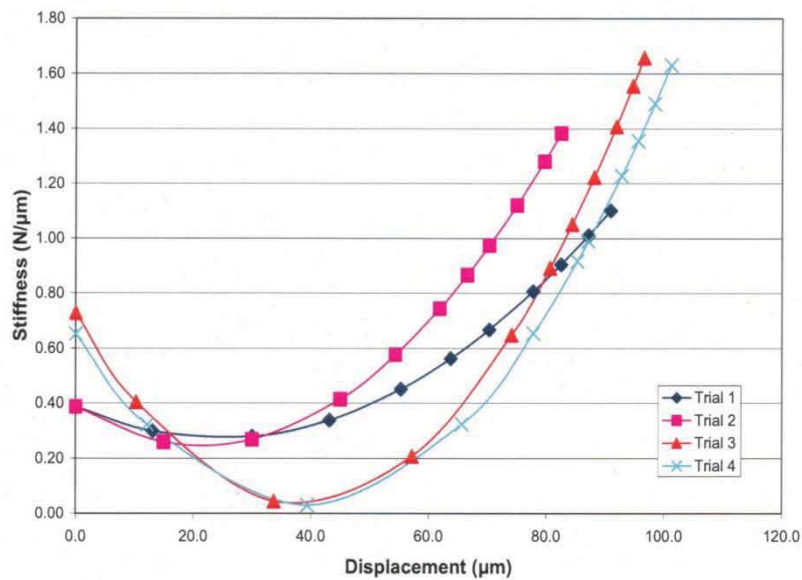


**Figure 8** Estimated foil bearing structural stiffness versus displacement. Test case: bearing without shaker attached, 0° position

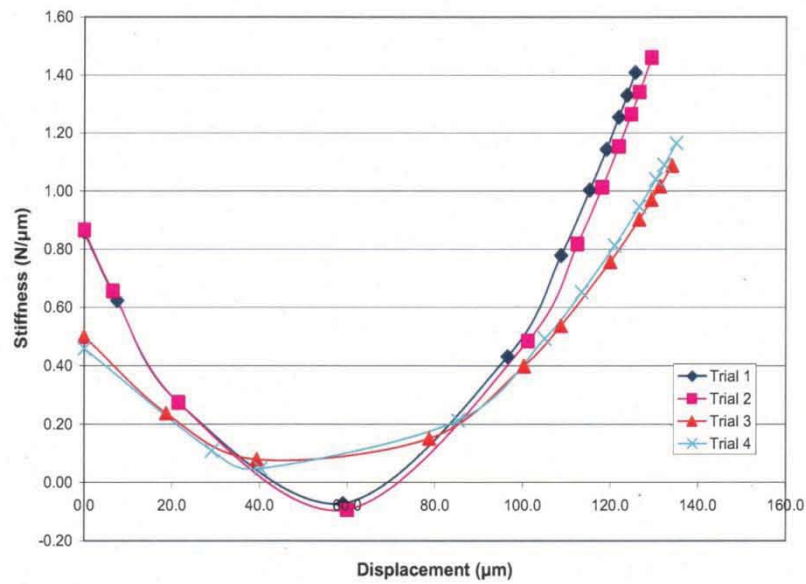


**Figure 9 Estimated foil bearing structural stiffness versus displacement. Test case: bearing with shaker attached, 90° position**

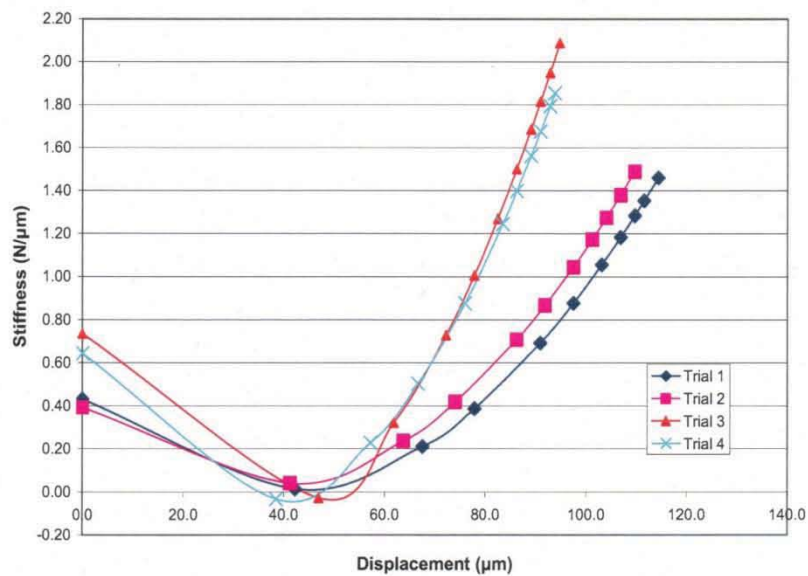


**Figure 10 Estimated foil bearing structural stiffness versus displacement. Test case: bearing without shaker attached, 90° position**

Rubio and San Andrés [2] presented data for bearing stiffness calculated using a shaft with 38.07-mm diameter and bearing with an inner diameter of 38.35 mm. These earlier results are reproduced in Table 3 below. Note that in [2], static load tests were conducted with the *FB* rigidly mounted on a lathe and with the dynamometer secured into the tool holder; thus the results given in [2] are more accurate than the ones presented here. However, the influence of the shaker attachment is not accounted for in the earlier experiments.

Table 4 presents the test results from the current investigation for Trial 3, 0° and 90° positions, without the shaker attached, as in [2]. Note that the bearing stiffness decreases at lower displacements, and then increases due to the bearing traversing its clearance. Comparison to the data in [2], reproduced in Table 3, shows that the present estimated stiffnesses are considerably less for all load values.

**Table 3 Deflection and structural stiffness data for the 0° and 90° positions. Taken from [2]**

Static Load [N]	0° Position			90° Position		
	Deflection [μm]	Stiffness [N/μm]	Uncertainty [N/μm]	Deflection [μm]	Stiffness [N/μm]	Uncertainty [N/μm]
0	0.00	0.13	0.14	0.00	0.28	0.05
4	10.16	0.58	0.02	34.29	0.87	0.10
9	48.26	0.83	0.03	40.64	1.08	0.10
13	66.04	1.03	0.03	45.72	1.27	0.09
18	74.93	1.13	0.03	49.53	1.42	0.09
22	81.28	1.24	0.03	52.07	1.54	0.09
36	93.98	1.52	0.04	59.69	1.90	0.10
44	100.33	1.69	0.04	63.50	2.09	0.10

Figures 11 and 12 display the applied static load versus recorded bearing displacement for Trial 3 of the *FB* 0° and 90° Positions, respectively. Note the curve fits for the two cases. At lower displacements (<~70 μm) the trend line does not represent well the measured data; thus then the poor curve confidence in estimated stiffnesses at low bearing displacements.



**Table 4 Present deflection and structural stiffness data for the 0° and 90° positions, without shaker attached, Trial 3 of each case**

Static Load [N]	0° Position			90° Position		
	Deflection [μm]	Stiffness [N/μm]	Uncertainty [N/μm]	Deflection [μm]	Stiffness [N/μm]	Uncertainty [N/μm]
0	0.0	0.73	0.06	0.0	0.74	0.07
4	10.3	0.41	0.07	46.9	-0.03	0.53
9	33.7	0.05	0.10	61.9	0.32	0.12
13	57.2	0.21	0.10	72.2	0.73	0.07
18	74.0	0.65	0.06	77.8	1.01	0.06
22	80.6	0.89	0.05	82.5	1.27	0.06
36	91.9	1.41	0.05	90.9	1.82	0.05
44	96.5	1.66	0.05	94.7	2.09	0.05

In [2], the static load ranged from -222 N to 222 N, which is more representative of actual load conditions. The region of small loads (and displacements) was not readily apparent because of the large load range. Note in Tables 3 and 4 the estimated stiffnesses for each data set at a load of 44N. The magnitudes presently identified are within 0.03 N/μm for the 0° position and identical to those in [2] for the 90° position. Table 5 shows the identified FB stiffnesses for the test cases at loads equal to 22.2 N and 44.5 N. The uncertainties are also given, as determined from the general uncertainty analysis given in Appendix A.

Since multiple trials were performed for each case, an average (mean) and a precision limit prove helpful. The interval defined by  $\bar{k} \pm P_k$  gives the range for 95% confidence. Table 6 displays the calculated mean and precision limit of the mean of the four stiffness magnitudes for the four cases. See Appendix B for the respective analysis. The table shows significant variability for the estimated stiffnesses. For example, the mean bearing stiffness at the 90° orientation for the two cases (with and without shaker) varies by 35%.

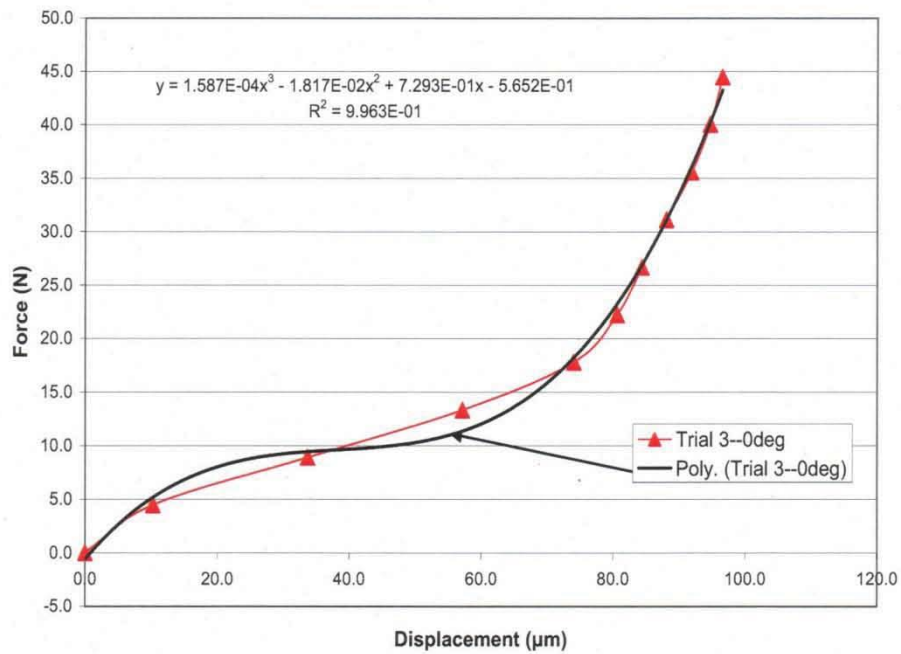


**Figure 11 Applied force versus bearing displacement and third-order polynomial fit for Trial 3 of 0° Position**

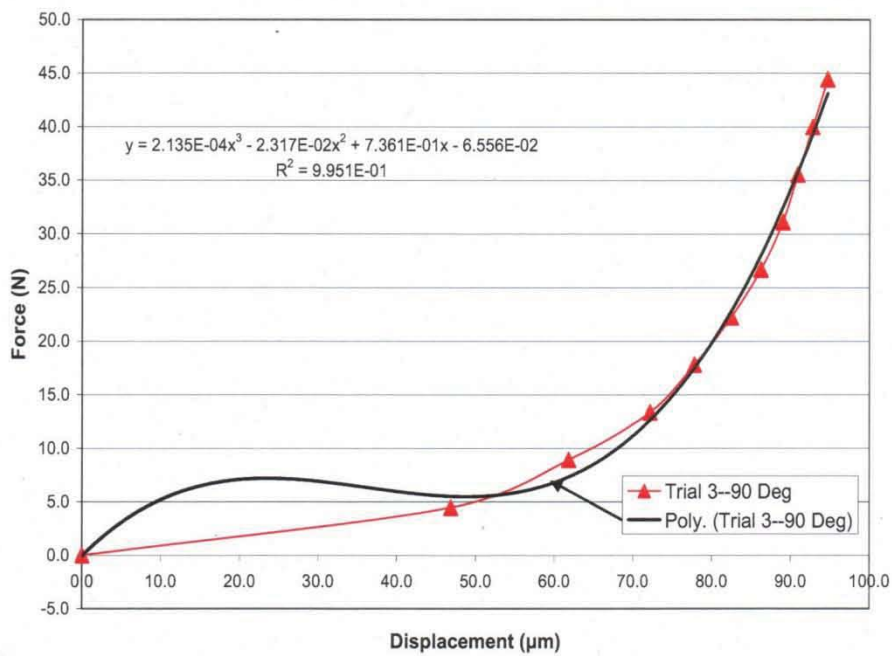


**Figure 12 Applied force versus bearing displacement and third-order polynomial fit Trial 3 of 90° Position**

**Table 5 FB structural stiffness at 22.3 N and 44.5 N for four test cases**

Case	Trial #	R <sup>2</sup>	Stiffness (N/μm) [at 22.2 N]	Uncertainty (N/ μm)	Stiffness (N/μm) [at 44.5 N]	Uncertainty (N/μm)
<b>With Shaker</b> <b>0 Degrees</b>	1	0.9994	0.654	0.038	1.341	0.035
	2	0.9985	0.603	0.043	1.366	0.040
	3	0.9994	0.771	0.039	1.413	0.034
	4	0.9986	0.811	0.041	1.440	0.035
<b>No Shaker</b> <b>0 Degrees</b>	1	0.9996	0.562	0.030	1.101	0.028
	2	0.9989	0.744	0.039	1.382	0.035
	3	0.9963	0.892	0.054	1.657	0.045
	4	0.9966	0.917	0.050	1.629	0.042
<b>With Shaker</b> <b>90 Degrees</b>	1	0.9854	0.779	0.048	1.409	0.039
	2	0.9886	0.818	0.047	1.459	0.038
	3	0.9860	0.538	0.038	1.088	0.029
	4	0.9870	0.653	0.036	1.165	0.029
<b>No Shaker</b> <b>90 Degrees</b>	1	0.9904	0.878	0.041	1.461	0.035
	2	0.9953	0.868	0.041	1.490	0.035
	3	0.9951	1.271	0.059	2.089	0.053
	4	0.9810	1.245	0.054	1.854	0.049

**Table 6 Tabulated average values of structural stiffness and precision limit intervals for two static loads**

Case	$\bar{k} \pm P_k$ (N/μm) at 22.2 N	$\bar{k} \pm P_k$ (N/μm) at 44.5 N
<b>With Shaker/0 degrees</b>	0.71±0.16	1.39±0.07
<b>Without Shaker/0 degrees</b>	0.78±0.26	1.44±0.41
<b>With Shaker/90 degrees</b>	0.68±0.20	1.28±0.29
<b>Without Shaker/90 degrees</b>	1.07±0.35	1.72±0.48

The identification leading to the highest correlation coefficient  $R^2 \sim 1.00$  determines the best estimated FB stiffnesses. Table 7 presents the FB stiffnesses and their uncertainty at 22.2 N and 44.5 N of applied load for the 0° and 90° positions with and without the shaker attached. The maximum reported stiffnesses at 44.5 compare well with the prior results given in [2].

**Table 7 Estimated FB structural stiffness at 44.5 N load, one with highest correlation coefficient and one with maximum magnitude for each test case**

Case	Trial #	Best Correlation Coefficient, $R^2$			Maximum Value	
		$R^2$	Stiffness (N/ $\mu$ m) [at 44.5]	Uncertainty (N/ $\mu$ m)	Stiffness (N/ $\mu$ m) [at 44.5 N]	Uncertainty (N/ $\mu$ m)
<b>With Shaker/0°</b>	<b>1</b>	<b>0.9994</b>	<b>1.34</b>	<b>0.04</b>	<b>1.44</b>	<b>0.04</b>
Without Shaker/0°	1	0.9996	1.10	0.03	1.66	0.05
<b>With Shaker/90°</b>	<b>2</b>	<b>0.9886</b>	<b>1.46</b>	<b>0.04</b>	<b>1.46</b>	<b>0.04</b>
Without Shaker/90°	2	0.9953	1.49	0.04	2.09	0.05

### ***Preliminary conclusions***

FB stiffnesses identified at low loads may be in error since the third order polynomial curve fit does not reproduce well the recorded deflection versus load behavior. In essence, at low loads, the FB is very soft due to its large initial clearance.

Poor repeatability in recorded displacements is apparent from tests conducted on different days. This deficiency is strictly due to human error. Further investigation will be required with more careful loading procedures during testing.

### ***References***

- [1] Breedlove, A., 2005, "Calibration of Bently Nevada 7200 Series Eddy Current Sensor," Research Progress Report, February.
- [2] Rubio, D., and San Andrés, L., 2003, "Bump-Type Foil Bearing Structural Stiffness: Experiments and Predictions," Research Progress Report to TRC, TRC-B&C-5-03, pp. 8-20.
- [3] Coleman, H. and W. Steele, 1985, *Experimentation and Uncertainty Analysis for Engineers*, Wiley-Interscience Publication, pp. 26-28.

## Appendix A. Uncertainty Analysis

The derivation of the uncertainty ( $U_k$ ) for the stiffness ( $k$ ) derived from the force versus displacement curve fit polynomial is taken from [2].

$$U_k = \sqrt{\left(\frac{\partial f}{\partial x} * \frac{\partial x}{\partial V} * u_V\right)^2 + \left(\frac{\partial f}{\partial x} * \frac{\partial x}{\partial F} * u_F\right)^2}$$

where

$$\frac{\partial f}{\partial x} = \frac{\partial k}{\partial x} = \frac{\partial^2 F}{\partial x^2},$$

$$\frac{\partial x}{\partial V} = \frac{1}{G},$$

$$\frac{\partial x}{\partial F} = \frac{1}{\frac{\partial F}{\partial x}},$$

$$u_V = 5mV,$$

$$u_F = 1.1N,$$

$$G = \text{eddycurrentsensorgain} = 10.7mV / \mu m$$

## **Appendix B. Precision Limit of the Mean of the Trials**

The following derivation determines the precision limit of the mean of a sample of  $N$  measurements of stiffness ( $k$ ) drawn from a Gaussian distribution [3]. The mean of a sample population is given by

$$\bar{k} = \frac{1}{N} \sum_{i=1}^N k_i.$$

The precision index or the sample standard deviation is given by

$$S_k = \left[ \frac{1}{N-1} \sum_{i=1}^N (k_i - \bar{k})^2 \right]^{\frac{1}{2}}.$$

Further, the precision index of the mean can be calculated using

$$S_{\bar{k}} = S_k / \sqrt{N}.$$

Finally, the precision limit of the mean is calculated with the simple relation

$$P_{\bar{k}} = t S_{\bar{k}} = t S_k / \sqrt{N}$$

where  $t$  is taken from the Table A.2 in the text for  $\nu = N - 1$ .

The interval defined by  $\bar{k} \pm P_{\bar{k}}$  gives the range within which it is expected, with 95% confidence, for the mean value of the parent population to fall; that is, if an infinite number of samples of the stiffness could be taken, then the mean value of the samples would fall within this range.

**APPENDIX B**  
**Purdue University Contribution**



**NUMERICAL ANALYSIS OF BEARING PERFORMANCE  
AND POWER LOSS**

Submitted to the Wright Patterson Air Force Base  
December 2004

Mechanical Engineering Tribology Laboratory  
Purdue University

Principal Investigator: Farshid Sadeghi  
Research Assistant: Bradley Pederson



## TABLE OF CONTENTS

1.1 Summary of Work Completed.....	3
1.1.1 METL Dynamic Bearing Model.....	3
1.1.2 Traction Curves.....	4
1.1.3 Operating Conditions .....	4
1.1.4 Geometrical Clearances .....	5
1.1.5 Material Properties.....	5
1.2 Output Files Included in the Attached CD.....	6
1.2.1 Output File Labeling .....	7
1.2.2 Variables Printed to Output .....	8
1.3 Sample of Plotted Results .....	9
1.4 Additional Results.....	14
1.5 List of References .....	23

## **1.1 Summary of Work Completed**

A comprehensive investigation of bearing performance and power loss was completed using the Mechanical Engineering Tribology Lab's (METL) Dynamic Bearing Model (DBM) for various cage, race, and rolling element materials for a series of loads, speeds, and clearances. The investigation focused on the power loss at the race-to-cage and ball-to-cage contacts. Additionally, the power loss at ball-to-cage pocket contact was included. Power loss parameters and bearing element state data were written to two separate ASCII output files included in the attached CD. Utilizing both files, an experienced bearing analyst can make further investigations into the dynamics and performance of the bearing operation. In all cases, the bearing simulation ran for 1000 revolutions of the inner race.

### **1.1.1 METL Dynamic Bearing Model**

The model used in the current investigation was the METL Dynamic DBM for angular contact and deep groove ball bearings. The current investigation required the use of the angular contact model only. The DBM is a six degree-of-freedom, three-dimensional dynamic bearing model that utilizes a Runge-Kutta fourth order variable step size time integrator to solve for the position, velocity and acceleration of every element in the bearing. The model allows for contact detection at ball-to-races, cage-to-guiding race, and ball-to-cage pocket. Contact forces at all elements are summed and the resulting accelerations are integrated to determine the next set of element states using the largest time step possible that generates an error less than a prescribed value. The prescribed error value is predetermined to limit the numerical error to an insignificant quantity while allowing computational efficiency of the simulation.

### 1.1.2 Traction Curves

Figure 1 illustrates the traction coefficient for both the cage-to-race and ball-to-race contacts provided by Wright Patterson Air Force Base (WPAFB). However, the dynamic bearing model can support any number of traction coefficient models including constant, piece-wise linear and exponential curve fits.

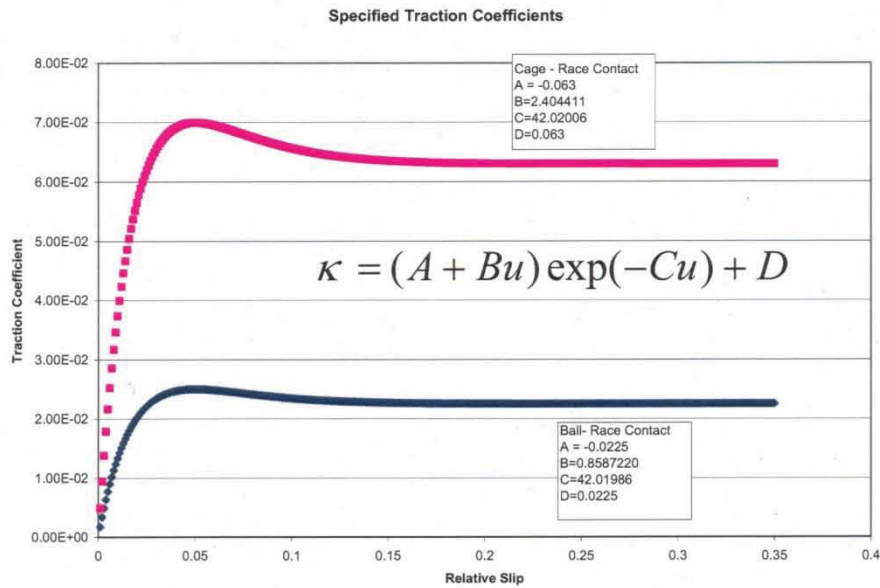


**Figure 1: Traction models provided for the current study.**

### 1.1.3 Operating Conditions

DBM was used to determine power loss for a range of speeds and loads. The bearing model was subjected to gravity and thrust loading, without the application of interference or radial loading, in order to fulfill the requirements of this project. Interference is the condition when the distance from the inner race groove to the outer race groove is less than the ball diameter. Table 1 contains the loading and speed combinations considered in the investigation. All bearing simulations for the current investigation started with

zero initial conditions. Starting with the zero initial conditions indicates that the bearing model will begin with all velocities and accelerations equal to zero.

**Table 1: Operating conditions and abbreviations used to label output files.**

Speeds/abbreviations:	Loads/abbreviations:
1 – 11,250 rpm	1 – 5,000 lb <sub>f</sub>
2 – 15,000 rpm	2 – 10,000 lb <sub>f</sub>
3 – 22,500 rpm	3 – 15,000 lb <sub>f</sub>

#### 1.1.4 Geometrical Clearances

Table 2 contains ball-to-cage pocket diametral clearances used in this study and supplied by WPAFB. Previous METL work focusing on diametral ball-to-cage pocket clearances indicates that clearance ratios can affect cage stability (Ghaisas, 2003). Given the range of ball-to-cage pocket clearances, three clearance values were selected for the power loss investigation. Selecting the upper and lower clearance limits, as well as the mean, provided complete coverage on the possible effects of clearance ratio on power loss.

**Table 2: Ball-to-cage pocket diametral clearance.**

	Inches	Meters
Clearance Range:	0.026 - 0.035	6.604e-004 – 8.89e-004
Min (clearance)	0.026	6.604e-004
Mean (clearance)	0.0305	7.747e-004
Max (clearance)	0.035	8.89e-004

#### 1.1.5 Material Properties

Material data was provided for the races, cage, and balls as shown in Table 3. Ball and cage properties were varied in order to investigate their effect on power loss and performance, while holding the race material properties constant.

**Table 3: Angular contact bearing materials employed in the current study.**

Element	E (Gpa)	Possion's Ratio	Density (kg/m <sup>3</sup> )
M50 Races	175	0.29	8190
Si3N4 Balls	320	0.26	3160
M50 Balls	175	0.29	8190
4340 Cage	170	0.3	7750
C-C(t) Cage	100	0.05	1600

### 1.2 Output Files Included in the Attached CD

The results from this investigation are included on the attached CD. The output files can be opened using Excel, MATLAB, or any alternate data processing software compatible with an ASCII file format. For the current project, a power loss file was generated in addition to the generic output file that contains many variables that are frequently of interest to bearing analysts. It should be noted that a select number of bearing variables were written to the data file, but this number is user-determinable and can be adjusted to investigate any one specific area of bearing performance. Bearing element states were sampled for every 2 degrees of inner race rotation.

The generic bearing variable output file, labeled as `output_...` contains bearing state data such as velocities, positions, and forces, etc. as described in Sub-Section 1.2.2. This file also includes the corresponding simulation time.

A second output file labeled as `hp_...` contains the power loss variables specific to the current project. The power loss data file format is presented in Sub-Section 1.2.2.

### 1.2.1 Output File Labeling

A total of 108 different bearing simulations were completed for 1000 revolutions of the inner race. In order to distinguish between the various output files, a file labeling system was used and is presented by concatenating the following:

output\_WPAFB\_rpm + (speed #) + \_load + (load #) + \_ +  
 (clearance level) + clear + \_ + (race material) + (ball material) +  
 (cage material)

The same procedure was used for the power loss file. An example of which is given below:

Output\_WPAFB\_rpm1\_load1\_smallclear\_M50races\_Si3N4Balls\_CCCage  
 and  
 hp\_WPAFB\_rpm1\_load1\_smallclear\_M50races\_Si3N4Balls\_CCCage

These two files contain results for 11,250 rpm, 5,000 lb<sub>f</sub> load, minimum ball-to-cage pocket clearance using M50 races, Si<sub>3</sub>N<sub>4</sub> balls and a carbon-carbon cage.

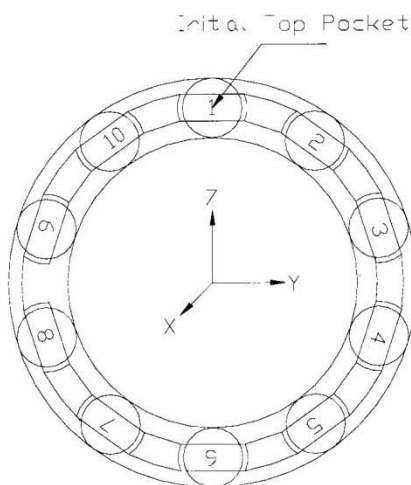


**Figure 2: Bearing axis orientation and location of the initial top pocket reference.**



### 1.2.2 Variables Printed to Output

Tables 4 and 5 contain the format for the output files in the attached DVD's.

**Table 4: Format for the generic output file (tab delimited columns):**

Column 1	Column 2	Column 3	Column 4	Column 5
Simulation Time (seconds)	Initial Top Ball X Velocity (m/sec)	Initial Top Ball Y Velocity (m/sec)	Initial Top Ball Z Velocity (m/sec)	Initial Top Ball Angular Velocity about X (rad/sec)
Column 6	Column 7	Column 8	Column 9	Column 10
Initial Top Ball Y Velocity (m/sec)	Cage CM X Position (m)	Cage CM Y Position (m)	Cage CM Z Position (m)	Inner Race CM X Position (m)
Column 11	Column 12	Column 13	Column 14	Column 15
Inner Race CM Y Position (m)	Inner Race CM Z Position (m)	Initial Top Ball Angle about IR (deg)	Initial Top Ball Angle with respect to IR Angle (deg)	Inner Race Angle with Respect to Vertical (deg)
Column 16	Column 17	Column 18	Column 19	Column 20
Ball to Inner Race Contact Force (N)	Average Ball to Cage Pocket Force (N)	Max Ball to IR Contact Pressure (N/m <sup>2</sup> )	Max Ball to OR Contact Pressure (N/m <sup>2</sup> )	Cage to Race Contact Force (N)
Column 21	Column 22	Column 23		
Inner Race Load in X Direction (N)	Inner Race Load in Y Direction (N)	Inner Race Load in Z Direction (N)		

**Table 5: Format for the power loss output file (tab delimited columns):**

Column 1	Column 2	Column 3	Column 4	Column 5
Power Loss Cage to Outer Race (W)	Power Loss All Balls to Inner Race (W)	Power Loss All Balls to Outer Race (W)	Power Loss All Balls to Cage Pockets (W)	(Cols 5 -14 were debug variables)

### 1.3 Sample of Plotted Results

In this section we present results for a bearing operating at 15,000 rpm with a 5,000 lb<sub>f</sub> axial load and the mean ball to cage pocket clearance.

Figure 3 displays the translational velocity magnitude of the ball initially located along the Z axis as it travels around the circumference of the inner race. Steady state conditions can be determined by comparing the velocity of the top ball (blue line) and the approximate kinematic velocity for the ball plotted in red. Steady state conditions begin shortly after the ball translational velocity magnitude reaches the approximate kinematic solution. A slight difference in velocity is attributed to the kinematic velocity not accounting for the ball rolling up the inner groove radius. The approximate kinematic velocity is computed at the center line of the inner race.

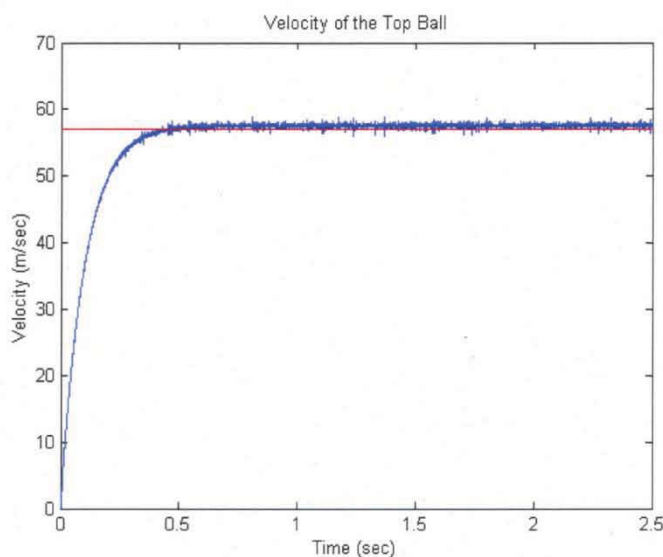


**Figure 3: Velocity of the initial top ball**

Figure 4 displays the cage center of mass as the cage rotates with the ball group. The current set of operating conditions causes erratic motion of the cage center of mass. Cage center of mass displacement is limited by the cage-to-guiding race radial clearance of  $3.43\text{e-}4$  meters, which is confirmed in Figure 4.



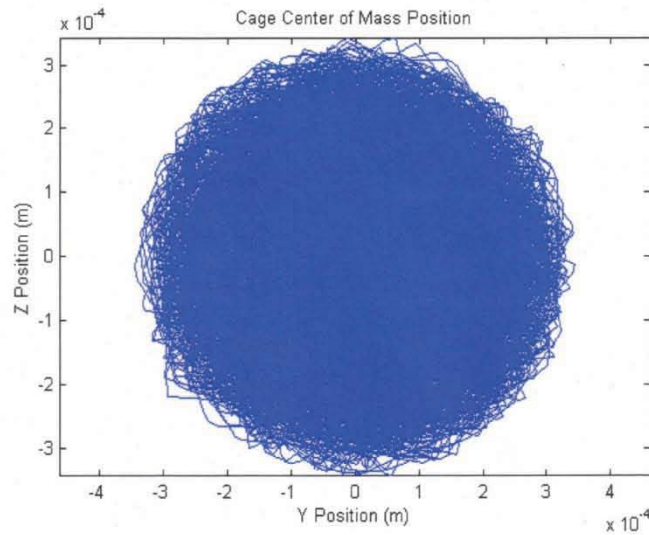


**Figure 4: Cage center of mass position**

Steady state cage-to-race contact power loss is depicted in Figure 5. Glancing cage-to-guiding race contacts and unstable cage motion cause the impulsive power loss presented in Figure 5.

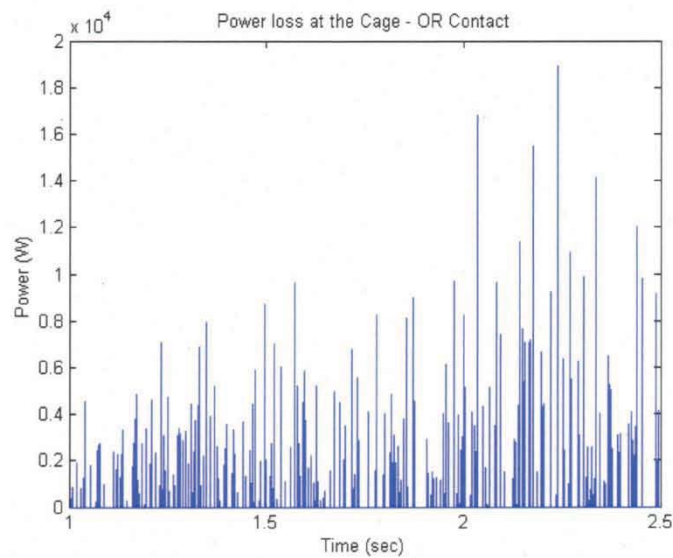


**Figure 5: Steady state power loss at the cage-to-outer race contact**

Steady power loss results shown in Figures 6 and 7, for ball-to-inner race and ball-to-outer race contact respectively, show steady power loss with sudden decreases at coincidental times. Ball-to-cage pocket power loss presented in Figure 8 will provide the explanation for the sudden change in power loss of Figures 6 and 7.

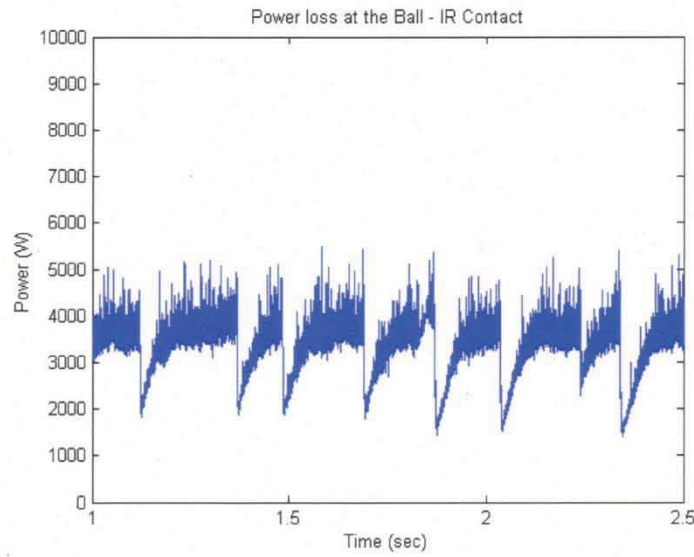


**Figure 6: Steady state power loss at the ball-to-inner race contact**

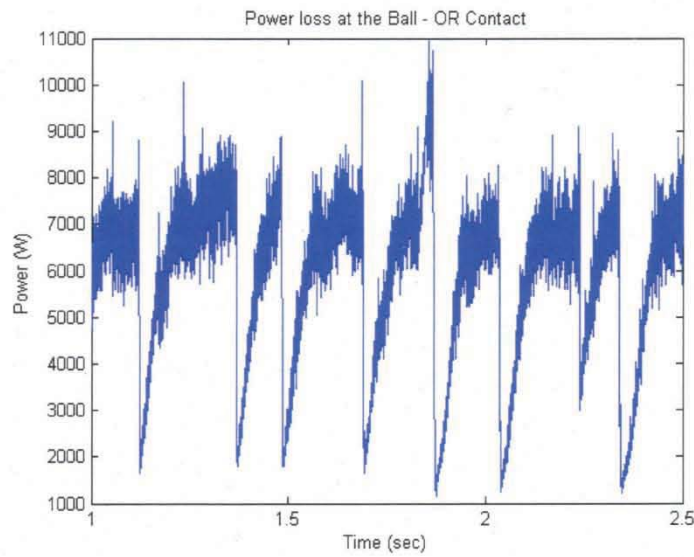


**Figure 7: Steady state power loss at the ball-to-outer race contact**

Given an axial load, the ball group rolls up the side of both race grooves and a near constant normal force occurs on the balls and races. Under these conditions, slip can occur and can be a significant contributor to power loss at the ball-to-inner and ball-to-outer race contacts when erratic cage motion causes large impulsive forces on the balls. Results for all ball-to-race contacts are included in Figures 6 and 7.

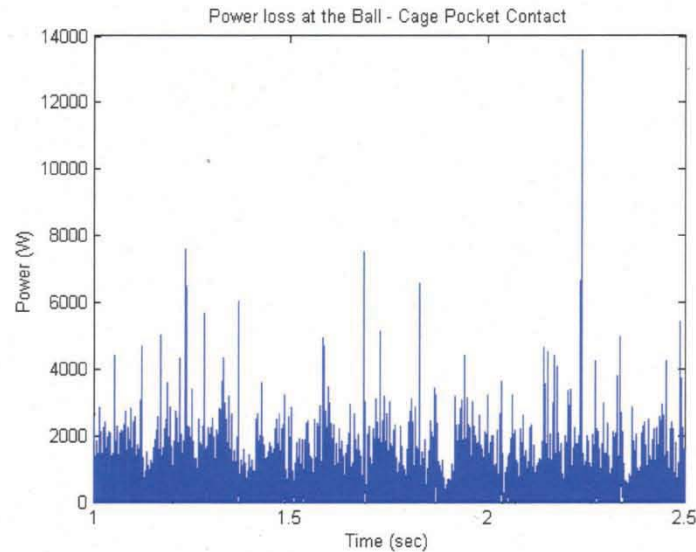


**Figure 8: Steady state power loss at the ball-to-cage pocket contact**

Figure 8 depicts ball-to-cage power loss, which includes all ball-to-cage contacts. The power loss oscillation is due to contact occurring between any one of the balls in the ball group and the cage. Ball-to-cage contacts generally are sliding contacts with large relative velocities and frictional forces that operate in the upper region of the traction curve (Figure 1). The ball-to-cage pocket contact also has an effect on the stability of the cage which correlates with sharp decline of power loss in Figures 6 and 7. Figure 9 shows results of the ball-to-cage pocket contact in the specific time corresponding to the sharp declines seen in Figures 6 and 7. Continuous power loss occurs near time equal to 1.48 seconds as the cage motion attempts to change to another steady solution. The results show the cage motion operating in a transition region between erratic motion and stable whirl. Correlating Figures 6, 7, and 8 gives evidence that the cage motion affects the power loss for the ball-to-inner race and ball-to-outer race contact. As the power loss

at the ball-to-cage pocket contact increases from impulsive to continual, the power loss at the ball-to-races contacts decreases.

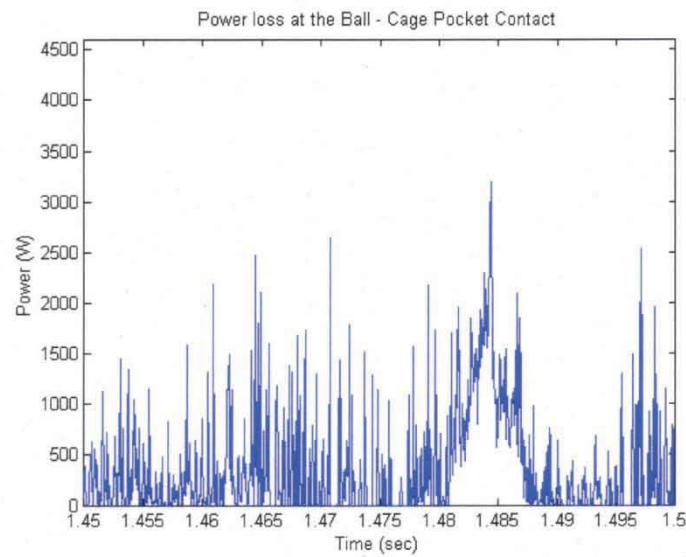
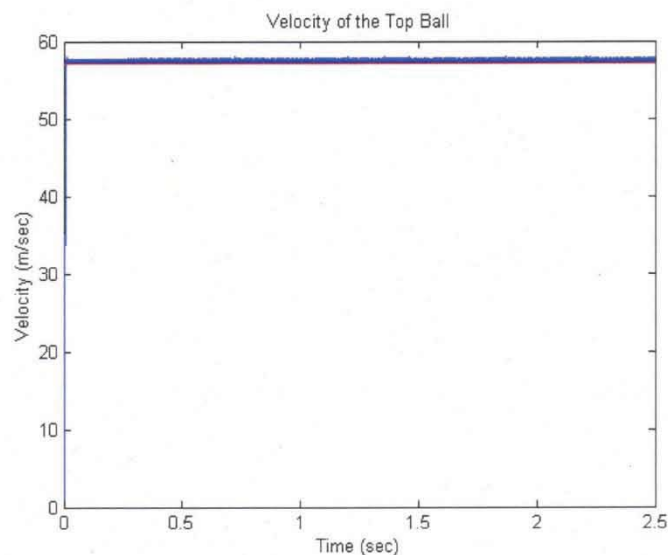


**Figure 9: Steady state power loss at the ball-to-cage pocket contact**

Additional cases are presented next to provide a clearer picture of the phenomena occurring due to different types of cage motion.

### 1.4 Additional Results

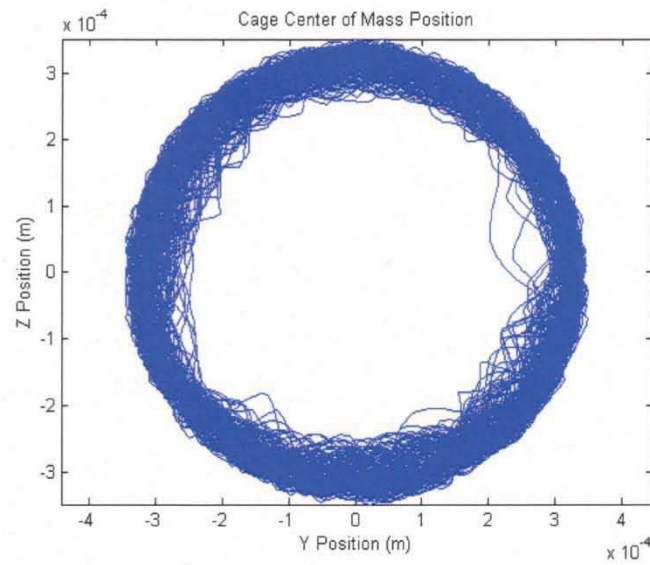
Ghaisas (2003) showed that erratic cage motion can be modified to whirl when the size one roller is larger than the others. The results for an oversized roller operating at 15,000 rpm and a 5,000 lb<sub>f</sub> axial load are presented in Figures 10 through 15



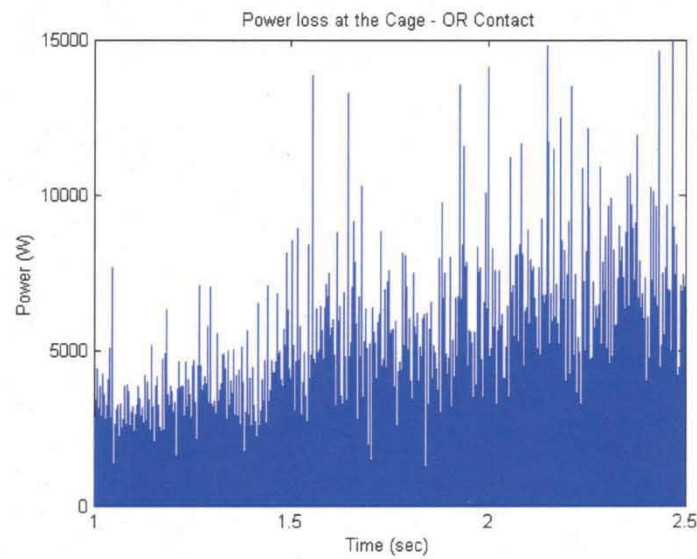
**Figure 10: Velocity of the initial top ball**

Figure 11 shows a well defined cage whirl when one roller is larger than the others. The cause for a well-defined cage whirl pattern can be attributed to ball-to-cage interactions. A secondary effect of the cage whirl, caused by one larger ball, is attributed to a circular motion of the inner race being pushed around by the larger ball. The inner race motion would be the dominating contribution to the cage whirl motion if the bearing contained an inner race guided cage, but the current study makes use of an outer race guided cage and thus the cage motion is governed by the traction forces at the ball-to-cage pocket contacts.

Cage-to-race power loss presented in Figure 12 shows an increase in cage-to-race interactions due to whirl motion of the cage. The cage maintains longer sliding contacts at the outer races causing a power loss increase.



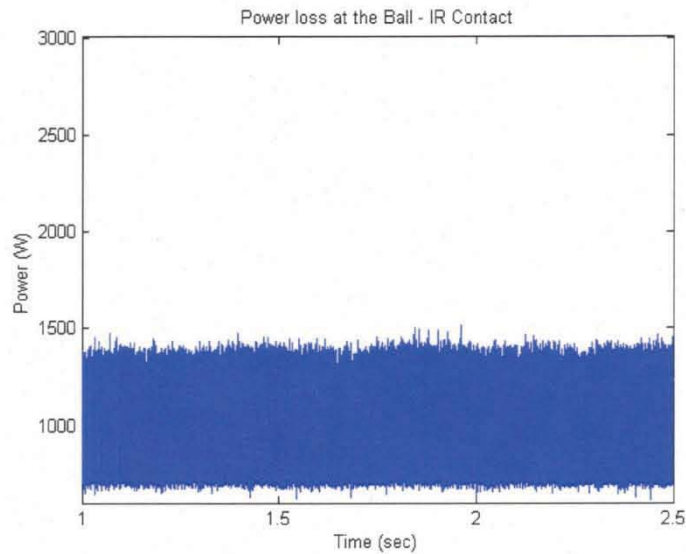
**Figure 11: Cage center of mass position**



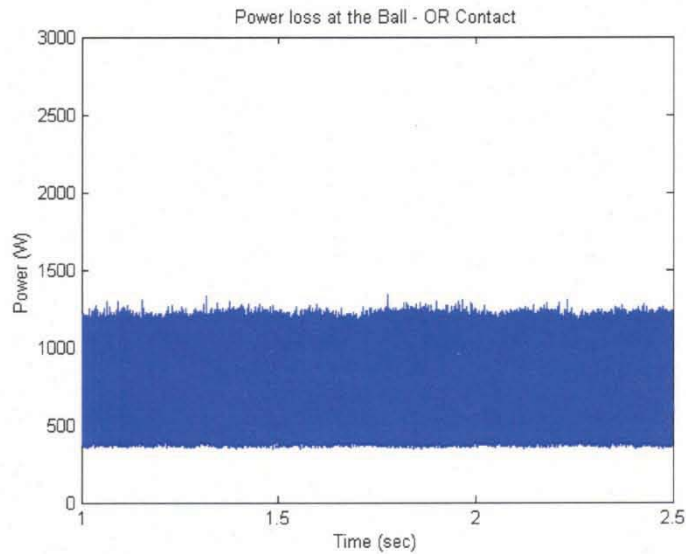
**Figure 12: Steady state power loss at the cage-to-outer race contact**



Figures 13 and 14 depict power loss values around the region of sharp decline seen in Figures 6 and 7, giving validation of the transitional cage behavior from erratic to whirl seen in Figure 9. Cage whirl causes reduced power loss values at the ball-to-outer race and ball-to-inner race contacts in comparison to erratic cage motion.

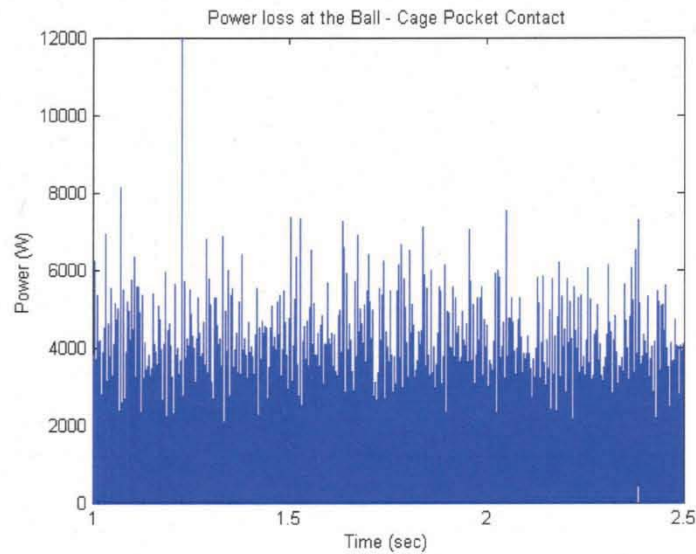


**Figure 13: Steady state power loss at the ball-to-inner race contact**



**Figure 14: Steady state power loss at the ball-to-outer race contact**

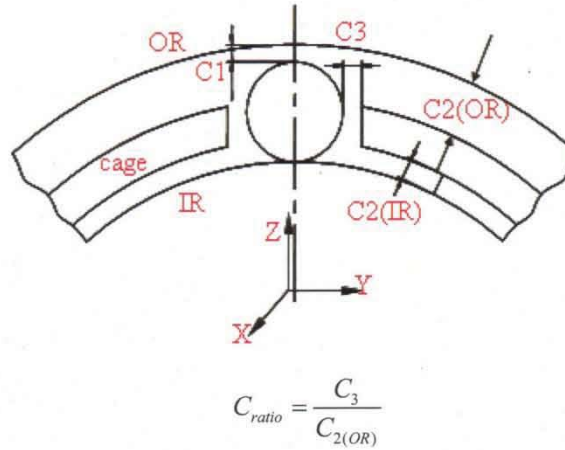




**Figure 15: Steady state power loss at the ball-to-cage pocket contact**

Figure 15 illustrates evidence of higher frequency ball-to-cage interactions causing an increase in power loss due to the oversize roller than those depicted in Figure 8.

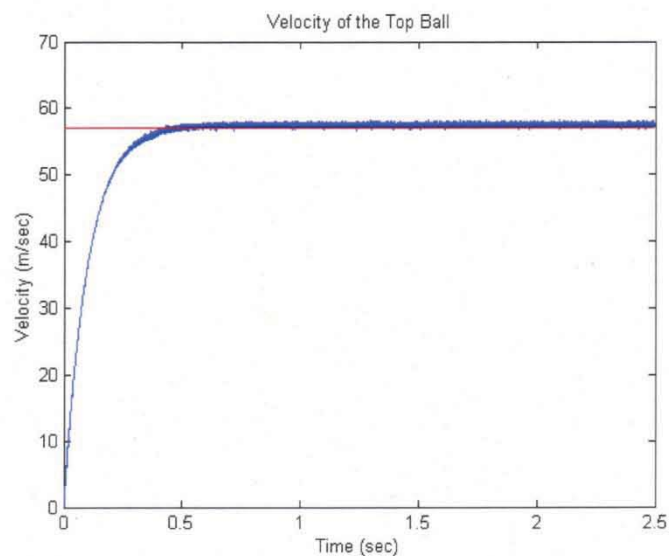
A second case investigated the effect of clearance ratio in the bearing; clearance ratio, defined as the cage pocket radial clearance to the cage-guiding race radial clearance shown in Figure 16. Small clearance ratios are known to initiate cage whirl (Ghaisas, 2003).



**Figure 16: Defining the clearance ratio.**

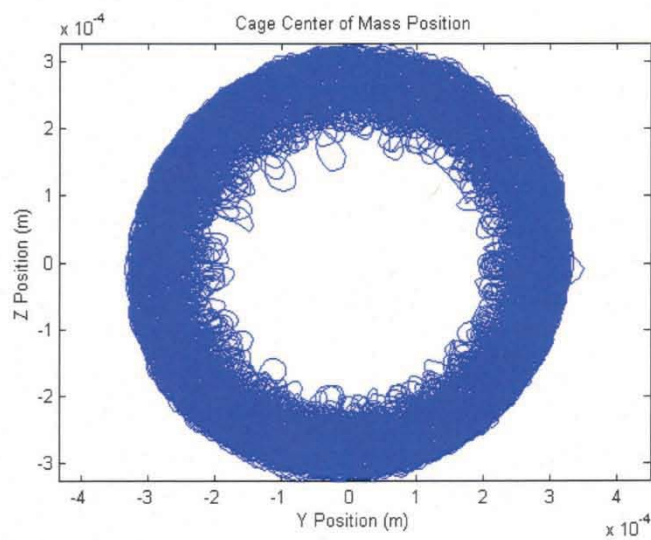
The clearance ratio ranged from 0.96 to 1.30 in the current study.

Clearance ratio studies in cylindrical roller bearings show a cage stability transition at a ratio of 1.0 (Ghaisas, 2003). Clearance ratios less than one caused stable cage whirl and ratios greater than one caused erratic cage motion. While the study investigated cylindrical roller bearings, similar trends have been observed in the current study of angular contact ball bearings with the transition region occurring at a slightly smaller clearance ratio. To investigate this effect, the cage pocket radial clearance was decreased to obtain a clearance ratio of 0.2 which caused the cage to exhibit a well defined whirl pattern. These findings are also in good agreement with the expected behavior of stable cage whirl. The results for an oversized roller operating at 15,000 rpm and a 5,000 lb<sub>f</sub> axial load are presented in Figures 17 through 22.



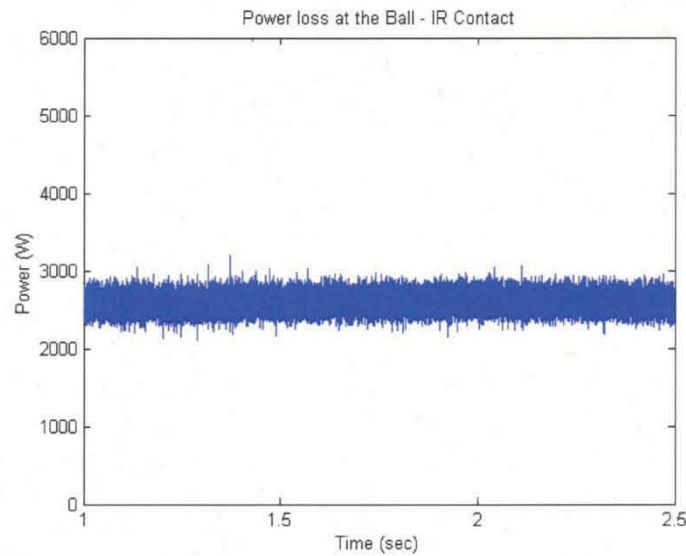
**Figure 17: Velocity of the initial top ball**

Figure 17 presents the translational velocity of the ball initially located along the Z axis to determine when the bearing model has reached steady state conditions.



**Figure 18: Cage center of mass position**

Figure 18 depicts stable cage whirl motion for the bearing model with a small clearance ratio, as expected. Figures 19 and 20 also show a decrease in ball-to-inner race and ball-to-outer race power loss as a result of cage whirl. This result is consistent with the power loss presented in Figures 6 and 7 when the cage transitions to whirl motion.



**Figure 19: Steady state power loss at the ball-to-inner race contact**

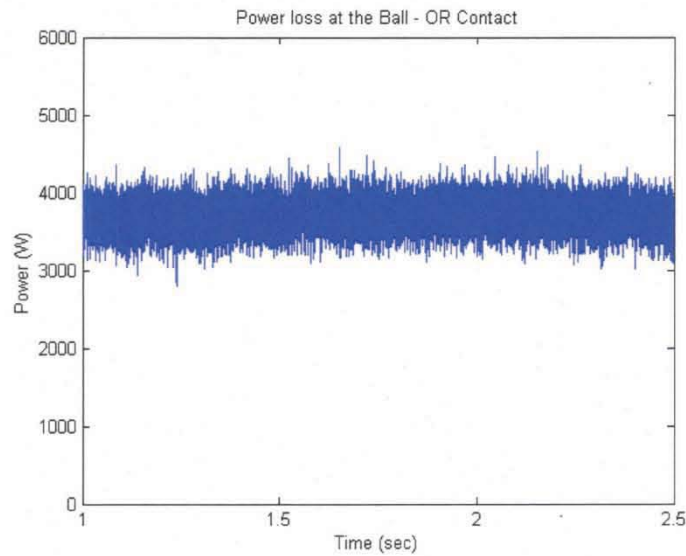


**Figure 20: Steady state power loss at the ball-to-outer race contact**

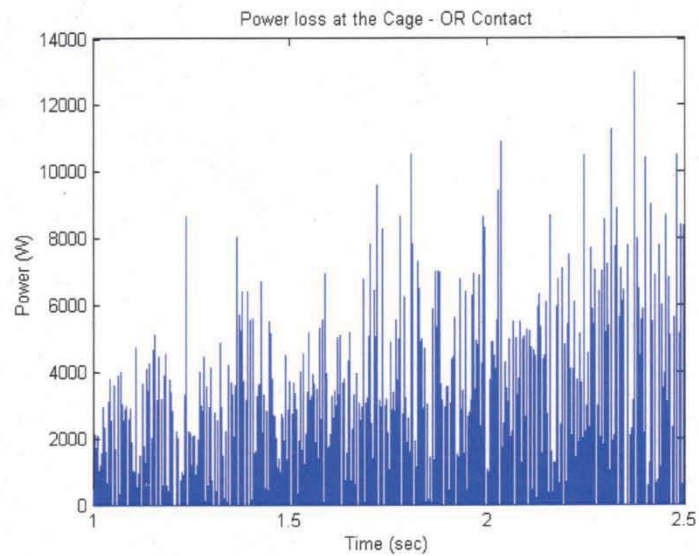


**Figure 21: Steady state power loss at the cage-to-outer race contact**

Figure 21 displays impulsive cage-to-outer race contacts. The power loss magnitudes are large but are very small in duration due to the short time impacts made between the two elements.

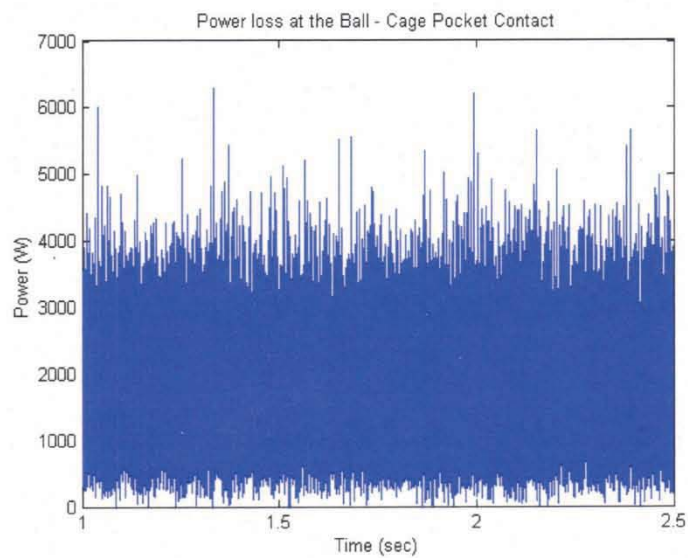


**Figure 22: Steady state power loss at the ball-to-cage pocket contact**

Traction forces at the ball-to-cage pocket contact cause cage whirl motion (Kingsbury, 1994). Figure 22 depicts a non-zero power loss for any point in time at the ball-to-cage contact, indicating at least one ball-to-cage pocket contact occurs. The increased contact between the ball and cage pocket due to the reduced clearances causes the cage whirl, as was shown previously in Figure 18.

### 1.5 List of References

Ghaisas, N., 2003, *Dynamics of Cylindrical and Tapered Roller Bearings Using the Discrete Element Method*, Master of Science thesis, Purdue University.

Gupta, P. K., 1991, "Modeling the Instabilities Induced by Cage Clearances in Ball Bearings", *Tribology Transactions*, Vol. 34, pp. 93-99.

Kingsbury, E., and Walker, R., 1994, "Motions of an Unstable Retainer in an Instrument Ball Bearing", *ASME Transactions*, Vol. 116, pp. 202-208.

Saheta, V., 2001, *Dynamics of Rolling Element Bearings Using Discrete Element Method*, Master of Science thesis, Purdue University.



**APPENDIX C**  
**Pradeep Gupta (PKG Inc) Contribution**

# Ball Bearing Dynamics as Affected by Raceway Defects

Presented at  
2008 AFRL/RZTM Bearing Modeling Summit  
WPAFB, OHIO  
Held at Holiday Inn, Fairborn, Ohio

Pradeep Gupta  
PKG Inc  
[guptap@PradeepKGuptaInc.com](mailto:guptap@PradeepKGuptaInc.com)

August 21, 2008

UTC Project C-247

# Project Outline

- ❖ Objectives
- ❖ Base line tool - ADORE
- ❖ Model Formulation
- ❖ Modeling Approach
- ❖ Customized subprogram for ADORE
- ❖ Summary

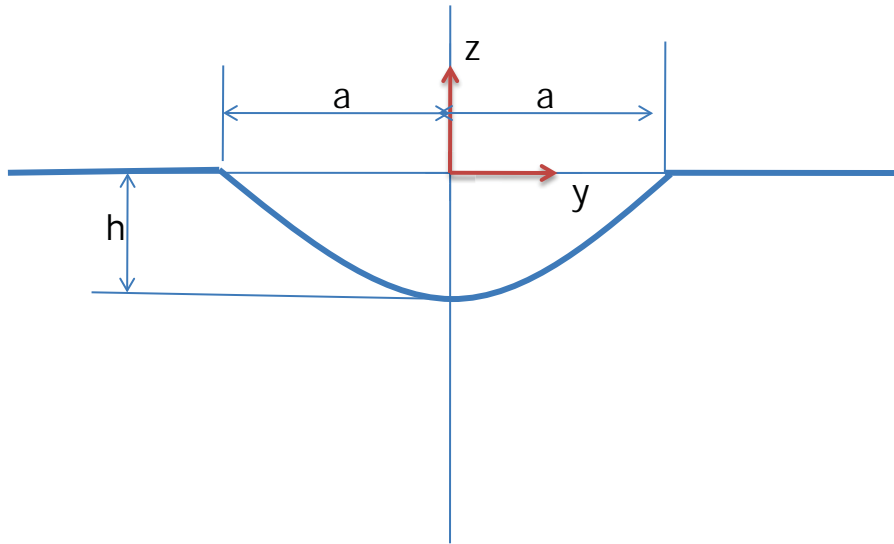
# Objectives

- Geometric modeling of race defect
- Model implementation as race geometry variation
- Bearing performance simulation as a function of defect geometry

# Base Line Tool - ADORE

- Generalized geometry
- Arbitrary variation in geometrical parameters
- Defect implementation via race radius variation
  - User programmable subprogram ADRX6
- Dynamic performance simulation as a function of defect parameters
  - Ball motion
  - Cage Motion

# Model Schematic



# Model Formulation

- Polynomial approximation

$$z = f(y) = (y-A_1)(y-A_2)(y-A_3)(y-A_4).....$$

- Normalization

$$y^* = y/a \quad z^* = z/h$$

- Boundary values

$$y^* = 0$$

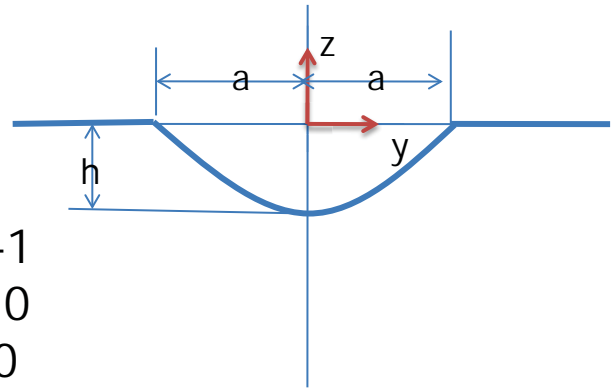
$$z^* = -1$$

$$y^* = 1$$

$$z^* = 0$$

$$y^* = -1$$

$$z^* = 0$$

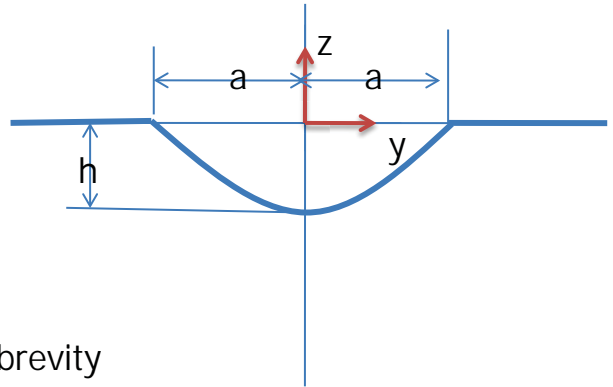




# Model Formulation

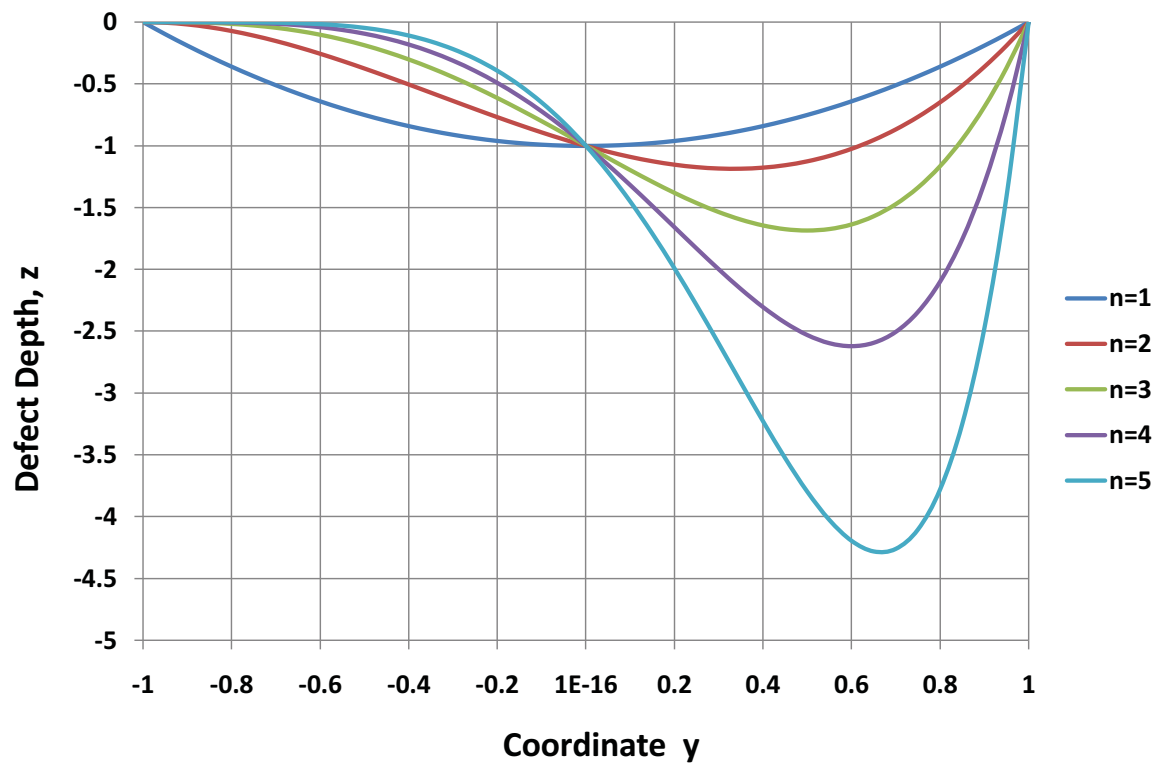
- Normalized polynomial after satisfying boundary values

$$z = (y - 1)(y + 1)^n$$

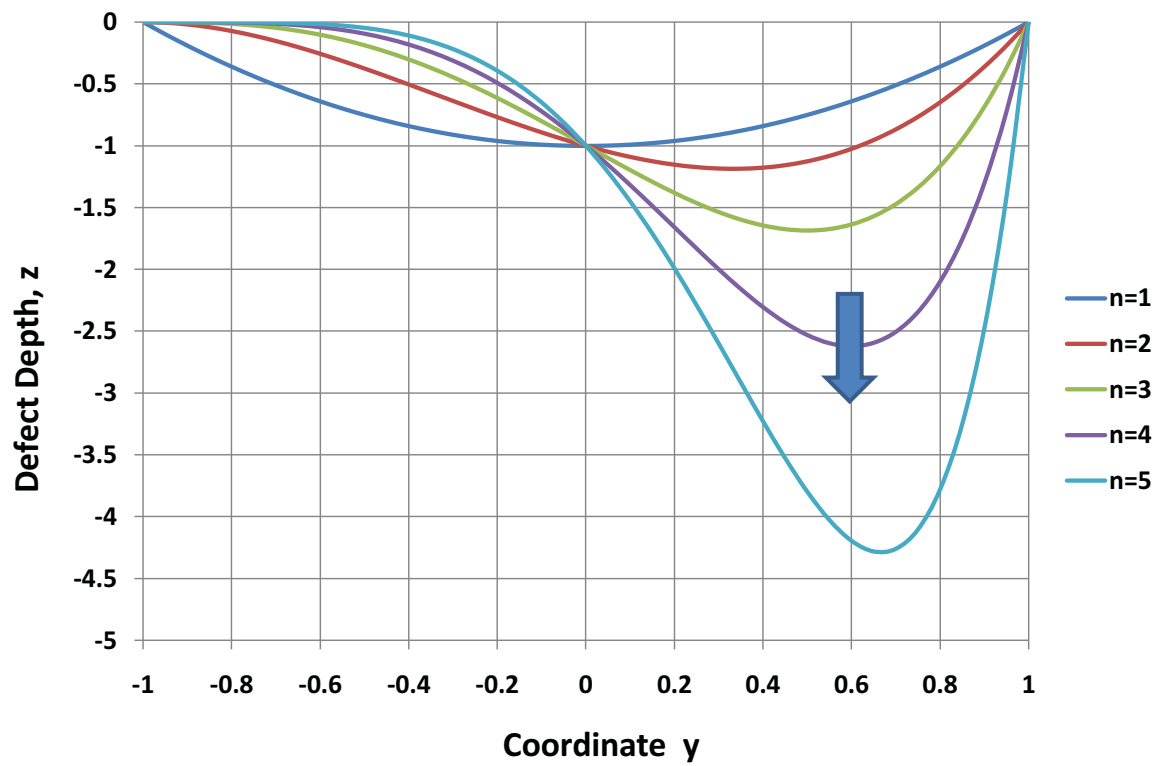


Asterisks (\*) have been dropped for brevity

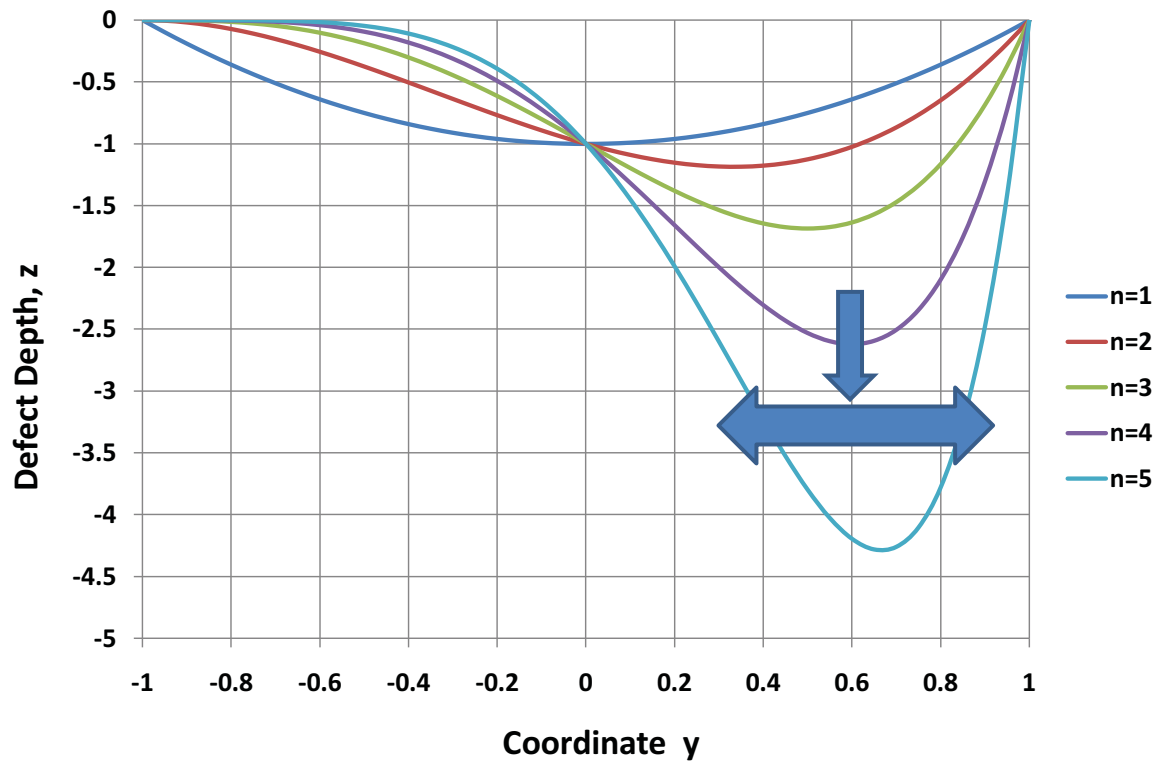
# Normalized Polynomial Model



# Elongated Defect Variation

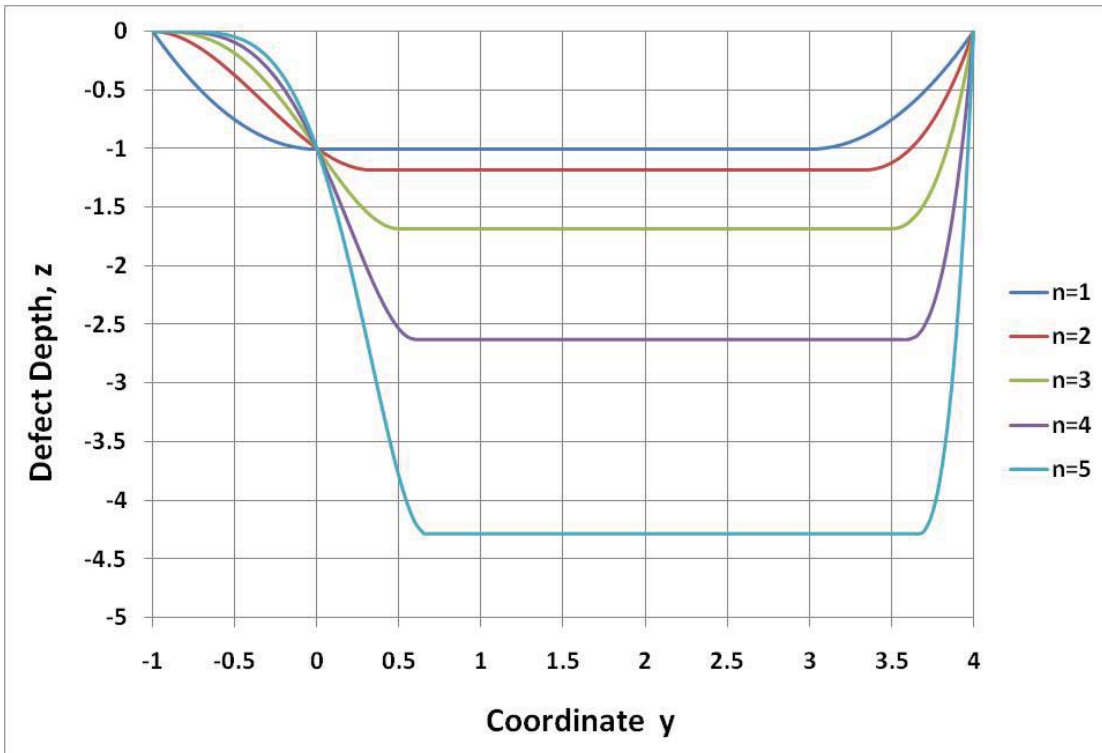


# Elongated Defect Variation



10

# Elongated Defect Model



# Modeling Approach

- Base performance simulation with no defects
  - Specified bearing geometry
  - Operating conditions
- Use the above solution as a baseline
- Customized subprogram for defect model
- Insert defect on the inner race with specified width and depth ( $a$  and  $h$ )
- Obtain dynamic simulation

# Project Outline

- ❖ Objectives
- ❖ Base line tool - ADORE
- ❖ Model Formulation
- ❖ Modeling Approach
- ❖ Customized subprogram for ADORE
- ❖ Bearing Performance Simulations

# Customize Subprogram ADRX6

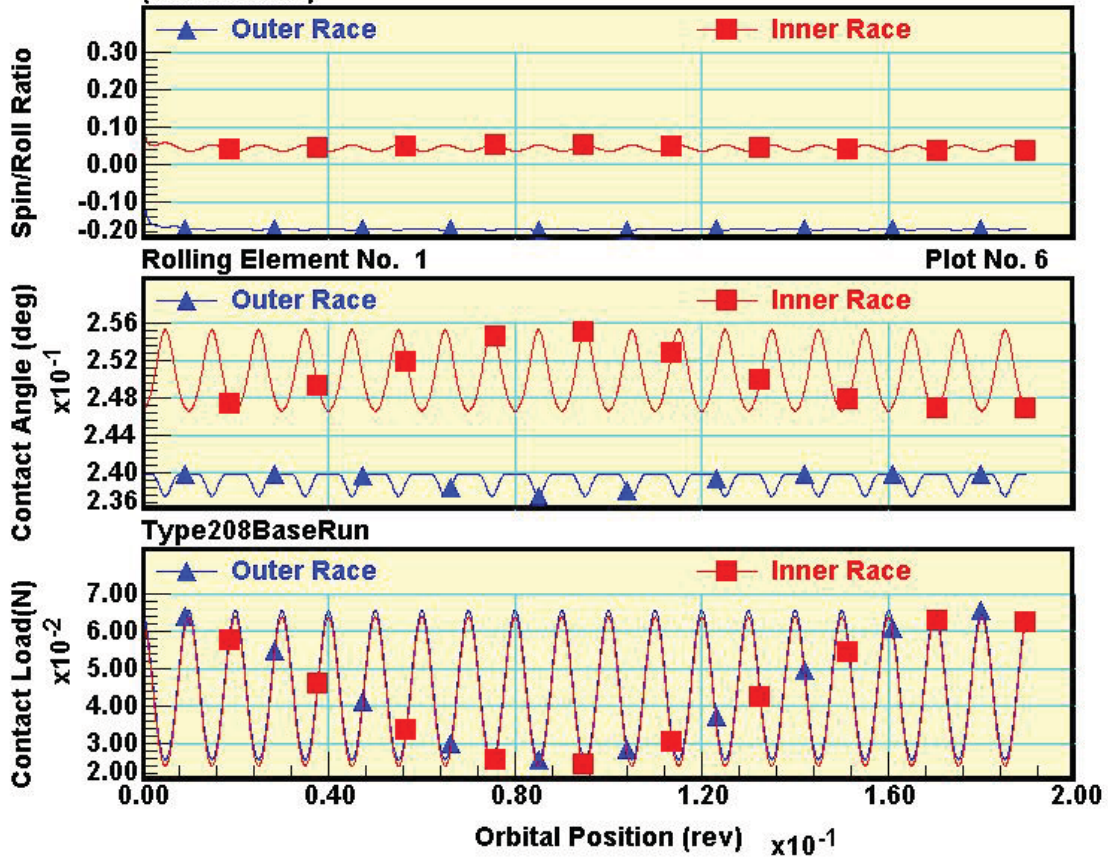
- Arbitrary race radius variation
- Parametric input corresponding to defect model
- Polynomial defect model
- Dynamic bearing performance simulations as a function of defect parameters

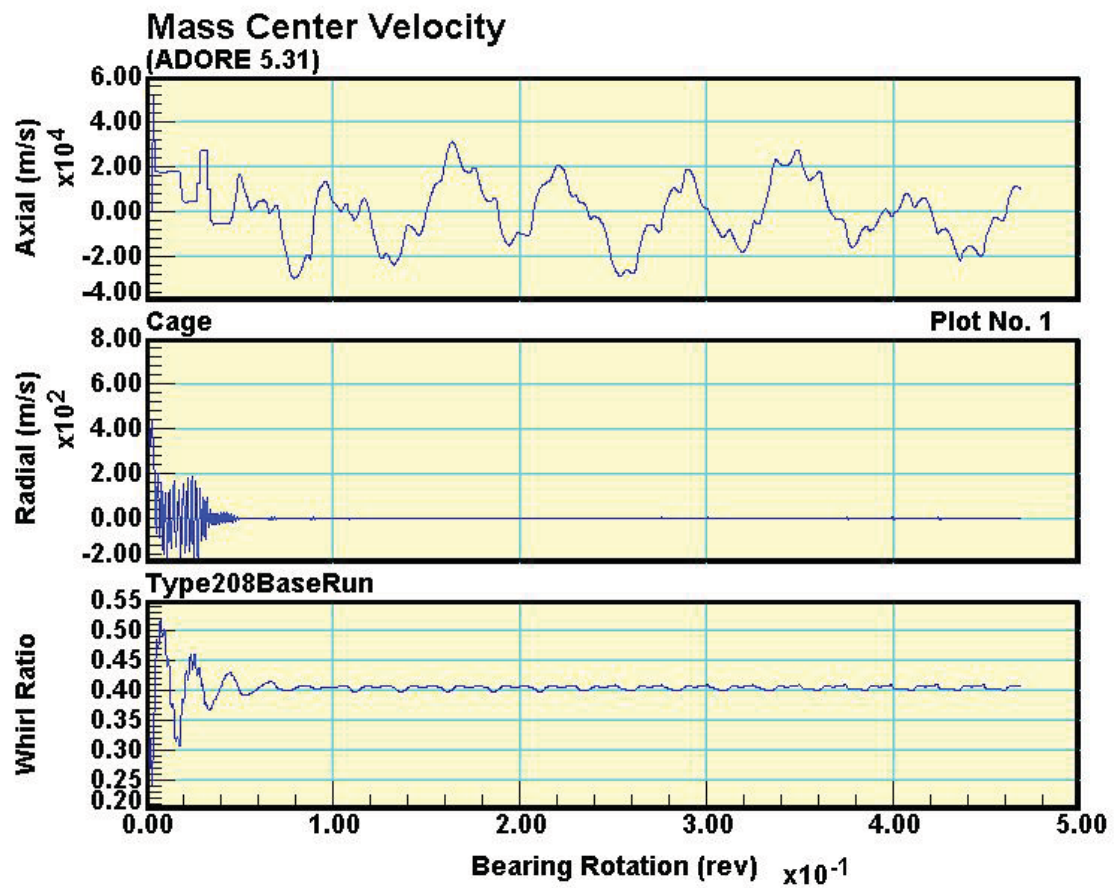


# Baseline Solution

- Type 208 ball bearing
- 40 mm bore, 80 mm OD
- 11 Silicon nitride balls, 12.7 mm dia
- 22 ° contact angle
- Outer race guided Steel cage
- 1 gm-cm unbalance
- 2,000 N Thrust, 1,000 N Radial
- 10,000 rpm
- MIL-L-7808 lubricant

# Rolling Element / Race Interaction: Set #1 (ADORE 5.31)

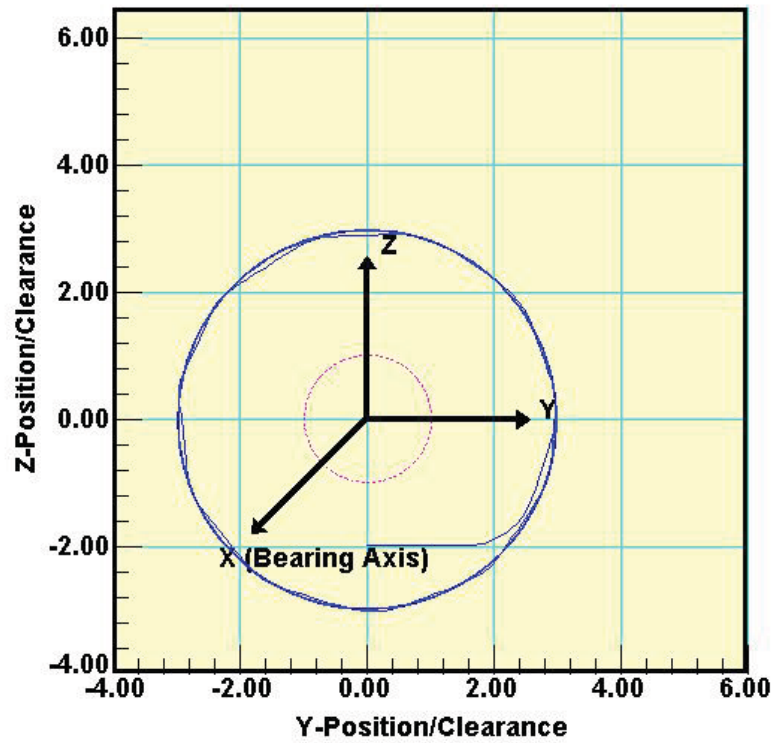


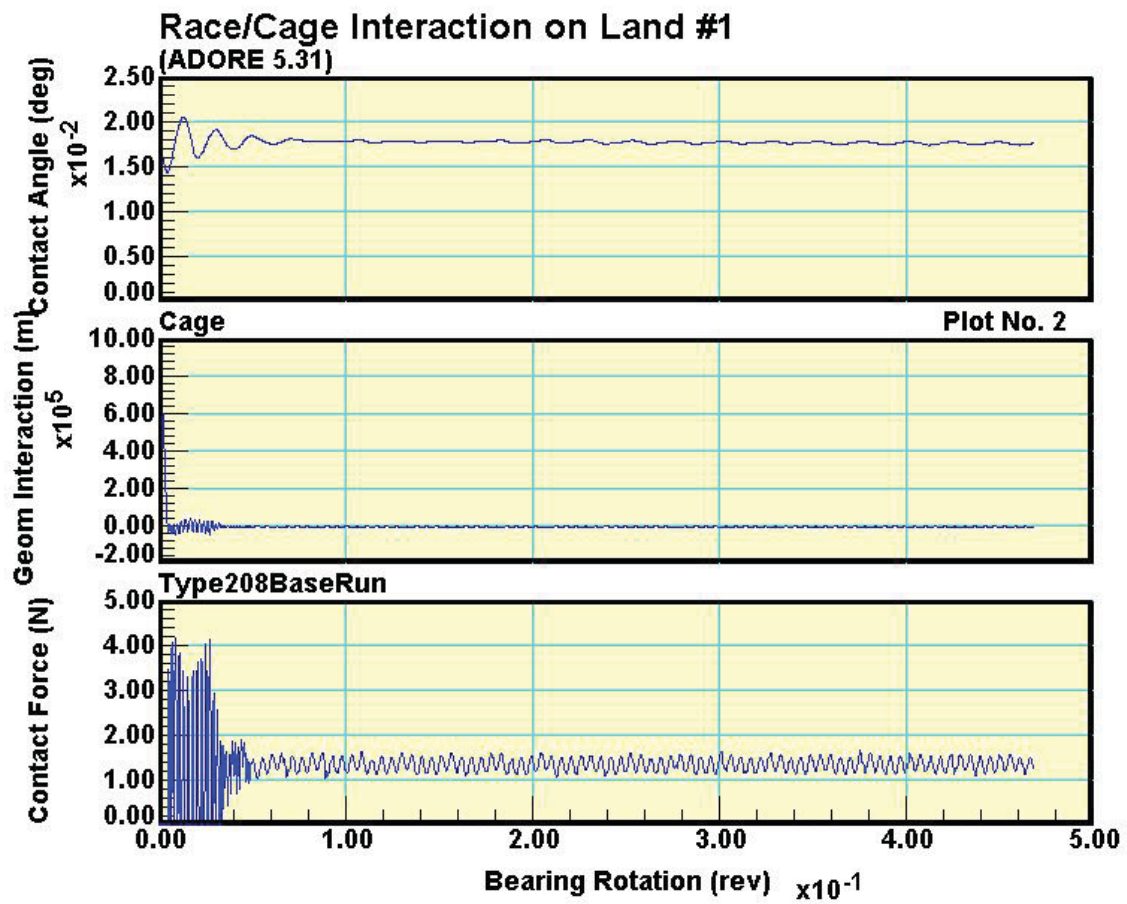


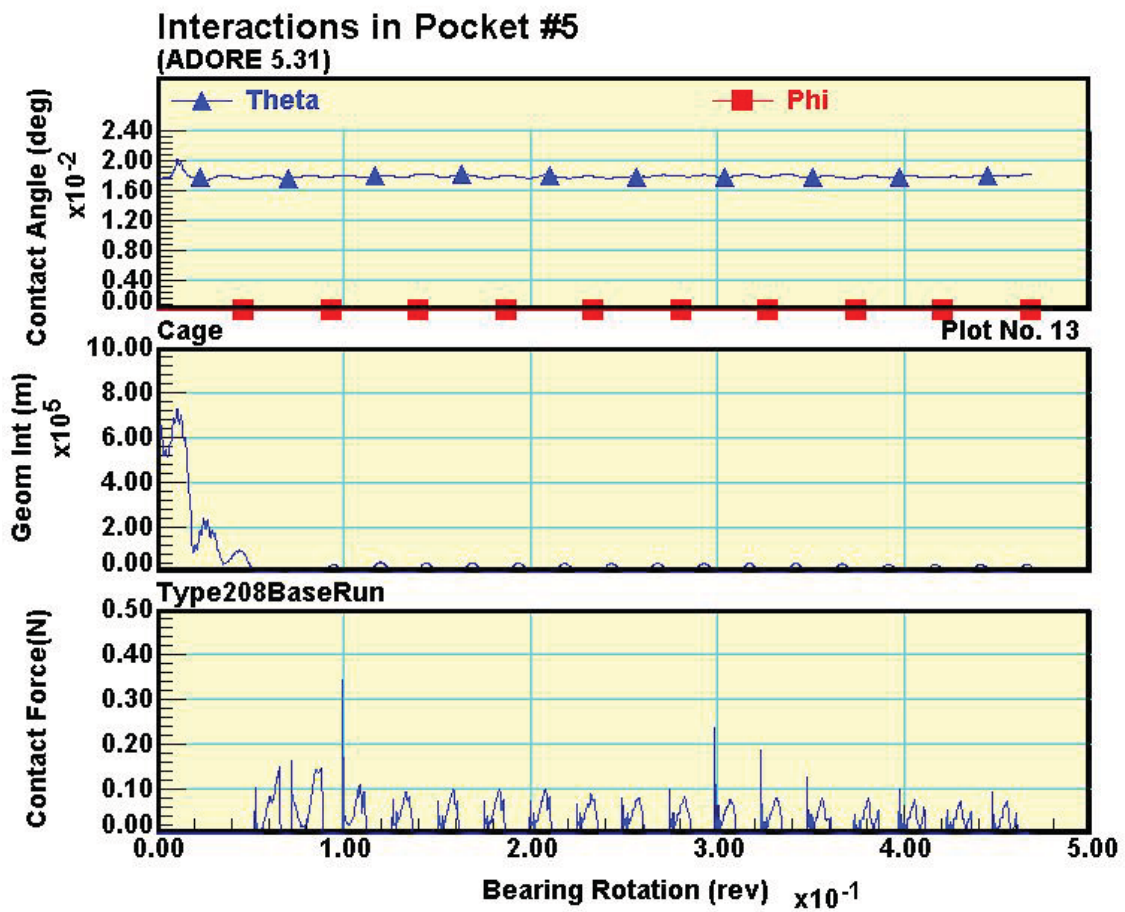
**Mass Center Whirl**  
(ADORE 5.31)

**Type208BaseRun**  
**Cage**

**Plot No. 5**







## Overall Performance Parameters

- Time-Averaged Heat Generation  
16.5 Watts
- Time-Averaged Cage Wear Rate  
 $1.01 \times 10^{-11} \text{ m}^3/\text{s}$

$$W = \frac{1}{T} \int_0^T \frac{KQ(t)V(t)}{H} dt$$

# Key Parameters for Evaluation of Bearing with Race Defect

- **Heat Generation Ratio**

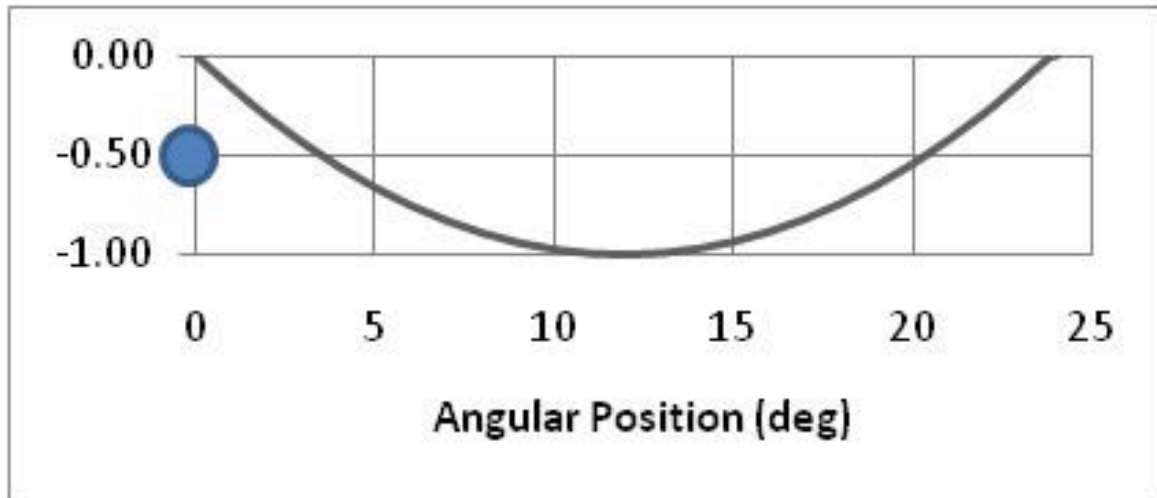
Time-Averaged heat generation of bearing with race defect divided by that of the baseline bearing

- **Cage Wear Ratio**

Time-Averaged cage wear rate of bearing with race defect divided by that of the baseline bearing

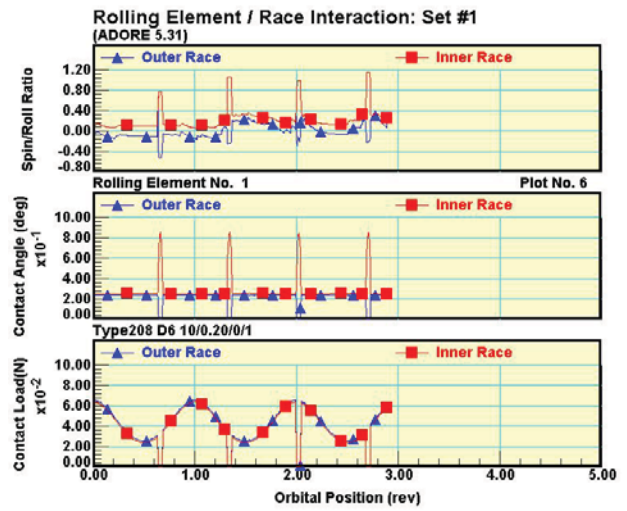
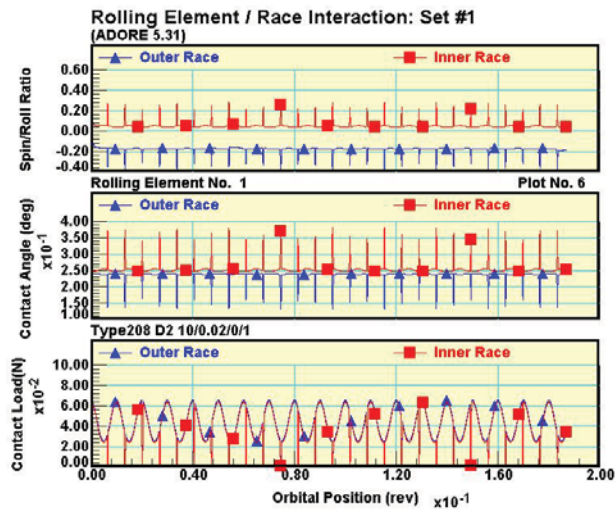


# Small Parabolic Defect 10mm

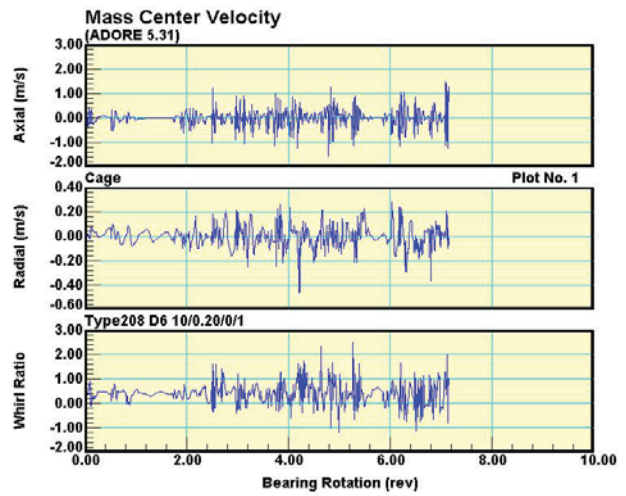
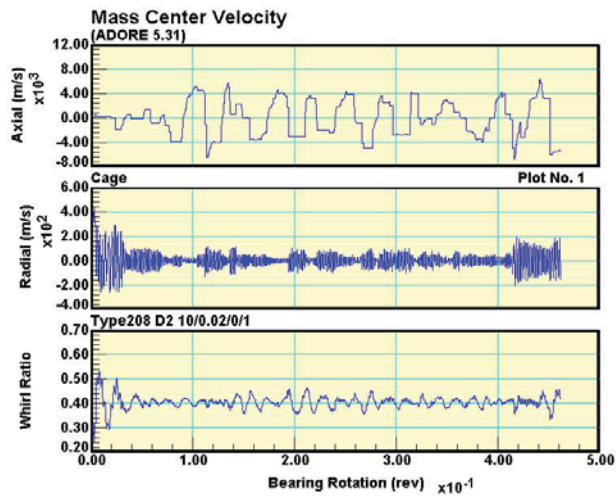


23

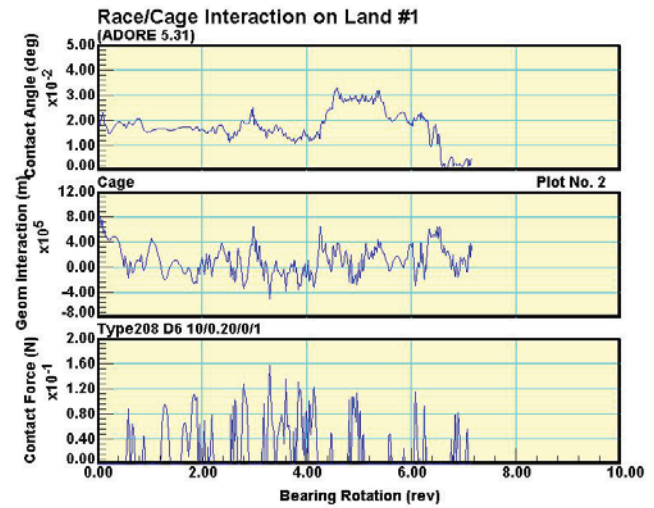
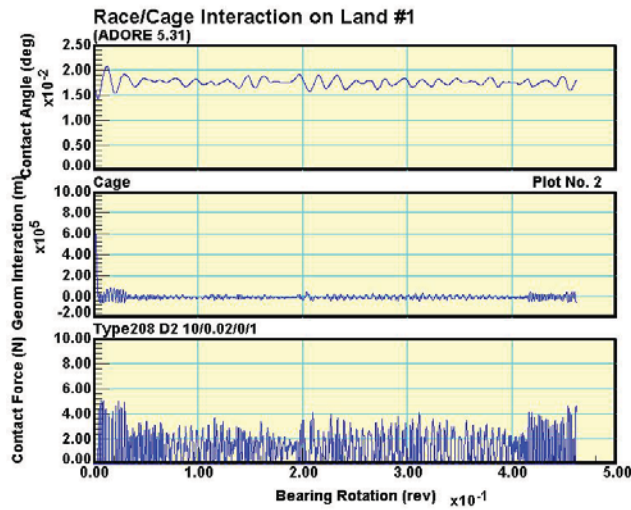
# Ball/Race Interaction



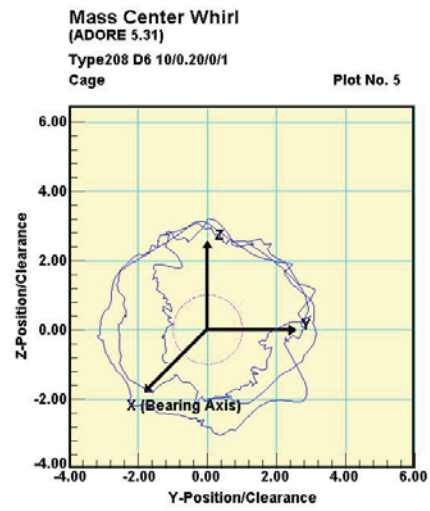
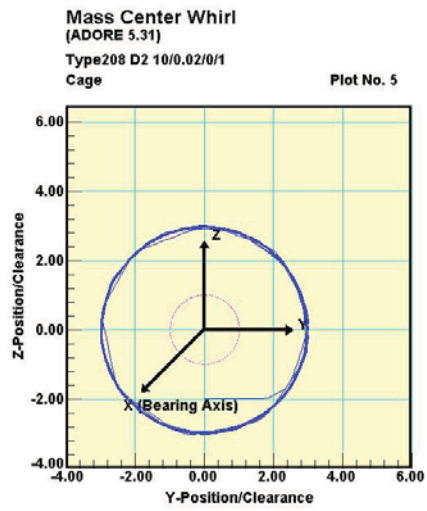
# Cage Mass Center Velocity



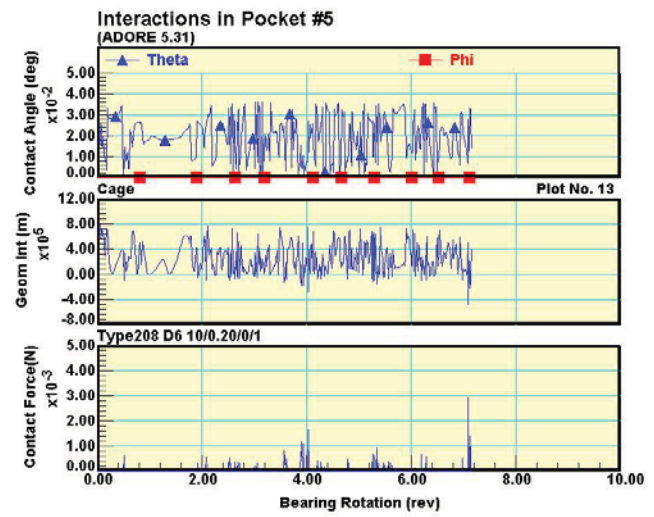
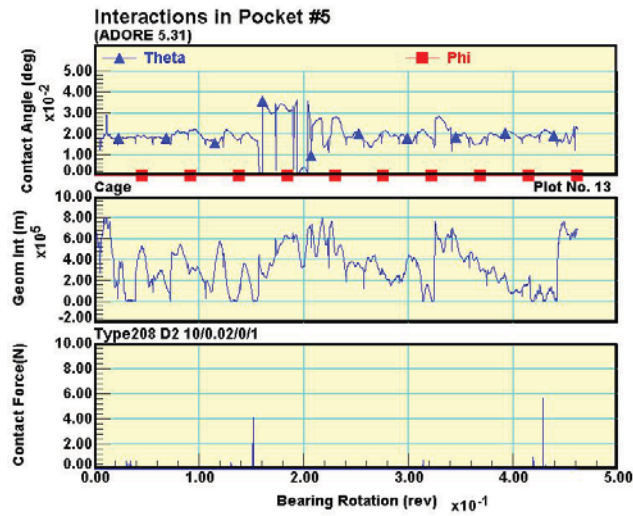
# Cage/Race Land Interaction



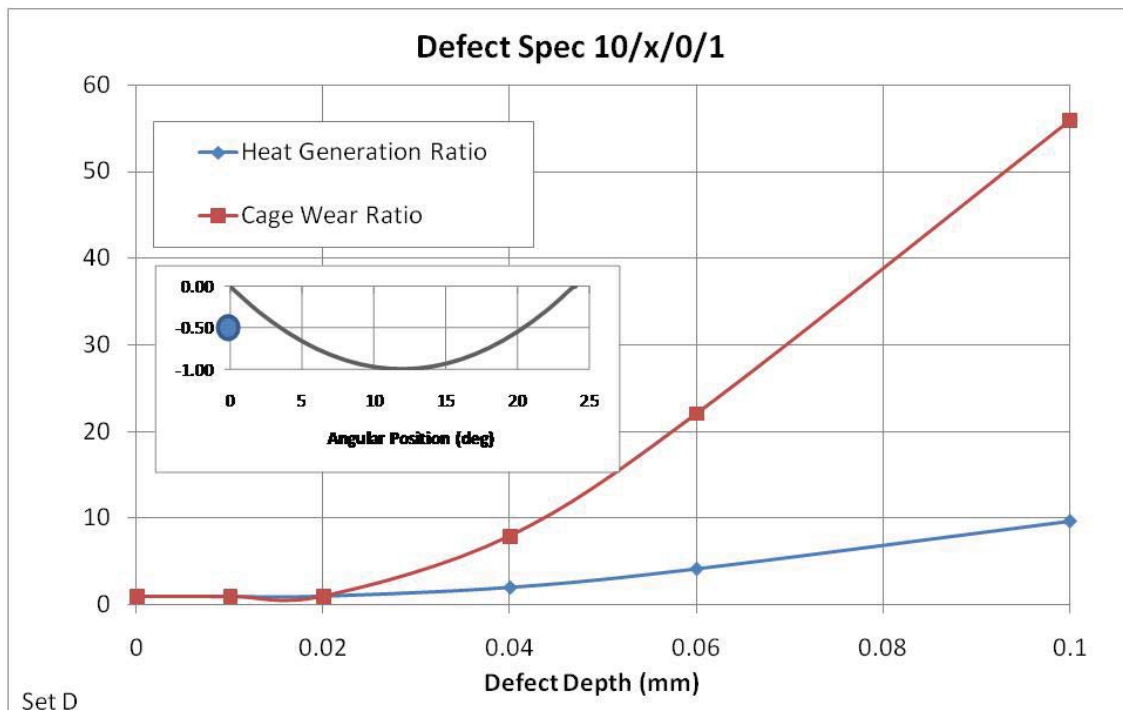
# Cage Whirl Orbits



# Cage Pocket Interaction

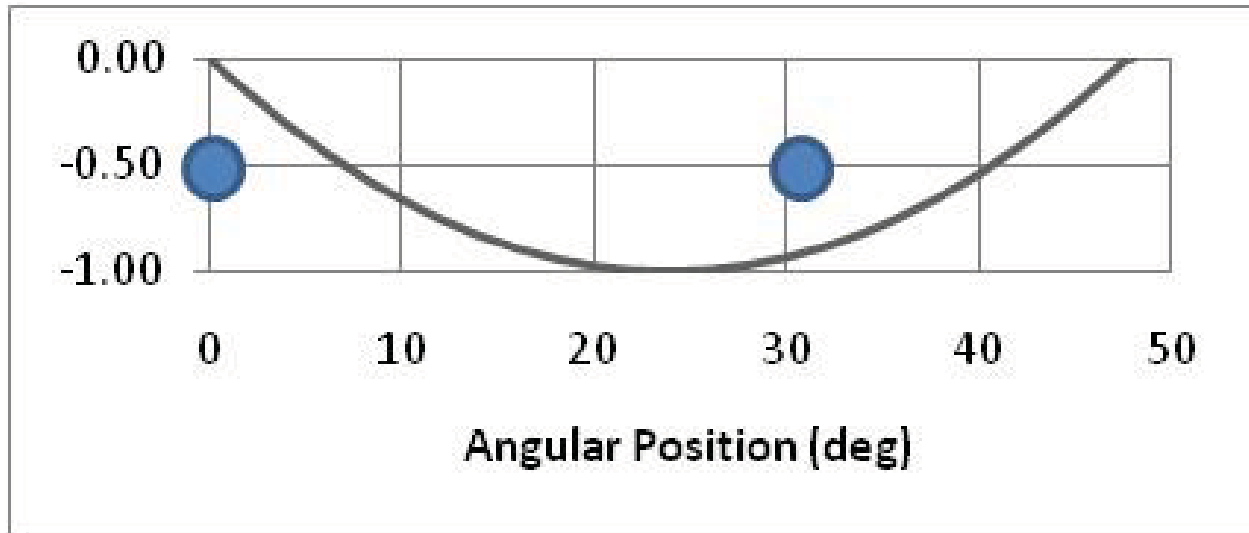


# Overall Performance Parameters



29

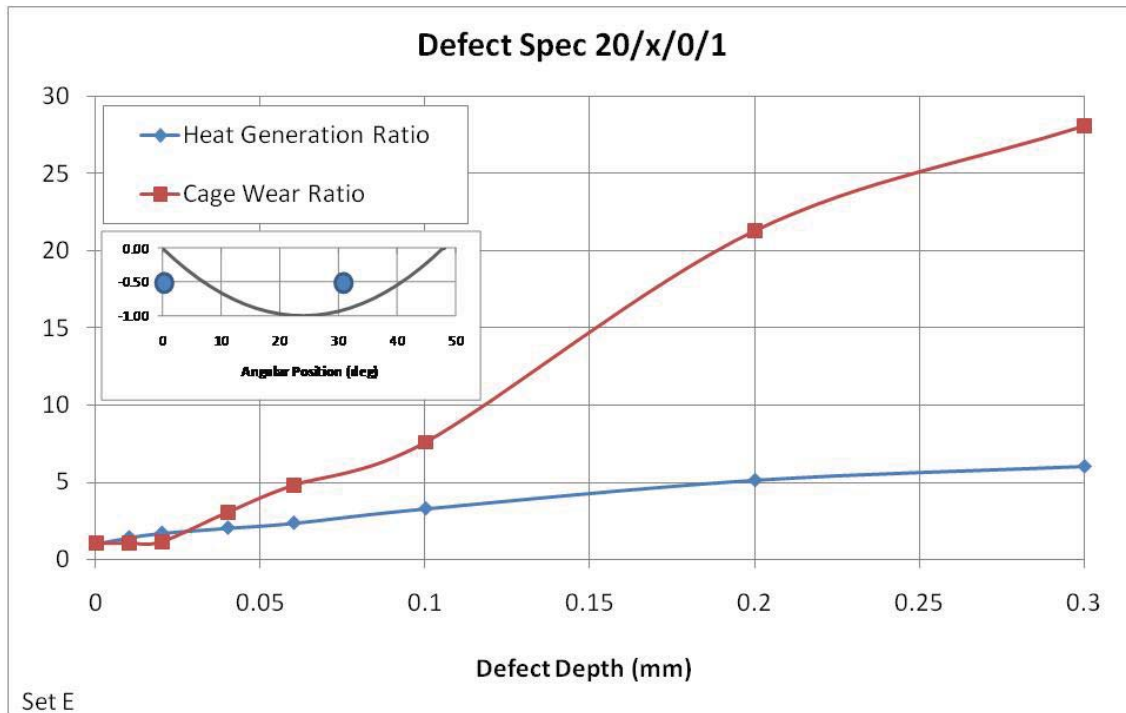
## Larger Parabolic Defect 20mm



30

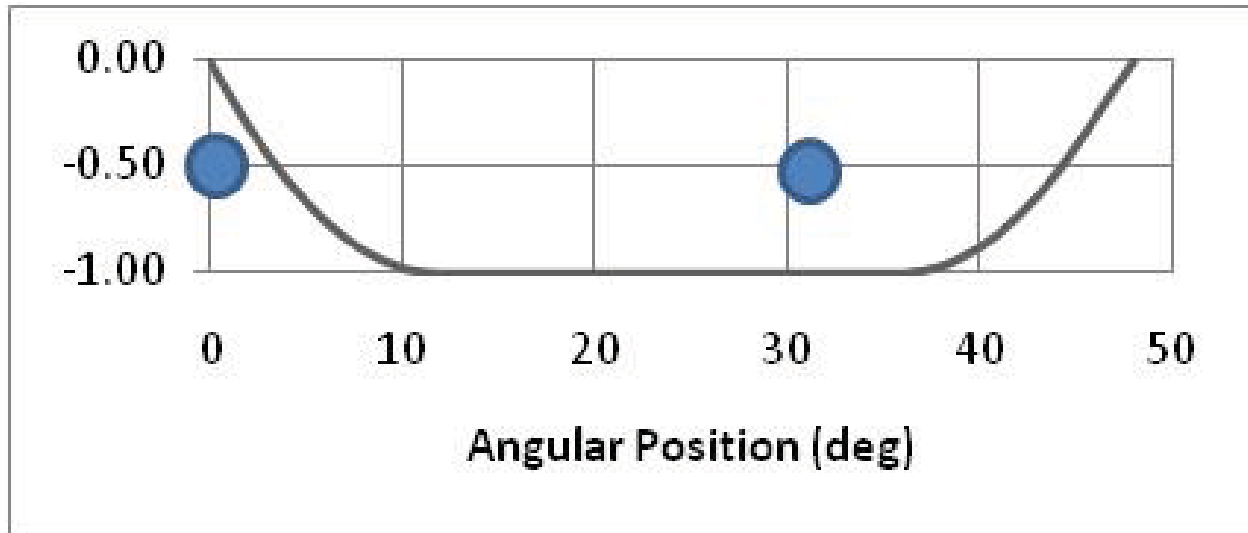


# Performance Parameters



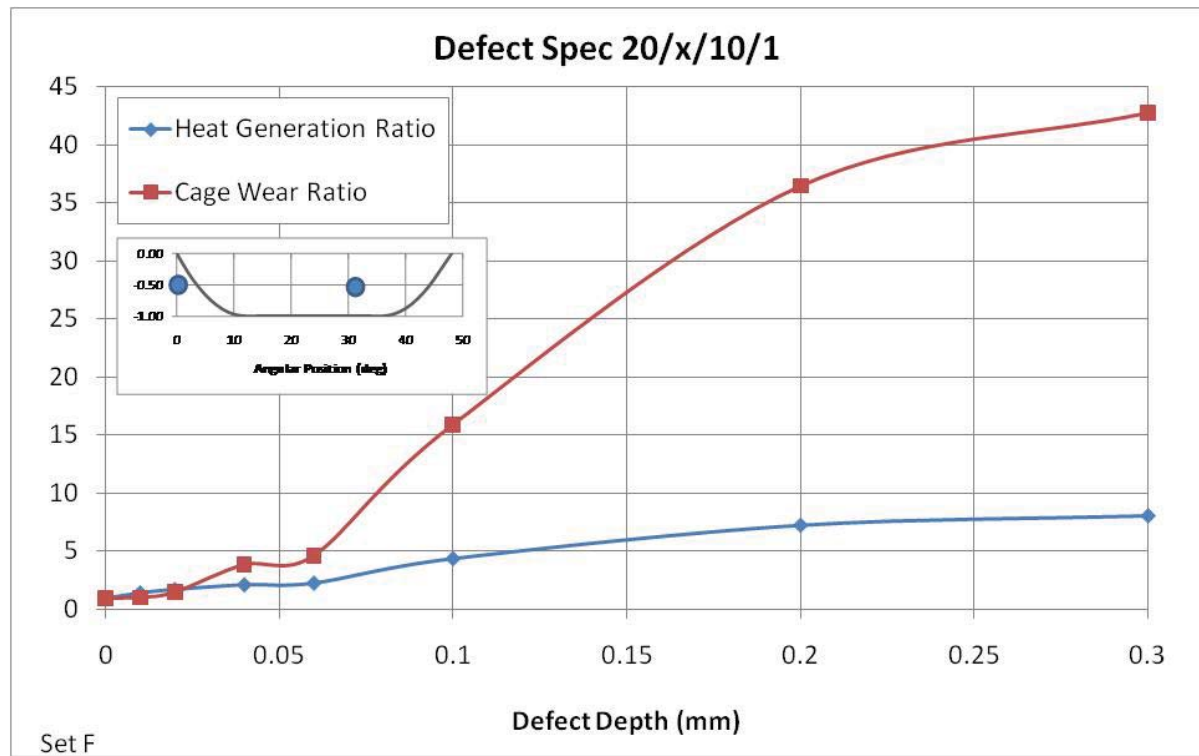
31

## Elongated Parabolic Defect 20mm



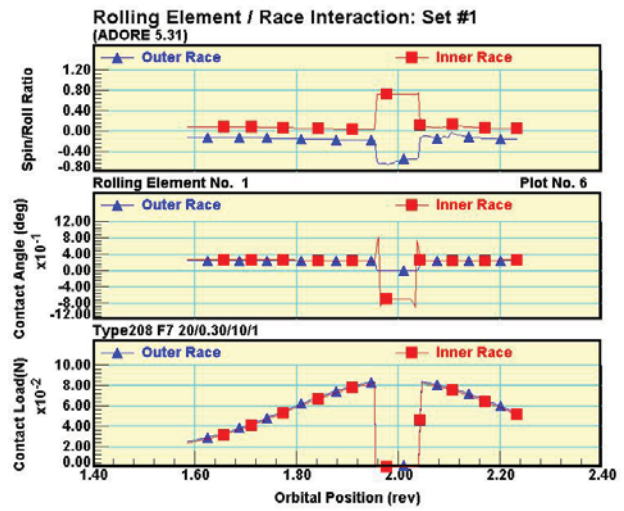
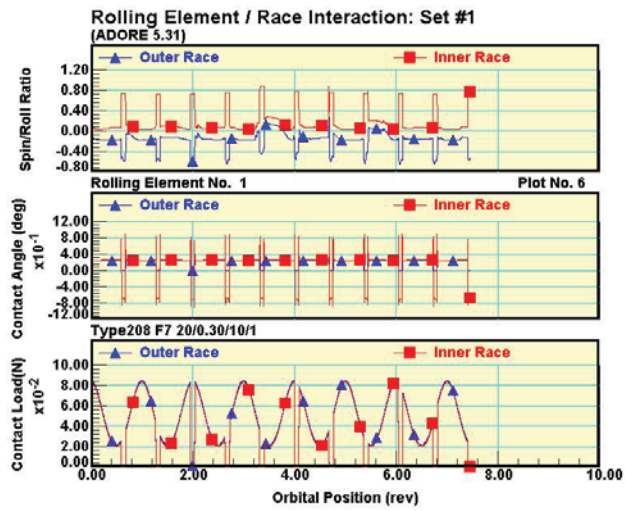
32

# Performance Parameters

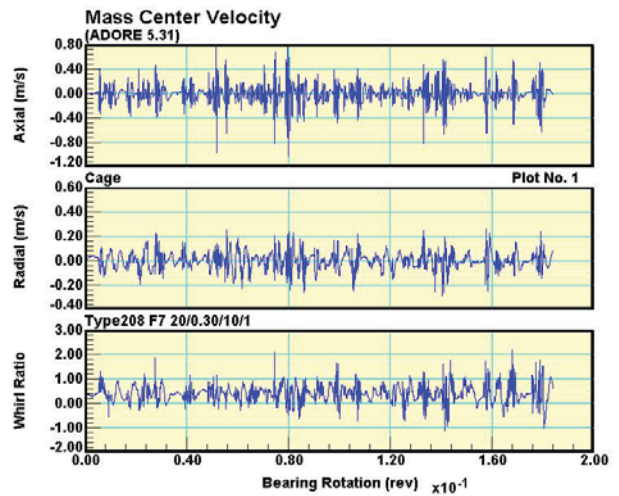
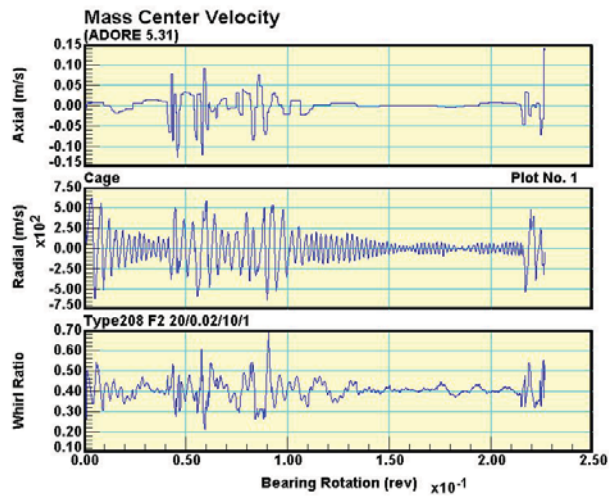


33

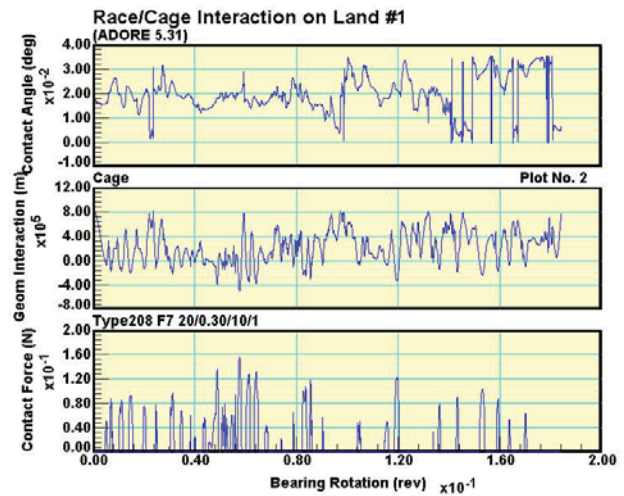
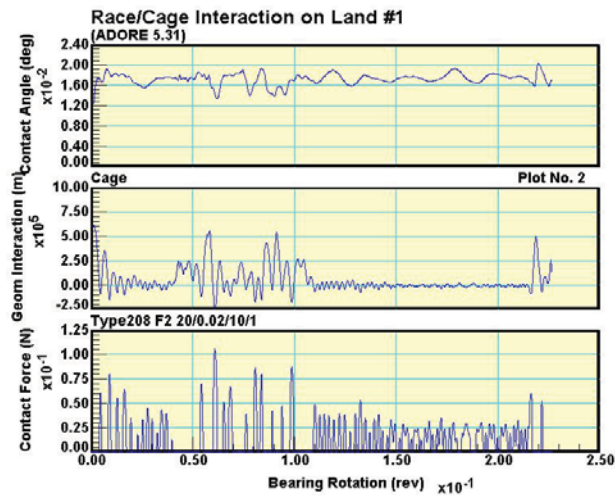
# Ball/Race Interaction



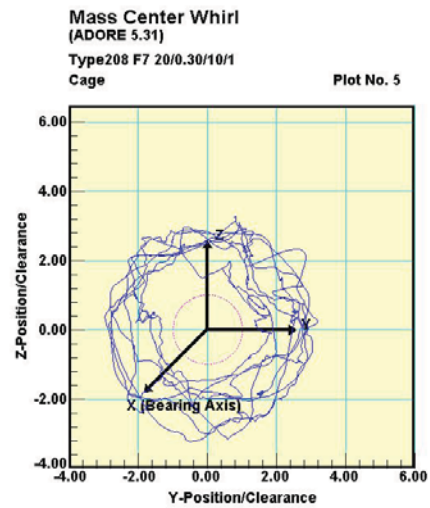
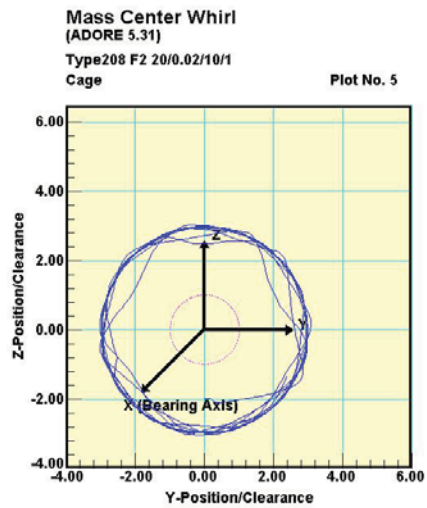
# Cage Mass Center Velocities



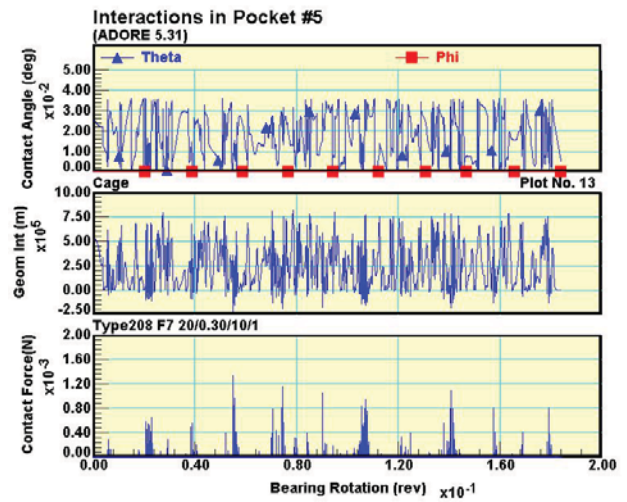
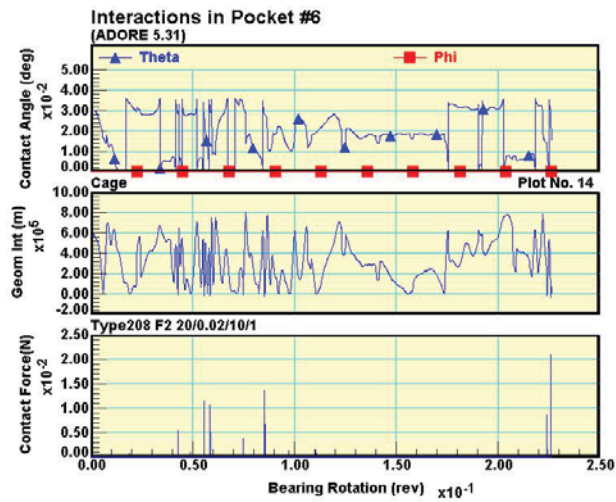
# Cage/Race Interaction



# Cage Whirl Orbits

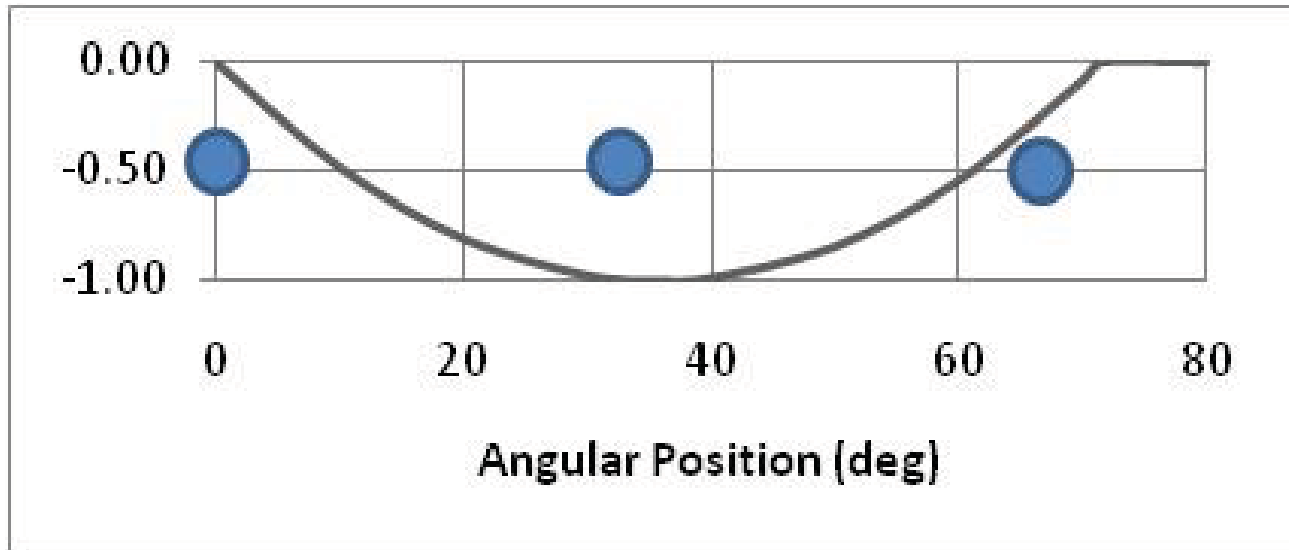


# Cage Pocket Interactions



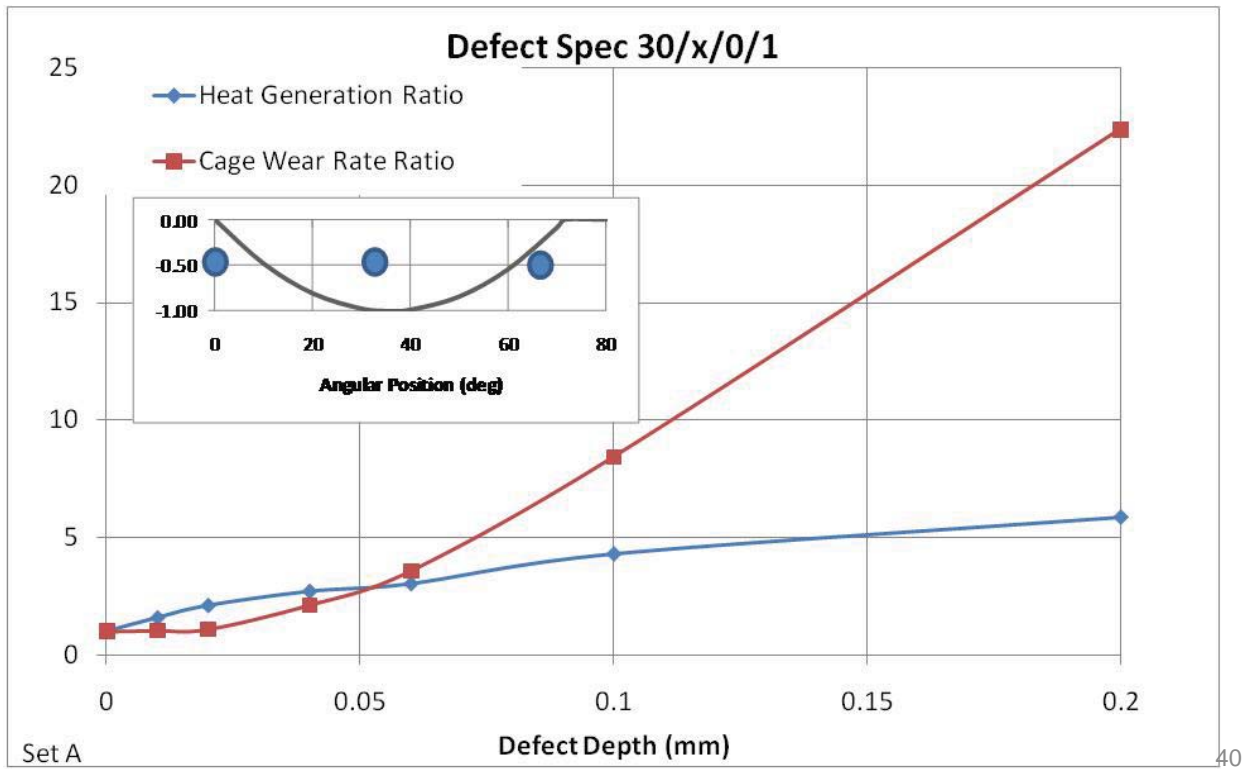


# 30mm Parabolic Defect

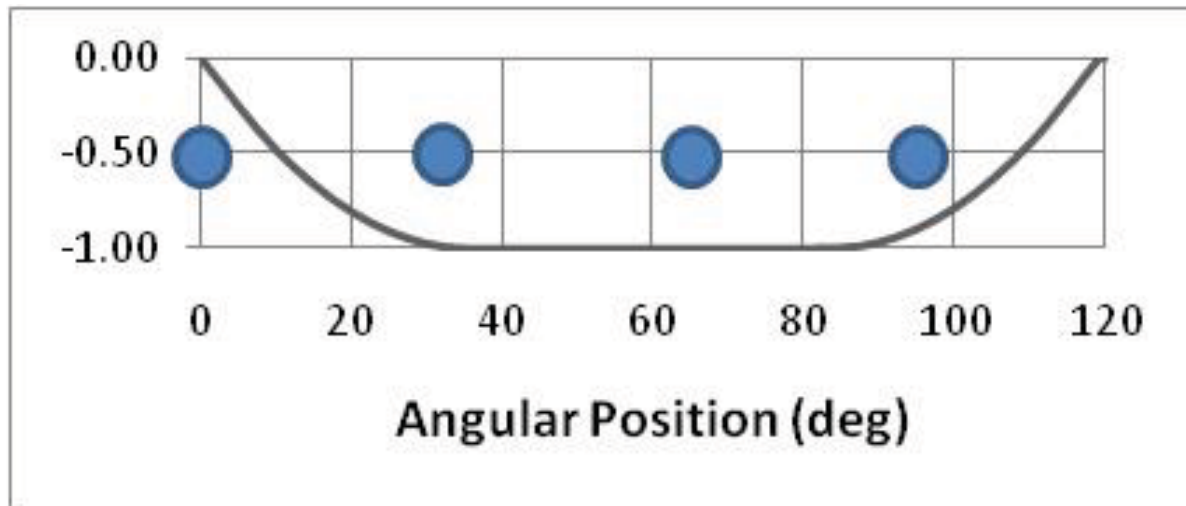


39

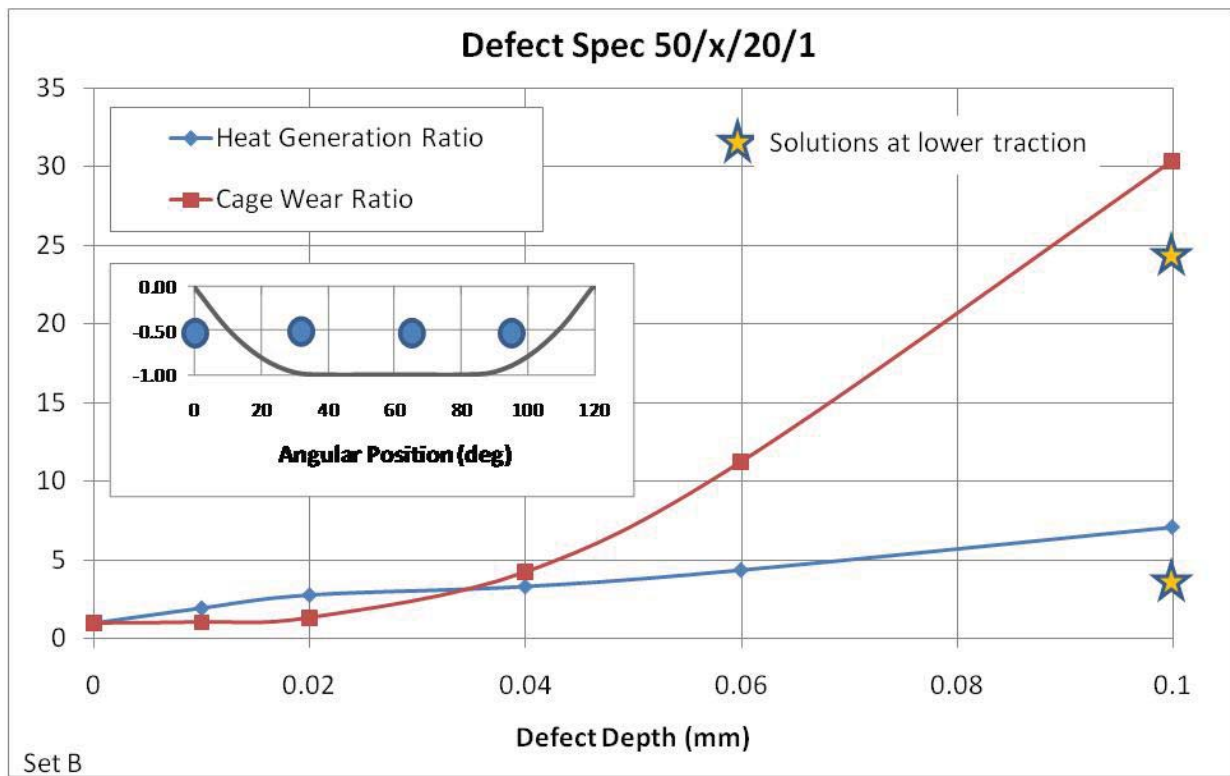
# Performance Parameters



# 50mm Elongated Defect

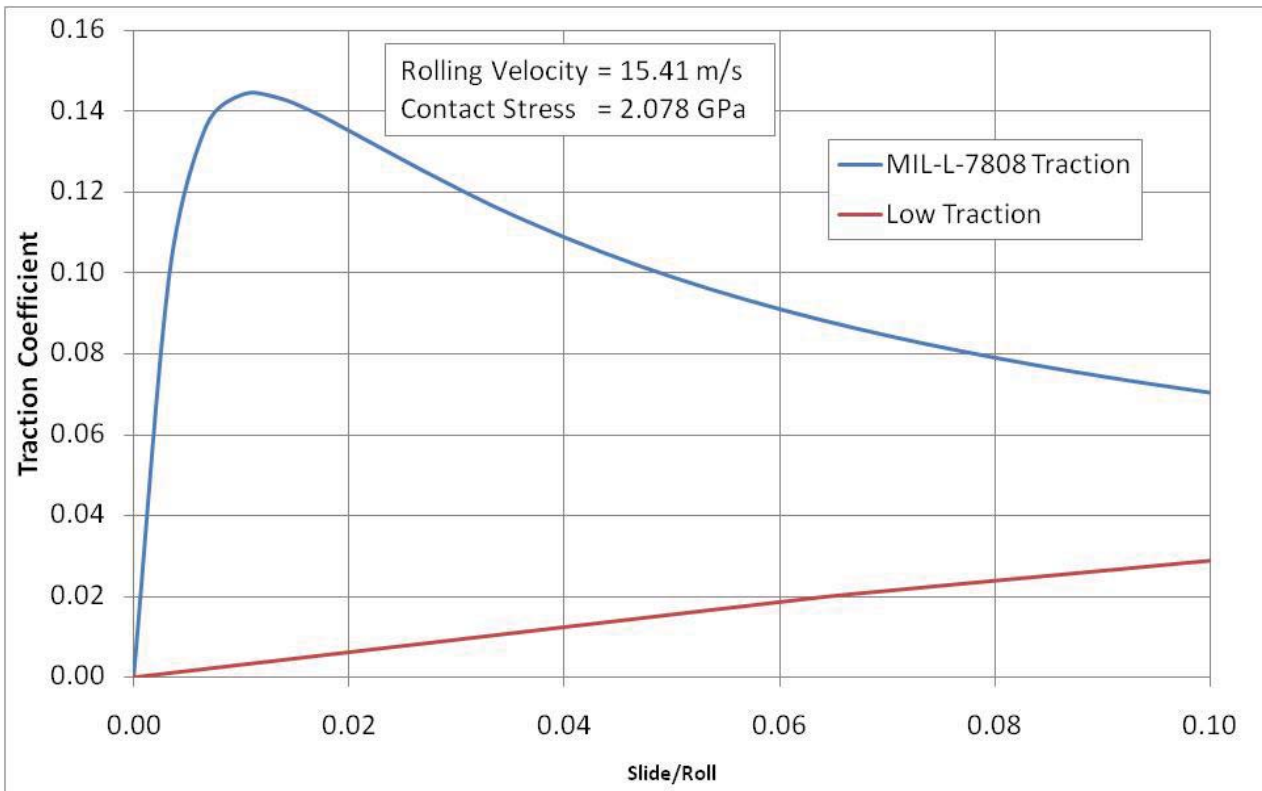


# Performance Parameters



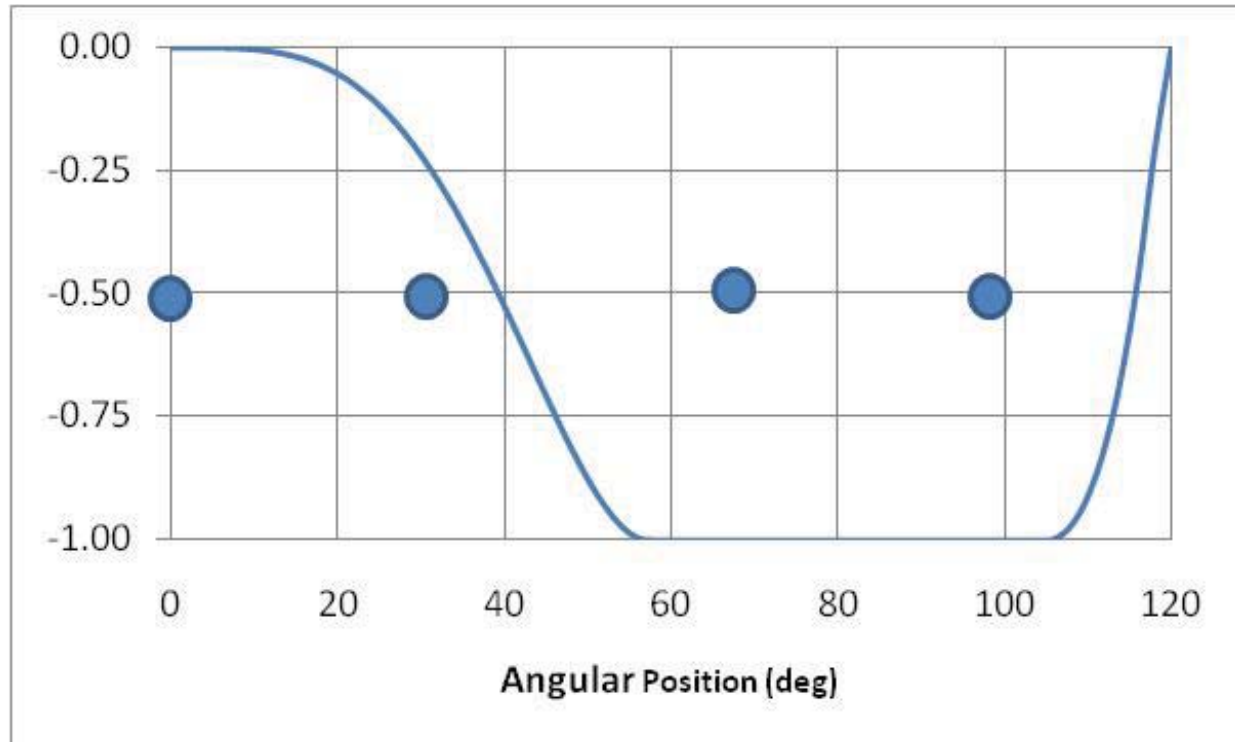
42

# Traction Curves



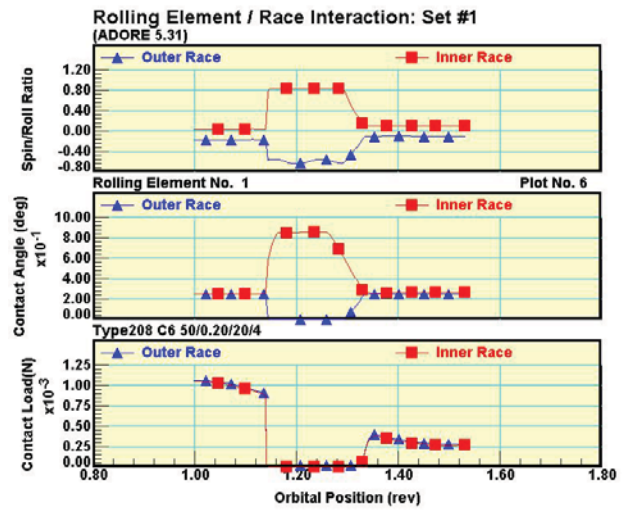
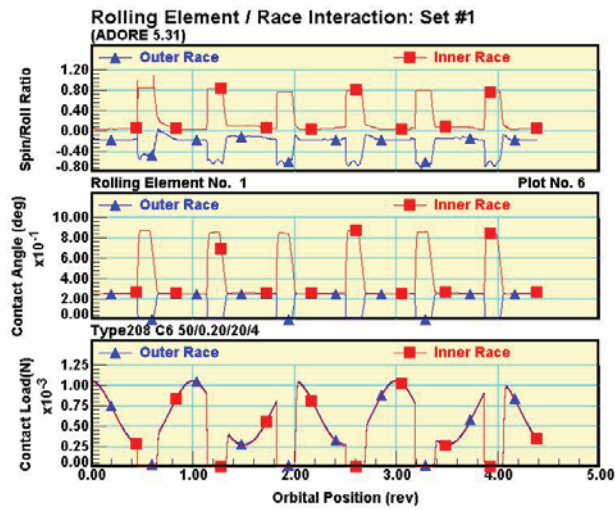
43

## 50mm Elongated Defect Higher Order Polynomial

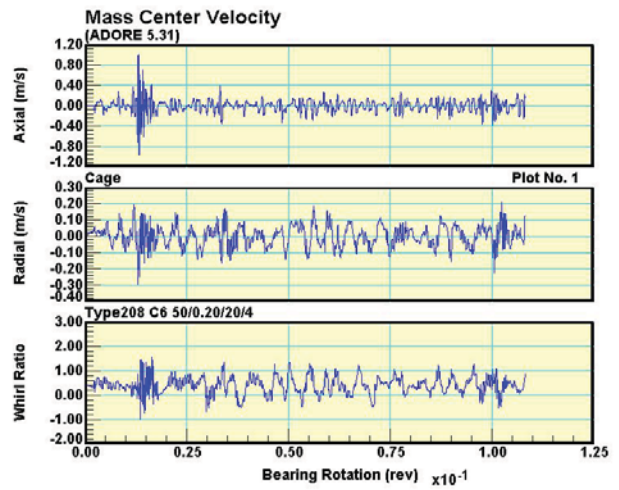
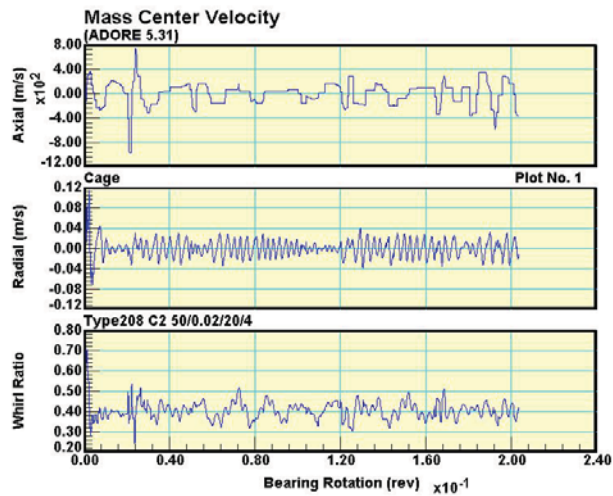


44

# Ball/Race Interaction

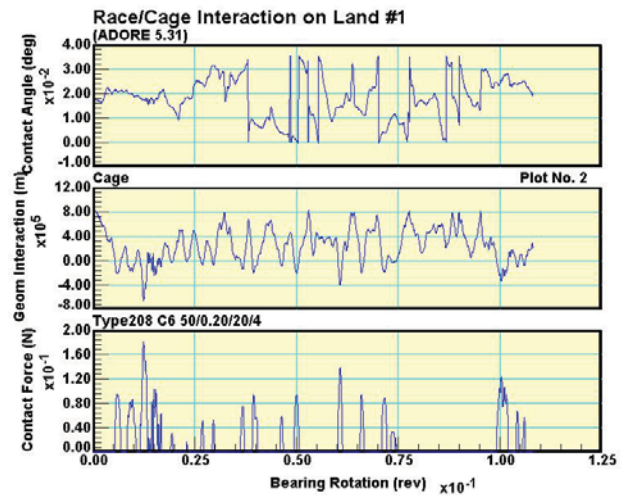
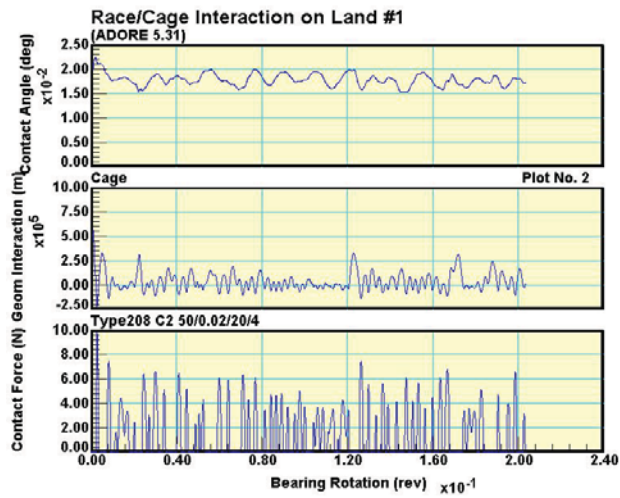


# Cage Mass Center Velocities

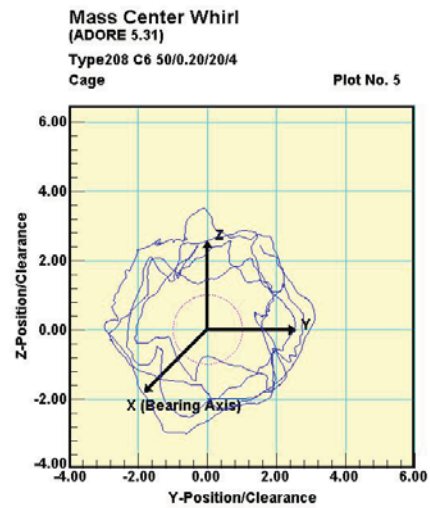
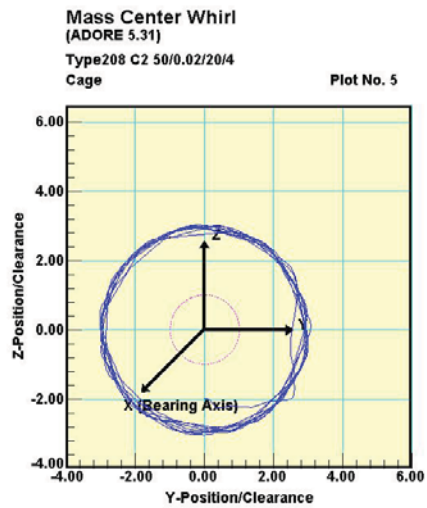




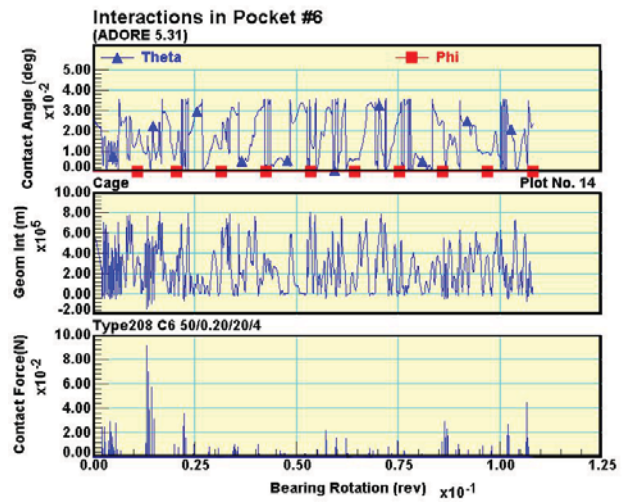
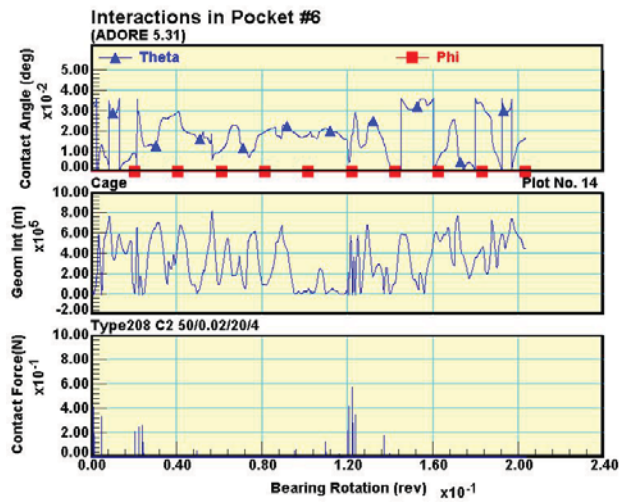
# Cage/Race Interaction



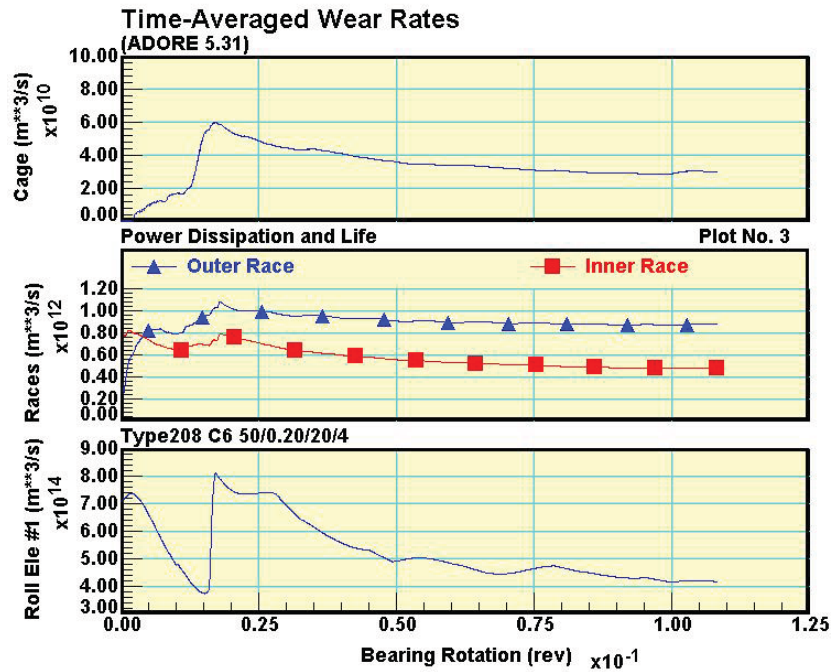
# Cage Whirl Orbits



# Cage Pocket Interaction

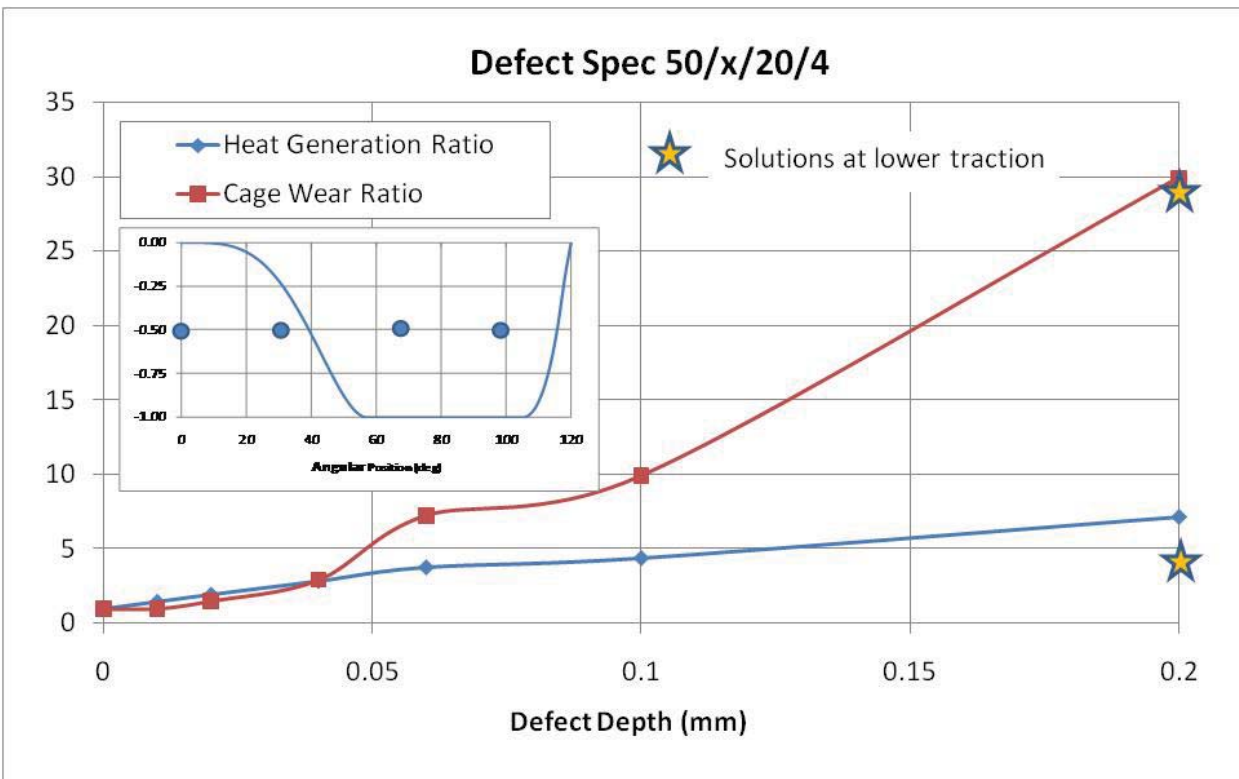


# Time-Averaged Wear Rates



50

# Performance Parameters



51

# Project Outline

- ❖ Objectives
- ❖ Base line tool - ADORE
- ❖ Model Formulation
- ❖ Modeling Approach
- ❖ Customized subprogram for ADORE
- ❖ Bearing Performance Simulations
- ❖ Summary

# Summary

## Performance Parameters at 0.10 mm Defect Depth

Defect Type	Heat Generation Ratio	Cage Wear Ratio
10mm Parabolic	9.67	55.94
20mm Parabolic	3.28	7.55
20mm Elongated Parabolic	4.39	15.93
30mm Parabolic	4.31	8.43
50mm Elongated Parabolic	7.08	30.39
50mm Elongated Higher Order Polynomial	4.40	9.95

# Summary

- High cage interactions and heat generation with small defects width
- Some improvement in performance parameters as defect widens
- Performance deteriorates again with increasing width
- Lower traction reduces heat generation but smaller effect on cage interactions



# Recommendations

- Correlation of defect model to experimentally measured defects
- More elaborate parametric evaluation of bearing performance with measured defects
- Correlation of bearing performance to defect growth rate
- Model available life from initiation to catastrophic failure

**APPENDIX D**  
**University of Florida Contribution**

**Final Project Report**

**Dec 31, 2008**

**Determination of Ball-Raceway Spall Interaction Forces Using ADORE and Ball-Raceway Stresses using FEA in Hybrid Bearings**

Submitted to

Michele L. Puterbaugh  
UTC Program Manager  
Universal Technology Corporation  
1270 N. Fairfield Road  
Dayton, OH 45432-2600  
Phone (937)426-8530 ext 264  
Fax (937)426-7753

Submitted by

Nagaraj K. Arakere  
Mechanical & Aerospace Engineering  
University of Florida  
Gainesville, FL 32611-6300  
Email: [nagaraj@ufl.edu](mailto:nagaraj@ufl.edu)

## 1.0 INTRODUCTION

Aircraft engine and bearing manufacturers have been aggressively pursuing advanced materials technology systems solutions to meet main shaft-bearing needs of advanced military engines. Such efforts are aligned with goals for affordable high speed, high life bearings that have superior durability and corrosion resistance. These requirements have led to the development of hybrid bearings with silicon nitride balls and metal raceways made of materials such as case hardened Pyrowear 675 (P675) / M50NiL and through hardened M50. The rolling contact fatigue (RCF) performance of hybrid ceramic/steel bearings has been shown to be much superior to steel bearings (1-5).

Past bearing material programs typically used life as the primary measure of performance i.e., the time until initiation of the failure. However, there is also a desire to understand what happens after initiation, i.e., the period of time where the bearing is liberating small pieces of material known as spalls. It is this window where bearing issues in the field are detected, usually from the spalled material collected on the magnetic chip detector. The objective of this research project, at the University of Florida (UF), are to model the elastic-plastic stress field associated with loaded region undergoing spall propagation using 3D FEA and gain an mechanistic understanding of the damage evolution due to RCF in the spall region. Parallel research efforts at AFRL, Dayton, OH and UES, Inc., Dayton, OH, have shown that M50 and M50 NiL not only have longer life than 52100 but also have slower propagation rate (6). Examination of the microstructure of the steel is being performed to gain insight into the effects of alloy content, heat treatment, and applied stress field and their effects on the microstructure and ultimately the life and propagation rate. We believe this three-way collaborative research effort at AFRL, UES, Inc. and UF is the first attempt at a systematic investigation of spall propagation and may provide engineers guidance to decrease the spall propagation rate, improving the safety of bearings in the field.

## 2.0 PROGRESS TO DATE

The following critical elements constituting the 3D elastic-plastic FEA has been implemented and tested.

- a) Solid models that accurately represent the 3D geometry of the ball-raceway contact has been built and Hertzian elliptical contact patch size resulting from a combination of radial and thrust loads verified by 3D elastic FEA. Extensive mesh size refinement studies have also been performed to ensure computed subsurface stress field values are accurate.
- b) Three-dimensional elastic-plastic FEA has been implemented and tested for static monotonic loading of a ball on a bearing raceway with and without a spall. Linear isotropic hardening was used in these models that included the plastic regime of the material's stress-strain curve. This is valid since isotropic, kinematic, and combined isotropic and kinematic hardening laws all converge to the same stress solution for static monotonic loading.
- c) Cyclic elastic-plastic FEA in 3D has also been implemented for specific test cases with isotropic, kinematic, and combined isotropic and kinematic hardening laws. This will be utilized for simulating repeated rolling of the ball over the spall. The cyclic stress-strain properties and strain rate effects for bearing materials are difficult to obtain and these models have been run with assumed material properties.
- d) The dynamic impact problem of the ball with the spall edge has been modeled using ABAQUS Explicit module. This allows study of the evolution of elastic-plastic stress fields in the spall edge region and the residual stress development as a function of time. This is a very important aspect of understanding spall propagation.

### 3.0 SPALL PROPAGATION CHARACTERISTICS

The test bearing is a split-inner ring 40mm hybrid with M50 NiL raceways and half-inch diameter silicon nitride balls. Figure 1a shows the as-initiated spall on the inner ring raceway. The peak Hertz raceway stress during testing is 2.41 GPa (350 ksi). Figure 1 shows an initiated fatigue spall and its progressive propagation under RCF in a M50 ball bearing raceway. Figure 1b shows the typical progression of spall under continued RCF. The spall first widens almost across the entire width of the raceway. The depth of the spall is roughly 125  $\mu\text{m}$  (0.005 inch). Once the spall spans the axial width of the raceway propagation is seen to proceed in the direction away from the initial spall leading edge, in the circumferential direction. Figure 2 summarizes aspects of the complex interplay between maximum Hertz stress, material selection and spall propagation rate, as measured by bearing mass loss (6). Tests were conducted at the same temperature for both 52100 and M50 NiL materials. We note that 52100 steel shows rapid spall propagation at 278-ksi max Hertz stress. Even at 250-ksi-peak Hertz stress the propagation rate is significant and if increased to 278 ksi during operation the rate increases very quickly. In contrast, M50 NiL will not propagate a spall at 300-ksi peak Hertz stress. If the stress level is increased to 350 ksi the increase in spall propagate rate is more gradual than for 52100 material. It should be noted that the cleanliness of these two bearing steels are similar as is the hardness levels. Clearly there are interactions between stress level and as yet unknown material parameters that affect spall propagation rate, that are not understood. Figure 3a shows a schematic of spall on the inner raceway along with bearing kinematics details. For an inner ring speed of 10,000 RPM, cage RPM is 4,023 and ball RPM is 22,814. Inner raceway speed relative to the ball is 15.18 m/sec (49.8 ft/sec). Based on testing, modeling and metallurgical investigation (6, 7) we propose the three-step process outlined below to explain the progressive damage caused by spall propagation:

1. Material on the edges of the spall yields due to RCF. The yield stresses induced by the ball rolling on the spall are higher on the diametral edges of the spall along the shaft axis than at the spall leading and trailing edges. This scenario will be or was substantiated with 3D FEA modeling of the stresses in the neighborhood of the spall due to rolling and via hardness measurements near the spall [7]. Material degradation from repeated rolling causes the spall to widen as shown in Figure 1b. The spall width eventually spans the width of the raceway, as seen in Figure 1.
2. Widening of the spall allows for the ball to descend into the spall. Since the spall depth (125  $\mu\text{m}$ , 0.005 in) is greater than the bearing radial internal clearance the ball will unload, illustrated in Figure 3b. The load supported by this ball is then shared by other loaded balls in the bearing, leading to a change in the effective bearing stiffness.
3. As the ball moves through the spall length, pushed along by cage interaction forces, it will partially impact the spall trailing edge as it climbs onto the intact raceway (Figure 3b). The stresses arising from the impact along with the contact stresses results in severe fatigue of the spall trailing edge material, leading to propagation of the spall in the direction indicated in Figure 1 and Figure 3a. Estimation of impact stresses at the trailing edge will be explained in a later section.

### 4.0 MODELING RESULTS

Modeling results from the 3D linear elastic FEA, elastic-plastic FEA and time transient analysis of the ball impact with the spall edge are presented now.

#### 4.1 Three-Dimensional Finite Element Modeling of Stress Field in the Spall Neighborhood

A 3D finite element (FE) model was built using ABAQUS 6.7 to model the stress state as a silicon nitride ball goes over a circular raceway spall in a bearing application. The FE model is an accurate representation of the full 3D ball-inner raceway contact geometry, as shown in figures 4 and 6. The test bearing material and geometric properties are shown in Table 1. Mesh refinement tests were performed for both tetrahedral and hexahedral elements such that converged results for Hertz peak elliptical contact stress agreed to within 1% of the analytical solution. Tetrahedral linear elements were used because of their ability to easily mesh complex geometries, such as the edge of a spall. The severe stress concentrations imposed by the elliptical contact and spall geometry required a very refined contact mesh geometry for obtaining acceptable solutions. Also, the use of linear tetrahedral elements proved to be more efficient than quadratic elements, based on achieving a balance between solution accuracy and run time.

E= Elastic modulus, $\nu$ = Poisson's ratio	
Steel raceway	E = 200 GPa, $\nu$ = 0.3
Silicon nitride	E = 310 GPa, $\nu$ = 0.3
Raceway yield stress, $Y$ = 2.34 GPa	
Silicon nitride ball diameter	12.7 mm
Inner raceway curvature, $f_i$	0.52
Inner ring bore	40 mm
Bearing pitch diameter	60.24 mm
Inner raceway radius	23.77 mm

Table 1 Test bearing material and geometric properties

Half symmetry modeling was used since the contact patch load and the bearing geometry was symmetric. Quarter symmetry was used for the unique case when the ball is directly over the center of the spall. Figure 6 illustrates this. The stress concentration created by the spall edge radius was found to greatly influence the severity of the stress state, as illustrated in Figure 7. The spall edge radius was chosen to be 1 mm, based on meshing and convergence considerations. The depth of the spall was chosen to be 125  $\mu\text{m}$  (0.005 inch), based on experimental measurements. The spall diameter is used as a parameter in the analysis. The normal load applied to the ball to achieve a peak Hertz contact stress of 2.65 Mpa (385 ksi) on the inner raceway is 1630 N (366 lbs).

Finite element simulation of the loaded ball, with a peak Hertz contact stress of 2.65 Mpa (385 ksi) away from the spall, rolling over the spall is accomplished via a series of single static load cases. Spall diameter is treated as a variable. Dynamic loading effects such as yield strength dependency on applied strain rate are not included. Also, initial residual stresses from case or work hardening were not included. These aspects as well as unloading effects are not studied here but will be considered in forthcoming studies.

Linear elastic analysis of the stress field in the neighborhood of the spall, caused by ball rolling, indicated that stresses everywhere on the edge of the spall exceeded the ultimate tensile strength. This is not surprising since both nonconformal contact loading and the spall surface geometry represent severe stress concentrations. For a more realistic stress field computation we used elastic-plastic FEA. The use of the associated flow rule to calculate increments of plastic deformation, as implemented in ABAQUS, was utilized for modeling elastic-plastic behavior. Linear isotropic hardening was used in the models that included the plastic regime of the material's stress-strain curve, shown in Figure 5. This is valid since isotropic, kinematic, and combined isotropic and kinematic hardening laws all converge to the same stress solution for static monotonic loading. It is during unloading and subsequent load cycles that these laws begin to display different behavior.

## 4.2 Finite Element Analysis Results

Figure 4a shows a schematic of the ball elliptical contact patch moving over the circular spall. Figure 8 depicts the maximum subsurface von Mises stress in the neighborhood of the spall edge as a ball rolls over a 3 mm diameter circular spall, as indicated in Figure 4a. The peak Hertz contact stress away from the spall is 2.65 Mpa (385 ksi), as indicated earlier. Results are shown for three different positions of the ball over the spall: at the leading edge, between the edge and the center, and directly over the center. The blue line represents the static yield strength limit, while the red line represents the static ultimate strength limit. [The elastic stresses exceed the yield and even the ultimate strength for all positions of ball with respect to the spall.] The von Mises stresses are highest when the ball is in the center of the spall and the lowest when it is at the edge. It is important to note that the magnitude of von Mises stress is highest on the axial diametral locations, indicating that the spall widens due to RCF in the axial direction spanning the width of the raceway, as shown in Figure 1b, before propagating along the raceway in the circumferential direction, as shown in figures 1c and 1d. On reflection, this is intuitive since there is less material supporting the ball when it is in the center of the spall than when it is on the spall's edge. Figure 9 displays cross sections of the von Mises stress contours for the three “ball-over-spall” positions. Figure 10 shows the effect of increase in peak Hertz stress on spall edge stresses, for on center loading. It also shows the volume of yielded material around the spall increases with increasing operating load. This also helps to confirm that the material removal rate is higher for increasing operating loads since the damage accumulation is faster due to the higher stresses within the spall. We note that the peak plastic stress has exceeded the ultimate tensile strength. This is a consequence of the linear extrapolation used in the stress-strain curve with a constant plastic modulus, as shown in Figure 5. A suitable nonlinear fit for the stress-strain curve will resolve this concern. Figure 11 shows a close up of the von Mises stress contours at the edge of a spall. The high stress gradients indicate that they are potential sites for damage initiation. Figure 12 demonstrates that the maximum von Mises stress experienced in the spall edge region increases with spall diameter, for both elastic and plastic analyses.

## 4.3 Estimation of Impact Stress at the Spall Trailing Edge

We proposed in the spall propagation characteristics section that the spall widens first in the axial direction (Figure 1b), spanning the width of the raceway and, eventually, allowing the ball to descend into the spall causing the ball to unload (Figure 3b). This unloaded ball is moving at 15.2 m/s relative to the inner raceway. We hypothesize that as it approaches the trailing edge, the lower portion of the ball will impact or partially impact the oblique edge. Once the ball climbs onto the raceway it is loaded, and will establish the Hertz contact stress, as computed in the FE model. Hence the trailing edge inside the spall is likely to experience stress from the ball impact loading while the trailing edge surface on the raceway will experience the Hertz contact stress. We propose that repeated application of this combined loading due to RCF weakens the inside spall edge material leading to spall propagation along the raceway circumference, as shown in Figs. 1d and 3a. A detailed analysis of a silicon nitride ball impacting an oblique surface, accounting for the proper raceway and cage constraints, is expectedly very complicated. We perform a simplified impact analysis of a rigid 12.7 mm (0.5 inch) diameter ball with a density of 2,600 kg/m<sup>3</sup> for silicon nitride, striking a ductile metallic oblique surface at a 45-degree angle to horizontal, based on Johnson (8), Tabor (9), Crook (10), Rickerby and McMillan (11) and Hutchings et al. (12), using the equation shown below.

$$p_o = \frac{3}{2\pi} \left( \frac{4E^*}{3R^{3/4}} \right)^{4/5} \left( \frac{5}{4} mV^2 \right)^{1/5} \quad (1)$$

For an impact velocity of  $V=15.2$  m/s (50 ft/sec), the estimated peak contact stress,  $p_o$ , at the spall trailing edge during impact is  $\sim 5.2$  GPa (750 ksi), using Eq. (1). Subsurface yielding is predicted if the maximum contact pressure reaches  $1.6*Y$  where  $Y$  is the material yield stress (8). Using a yield stress of 2.34 GPa (340 ksi), and accounting for increased value for dynamic yield stress (9, 10), we can predict yielding at the spall trailing edge for a peak contact pressure above 4.9 GPa (710 ksi). For a more thorough impact analysis the ball-spall-cage interaction forces have to be taken into account coupled with a 3D FE stress analysis. Although our impact analysis is simplified, it is based on past experimental work and is likely conservative. Thus the combined effects of repeated applications of impact and contact stress at the spall trailing edge is thought to initiate material degradation and eventually spall propagation along the raceway, as shown in Figure 1.

The above impact problem was also simulated using ABAQUS Explicit via a dynamic analysis of a ball striking the edge of a spall as seen in Figure 13. For this case the ball was assumed to be analytically rigid and the influence of the curvature of the raceway in the circumferential direction was assumed to be negligible. The same material properties used in the static analysis were also used here since strain rate dependent material properties are not yet readily available for these bearing steels. The geometry of the spall is the same as in the static analyses. Figure 13b shows a close-up view of the spall edge with the plastically deformed subsurface region shown in red, resulting from the impact. The time transient subsurface stress evolution during ball impact to spall edge is captured using an explicit dynamic simulation. The explicit approach necessitates a very small time step of  $7.88 \times 10^{-10}$  sec for numerical stability. Based on the ball velocity of 15.2 m/s (50 ft/sec), the total simulation time elapsed during impact is  $3.5 \times 10^{-5}$  sec, requiring a total of 44,416 explicit time step increments to simulate a single impact of ball with spall edge.

Figure 14 shows the evolution of contact pressure, maximum von Mises stress and maximum principal stress during impact. The important conclusion from Figure 14 is that yielding occurs within the edge of the spall during impact. This agrees with the simplified analytical solution discussed before. The maximum contact pressure also reaches a high value of 7.8 GPa during contact.

The residual stress states in the radial and hoop direction, after unloading of the ball, are of practical interest for spall propagation analysis. After the ball has impacted the spall, residual stresses were observed to develop. Residual stress states are of great importance regarding fatigue life calculations. Actual subsurface residual stress states in spalled bearings obtained by X ray diffraction techniques were compared to those found by FEA methods. Figure 15 shows the residual stress state in the hoop direction calculated by ABAQUS. Locations of depth profile data are shown by the black lines. The corresponding raw data is also shown in the stress versus depth charts shown in Figure 16. The corresponding raw data is also shown in the stress versus depth charts in Figure 16. The shapes of the experimental and finite element curves are similar but not exact. Finite element results predict subsurface tensile stresses in locations that are not seen in the experimental values. The actual values of graph number (3) Figure 16 are the most similar to those found by X ray diffraction (7). Large tensile stresses are calculated at the surface for some of the finite element computations whereas compressive stresses are seen at the surface for the X ray diffraction results.

These discrepancies are explained by the fact that the finite element model only experienced one impact, whereas the spall in the actual bearing used in X ray diffraction experienced thousands of impacts. The cumulative fatigue damage from successive impacts can result in stress fields that are markedly different from a single impact. These effects will be studied in subsequent analyses. Friction was also neglected in the model but is believed to play an important role since the layer of elastohydrodynamic lubrication is thought to degrade at the spall's edge during impact. Other effects such as localized heating and deformation of the ball were also neglected but could play a significant role.



The residual stress state in the radial direction after one impact is shown in Figure 17. This is a significant plot because there has yet to be any experimental data that shows the radial residual stresses around a spall. The zone of tensile stresses where the edge meets the bottom of the spall is noteworthy because this could be a critical site of fatigue crack initiation. The blue compressive region beneath the spall is thought to keep all of the damage propagation localized to the surface, as seen in the damaged raceways.

## 5.0 CHARACTERIZATION OF MATERIAL PROPERTIES FOR M50 AND CASE HARDENED P675 BEARING STEELS VIA STATIC AND DYNAMIC INDENTATION

One of the major difficulties in spall propagation modeling is that relevant in-situ static and cyclic material properties are not available for both through hardened M-50 and case hardened P675 bearing steels. Bearings operating at high RPM undergo high strain rate loadings, dictating the use of dynamic material properties such as dynamic hardness and fracture toughness. By comparing such data to static material properties, an indication of the rate sensitivity of a material can be determined. We have conducted a systematic static and dynamic indentation of bearing steels to capture the stress-strain properties as a function of depth, via micro indentation (13-15).

### 5.1 Comparison of Static and Dynamic Indentation

Utilizing the supplied sample rod of the M50 tool steel (9.525 mm diameter), an initial reference value of the Vickers indentation hardness was obtained on the cross section. These values are included in Table 1 below. It should be noted that the hardness values of the sample rod were lower than expected, compared to hardness data for the M50 raceway, possibly resulting from differing heat treatment conditions.

**Table 1:** Static Vickers hardness of M50 rod (average from 5 tests).

Load (15 sec)	300 g	1000 g
Hv (kg/mm <sup>2</sup> )	712	702

Utilizing the DIHT, dynamic hardness data from indentation loads ranging from 1 kg to 350 kg was extracted from both the P675 and M50 raceway specimens. Additionally, static Vickers indentation testing was conducted on both raceway materials. By comparing static and dynamic indentations, an indication of the rate dependence of hardness in a raceway begins to develop. Figure 18 shows both static indentations (shown as circles, taken as an average of five indentations at each load, with loading durations of 15 seconds) and dynamic indentations (shown as boxes, one per indent, with loading durations of 100  $\mu$ s) on the undeformed P675 raceway surface. Note that the maximum available load in the commercial static indentation tester is limited to 50 kg.

For static indentations, an indentation size effect<sup>2</sup> (ISE) appears at lower loads. Additionally, the lowest load indentations have a larger variation due to the influence of the raceway surface roughness (surface roughness is discussed in a later section). There is also an indication of a small hardening effect for the high rate dynamic indentations; however, this effect is absent at larger loads. The observed decrease in hardness at high load is likely due to the increasing depth of indentation resulting in deeper indents which interact with the ductile core layer of the P675 raceway.

Similarly, a comparison between static and dynamic indentation hardness values was made for the M50 raceway material. Figure 19 shows both static indentations (again shown as circles, taken as an average of five indentations at each load, with loading durations of 15 seconds) and dynamic indentations (again shown as boxes, one per indent, with loading durations of 100  $\mu$ s) on the undeformed raceway surface. Similar to the P675, there is an observed ISE for the low load static indentations.

## 5.2 Deformed vs. Undeformed Raceway

A comparison between the undeformed and deformed (ball path) regions of the raceway material was also produced utilizing static indentations. This data is summarized in Table 2 below.

**Table 2:** Deformed/undeformed raceway static hardness at 1 kg load.  
Each value is an average of 5 indents.

	<b>M50</b>	<b>P675</b>
<b>Outside of Wear Track</b>	780 Hv (~ RHC 63)	846 Hv (~ RHC 66)
<b>Deformed Region (within wear track)</b>	722 Hv (~ RHC 61)	830 Hv (~ RHC 65)

From this data, a number of conclusions can be drawn. Most interesting is that the plastic deformation produced during rolling contact and shakedown results in only a slight reduction in hardness for both P675 and M50. This small change is likely due to the already high hardness produced through heat treatment, which does not allow much room for further hardening due to plastic deformation. The following section covering compression testing further details this result.

## 5.3 Compression tests

A small number of static and dynamic compression tests were conducted on specimens sectioned from the supplied M50 rod. Compression tests were not performed on the P675 rod, as the case hardened nature (changing hardness with cross section location) would only produce an average yield stress value, which cannot be compared to indentations taken on specific regions of the samples. Figure 20 shows compression data from a static test conducted on a cylindrical specimen of the M50 material revealing a nearly perfectly-plastic response with a yield point near 2.4 GPa. Note that the strain values are incorrect due to a machine error resulting from the test frame lacking the necessary rigidity. Nevertheless, this curve confirms the previous results on the plastically deformed ball path, where the M50 showed very little hardening behavior and little change in hardness values beneath deformed and undeformed regions.

In an effort to reproduce the service condition of the plastically deformed ball path, a number of specimens of the M50 were compressed dynamically using a split Hopkinson pressure bar (SHPB). Samples were compressed to varying degrees of deformation, including a maximum of 16%. Deformation beyond 16% resulted in fracture of the test specimens. After the test, the specimens were polished and indented in an effort to characterize the hardening behavior under dynamic compression. Figure 21 shows compression specimens with a polished and indented surface.

These M50 rods showed little to no hardening behavior under dynamic compression. Data summarizing static (average of 5 indents) and dynamic indents on a deformed specimen is shown in Table 3. Additionally, the prior deformation of the specimen had no influence on the nature of deformation surrounding indents, as they remained ductile in appearance.

**Table 3:** Hardness of pre-deformed M50 specimen, 15.8% deformation.

<b>Static (15 sec) 1 kg</b>	<b>700 Hv</b>
<b>61.5 kg, Dynamic</b>	<b>725 DHv</b>
<b>68.1 kg, Dynamic</b>	<b>737 v</b>

## 5.4 Fracture Toughness

As mentioned above, indentations on the M50 material (both rod and raceway specimens) remained ductile in appearance regardless of the extent of previous deformation. Therefore, the study of indentation fracture was limited to the case-hardened P675 raceway specimens. During the previous indentation work, it was found that the load range required to initiate brittle behavior in the raceway material was extremely high, as loads beyond 300 kg were required to initiate cracks. This required load is well beyond the range of the commercial static Vickers hardness machine; therefore, the current study has utilized dynamic indentation as a means to estimate the fracture toughness of the P675 by inducing cracks at high loads.

Indentations were performed on both the virgin P675 raceway surface as well as within the deformed ball track. Figure 22 shows the indentation imprint on the virgin raceway surface where cracks are beginning to emerge at the corners of the indent. This established the minimum load required for crack initiation.

Indentations were also produced within the deformed region of the ball path. Figure 23 shows two indents in this region which resulted in significant crack propagation. Interestingly, cracks initiate parallel to the ball track while no cracks are seen perpendicular to the ball track. It was concluded that this result is influenced by two factors. First, due to a residual compressive hoop stress in the bearing raceway. This would serve to prohibit crack opening perpendicular to the rolling direction. Second, the surface finish (texture) resulting from the manufacture and machining of the raceway has likely produced crack initiation sites. As seen in the micrographs, the surface roughness appears as grinding marks parallel to the rolling direction, resulting in cracks which more readily propagate along these grooves. Analysis of additional indents pointed to the second option, as it was not uncommon for cracks to appear perpendicular to the hoop direction, while it was always evident that the surface finish influenced crack initiation.

Note that some cracks appear to have started slightly away from the corner of the indent. It is believed that these cracks have emerged at much lower depths (when the applied load was still increasing) during the indentation from the corners of the indent and have continued to grow with increasing depth. Hence, the crack path may have deviated slightly from the exact corner upon reaching the final depth (load).

Out of 50 total high load dynamic indentations on P675, crack propagation was evident in only 16 of the tests. This is partially due to the high loads required for cracks to initiate. Cracks were most commonly found when

loads were in the range of 3000 N to 3500 N. Crack appearance showed minimal differences between the deformed and undeformed regions of the raceway.

From the tests which produced cracks, some indents showed cracks at only one corner or at two neighboring corners (i.e., cracks were perpendicular). These cracks were not used for fracture toughness calculations. Similar to the method for determining indentation fracture toughness of ceramics<sup>3</sup>, indents with cracks on opposite corners were analyzed in an effort to determine a dynamic Vickers indentation fracture toughness value. Figure 24 shows a typical indent produced at high loads, resulting in brittle behavior at opposing indentation corners.

For the current crack system, it was determined that the cracks are of Palmqvist<sup>4</sup> type (see schematic in Figure 25), resulting from the combined response of the hard case layer and the ductile core. In this configuration, it is unlikely that deep radial/median crack systems will form beneath the indent due to the greater ductility of the core material. Instead, shallow surface cracks form in the more brittle case material. Additionally, the indentations which show crack propagation from only one corner (instead of opposite corners as seen in Figure 22) indicate that cracks appearing at opposite sides of an indentation are independent.

From the above observations, a preliminary calculation of fracture toughness was made. This required the use of Vickers indentation fracture toughness equations originally proposed for use on brittle materials (i.e., ceramics) exhibiting Palmqvist type crack behavior (16). Numerous such equations are available. We have used the following equation which is applicable for hard metal carbides such as tungsten carbide and has also been used for borided steels. The relevant equations are listed below (16).

$$K_c = 0.0193(H_v a)(E / H_v)^{2/5} (l^{-1/2}) \quad \text{for } l/a \approx 0.25 \text{ to } \approx 2.5$$

$$K_c = 0.0264(H_v a)(E / H_v)^{2/5} (l^{-1/2}) \quad \text{for } 1 \leq l/a \leq 2.5$$

Where,  $K_c$  is fracture toughness,  $E$  is Young's modulus,  $H_v$  is Vickers hardness,  $P$  is load,  $l$  is half crack length (see Figure 25),  $a$  is half diagonal length and  $c=l+a$ . Note that the constants used are different depending on the crack length. In our investigation, the dynamic Vickers indentation fracture toughness values fall in the range of 12 to 21 MPa/m (from three tests), depending on the equation and parameters used. While this range is fairly broad, these calculations still require further refinement to include the effect of the case/core hardness vs. depth profile, residual stresses remaining from manufacturing, and effects of surface roughness. Although some variation in the data exists, the average indentation fracture toughness value tends to be around 15 MPa/m for this limited data.

## 5.5 Polished Raceway

Furthermore, the appearance of the as-received bearing surface is a cause for consideration. The texture resulting from the grinding marks produced during the manufacturing processes are possible sources for crack initiation. In an effort to determine the influence of surface finish, one sample of the virgin raceway was lightly polished to remove these marks. Indentations were made on this surface to determine the load level where cracking initiates. One such example is shown in Figure 22, where the load required to produce cracking was in excess of 3.2 kN. This high load required for crack initiation may be the result of the removal (by polishing) of crack initiation sites (i.e., grinding marks), indicating that the surface finish has an influence on the indentation

fracture behavior. It was not quantified, however, if the amount of material removed during polishing influenced the case layer hardness, thus increasing the load required for crack initiation.

## **5.6 Monolithic Samples**

While polishing the raceway surface to remove machining marks was attempted, it was possible that this procedure was detrimental to the case layer hardness, resulting in hardness data which was not comparable to previous indents. In an effort to minimize this influence, samples produced from thin sections (0.1 inch, created by Metcut) were utilized. Additionally, the thin P675 samples were produced in a manner which resulted in a nearly constant hardness (comparable to the case layer hardness) through the entire thickness. This was beneficial in two regards. First, the samples could be polished without concern for removing or altering the case layer hardness, resulting in an accurate extraction of the case layer properties. Second, as no core layer was present, a simplified analysis of the indentation fracture toughness is possible.

In order to confirm the existence of a monolithic case layer, indentations on the cross section of the thin specimen were performed. Figure 26 contains a plot of this data for the P675 sample, showing only a minimal decrease in hardness when approaching the center of the cross section.

From a total of 12 static indentations resulting in cracking, the indentation fracture toughness was estimated using the equations shown in section 5.4. The calculation resulted in an average fracture toughness value of  $25.9 \pm 2.8$  MPa $\sqrt{\text{m}}$ . When compared to the raceway indentation fracture value, the higher toughness and lower data scatter is likely due to the polished surface finish and consistent material properties throughout the specimen. This result emphasizes the extent to which surface finish influences the indentation behavior of a material.

Noting that very few studies on the indentation fracture toughness of tool steels have been conducted, this simplified approach utilizing the “monolithic case layer” P675 sample allows for a better understanding of the fundamental mechanisms influencing the indentation fracture behavior of the raceway. This also illustrates the complexities involved with obtaining a value for indentation fracture toughness for the raceway specimens.

## **5.7 Sub-Surface Hardness Profiles**

In order to better understand the mechanisms influencing the indentation behavior of the M50 and P675 raceway samples, an effort was made to characterize the sub-surface deformation resulting from large dynamic indents. Specimens cut from the raceway were first indented at high loads (yet low enough as to not induce cracks) using the dynamic indentation hardness tester. The specimens were then progressively ground and polished to reveal the subsurface directly beneath the indent. Small polishing steps were used in order to keep polishing induced damage to a minimum. Figure 27 shows an indentation field beneath a surface indent on the P675 raceway. The large surface indent was produced at a load of 81 kg (dynamic), resulting in an indent diagonal dimension of 425  $\mu\text{m}$  and a depth near 75  $\mu\text{m}$ . The subsurface micro-indentations were produced using a static 200 gram load and were spaced 100  $\mu\text{m}$  to avoid interactions. It should be noted that all indentations begin 100  $\mu\text{m}$  beneath the sample surface to avoid edge effects.

From the data produced by the subsurface indentation fields, contour plots which map the indentation iso-hardness lines were produced for indents on both P675 and M50. Such plots are shown in Figures 28 and 29 for P675 and M50, respectively. This data, when compared to the hardness vs. depth profiles for the virgin raceway specimens, gives an indication of the hardening effects produced by the surface indent (Figure 30).

By simultaneously plotting the subsurface hardness values for the virgin material, and at locations directly beneath the indenter tip and 400  $\mu\text{m}$  from the indenter tip, a better representation of the hardening effect is shown in Figure

31 (see inset schematic for illustration of location in Figure 31). From this plot it is evident that the extent of plastic deformation induced by the large surface indent has reached a depth of 800  $\mu\text{m}$  (i.e., hardness value beneath the tip matches virgin hardness at same depth).

The above data can be used in finite element models to characterize the deformation and hardening behavior of these materials as a function of depth. In the future it is anticipated that such models be developed and extended to include the initiation of indentation cracking, resulting in a better analysis of the fracture behavior of the raceway.

## **6.0 CONCLUSIONS BASED ON WORK TO DATE**

Based on results from 3D FE stress analysis in the spall neighborhood, simplified trailing edge impact stress analysis, dynamic finite element impact analysis of the ball with the spall edge using ABAQUS Explicit, and spall propagation tests (6, 7), we come to the following conclusions:

1. Elastic and elastic-plastic 3D FEA of the stress field in the neighborhood of a circular spall shows that there is extensive yielding at the spall edges due to ball rolling contact. The stress magnitudes are highest at the axial diametral locations of the spall.
2. We hypothesize that the spall first widens in the axial direction, spanning the width of the inner raceway (Figure 1b). This allows the ball to descend into the spall causing it to unload (Figure 3b).
3. The unloaded ball then catches up to the spall trailing edge, resulting in a impact with the oblique edge. The impact stress, estimated via simplified analysis, was shown to be adequate to cause yielding of the trailing edge. A time transient finite element analysis of the ball impact with spall edge is also performed using ABAQUS Explicit and the evolution of spall edge stresses captured during impact, which also shows extensive yielding of the spall edge as a result of the impact.
4. The combined effects of repeated impact and contact stress at the spall trailing edge results in material degradation, resulting in propagation of the trailing edge in the circumferential direction (Figure 1).
5. In-situ fracture toughness and hardness profiles are provided for M-50 and P675 case hardened materials, via comprehensive static and dynamic indentation, and by mapping the subsurface region using micro indentation. The fracture toughness values for P675 agree with results produced via fracture specimens made with monolithic case material (Timken results).



## 7.0 REFERENCES

- (1) Miner, J. R., Dell, J., Galbato, A., and Ragen, M. A., (1996), "F-117-PW-100 hybrid bearing ceramic technology insertion," *ASME J of Engineering for Gas Turbines and Power*, V 118, pp. 434-442.
- (2) Tanimoto, K., Kajihara, K., and Yanai, K., (2000), "Hybrid ceramic ball bearings for turbochargers," *SAE Paper* 2000-01-1339, pp. 1-14.
- (3) Wang, L., Snidle, R. W., and Gu, L., (2000), "Rolling contact silicon nitride bearing technology: A review of recent research," *Wear*, Vol. 246, pp. 159-173.
- (4) Hadfield, M., (1998), "Failure of silicon nitride rolling elements with ring crack defects," *Ceramic International*, Vol. 24, pp. 379-386.
- (5) Hadfield, M., Stolarski, T. A., (1995), "The effect of test machine on the failure mode in lubricated rolling contact of silicon nitride," *Tribology International*, Vol. 28, pp. 377-382.
- (6) Rosado, L., Forster, N. (2008), Thomson, K., "On the Rolling Contact Fatigue Life and Spall Propagation Characteristics of M50, M50 NiL and 52100 Bearing Materials: Part I - Experimental Results," to be presented at the STLE Annual Meeting, May 18-22, 2008, Cleveland, OH.
- (7) Forster, N., Massey, M. (2008), "On the Rolling Contact Fatigue Life and Spall Propagation Characteristics of M50, M50 NiL and 52100 Bearing Materials: Part III - Metallurgical Examination," to be presented at the STLE Annual Meeting, May 18-22, 2008, Cleveland, OH.
- (8) Johnson, K.L. (1987), *Contact Mechanics*, Cambridge Press, Cambridge, pp. 361-366.
- (9) Tabor, D. (1948), A simple theory of static and dynamic hardness, *Proceedings of Royal Society*, A192.
- (10) Crook, A. W. (1952), A study of some impacts between metal bodies by a piezoelectric method, *Proceedings of Royal Society*, A212.
- (11) Rickerby, D. G., McMillan, N. H. (1980), On the oblique impact of a rigid sphere against a rigid-plastic solid, *International Journal of Mechanical Sciences*, Vol. 22, pp. 491-494.
- (12) Hutchings, I. M., Rickerby, D. G., McMillan, N. H. (1981), Further studies of the oblique impact of a hard sphere against a ductile solid, *International Journal of Mechanical Sciences*, Vol. 23, pp. 639-646.
- (13) G. Subhash, Dynamic Indentation Testing, *ASM Handbook*, 8, (2000).
- (14) P. M. Sargent, *ASTM Special Technical Publication*, 1985
- (15) A. G. Evans and E. A. Charles, *J. Am. Ceram. Soc.*, 59, (1976).
- (16) S. Palmqvist, *Jernkortorets Ann.*, 141, (1957).
- (17) J. Lankford, *J. Mater. Sci. Lett.*, 1, (1982)
- (18) I. Campos, G. Ramirez, C. VillaVelazquez, U. Figueroa, G. Rodriguez, *Mat. Sci. & Eng. A*, 475 (2008)
- (19) K. Niihara, R. Morena, and D. P. H. Hasselman, *J. Mater. Sci. Lett.*, 1, (1982)
- (20) K. Niihara, *J. Mater. Sci. Lett.*, 2, (1983)

## **FIGURES**

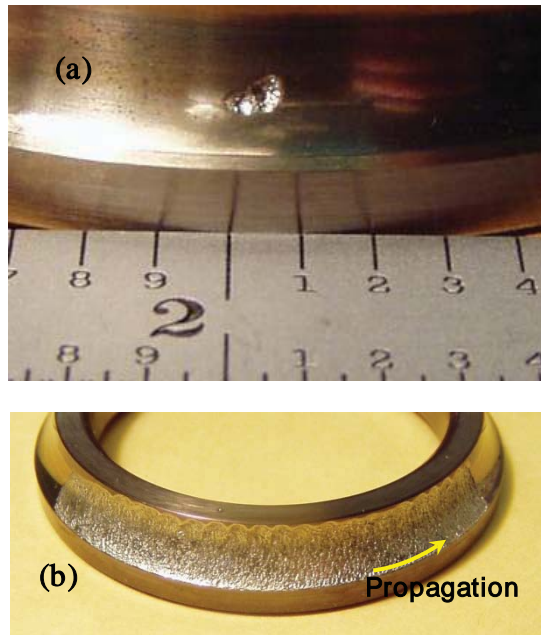


**Figure 1.** (a) Fatigue spall initiation on inner raceway,  
b) progressive propagation of the initiated spall under continued RCF



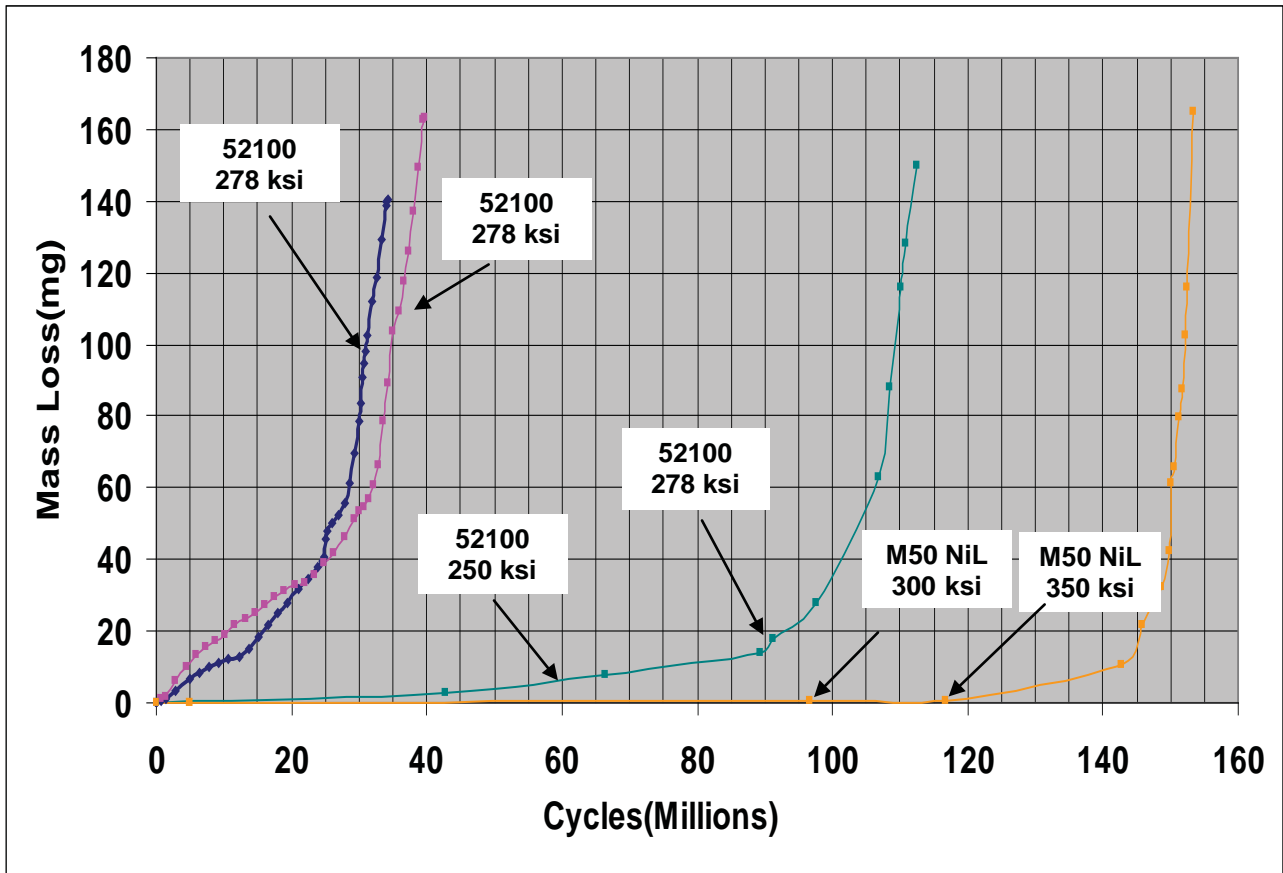


**Figure 2.** Effect of maximum inner raceway Hertz stress (ksi) and material selection on loss of raceway material due to spall propagation (6). Note that M50 NiL will not propagate a spall at 300 ksi while 52100 has a very rapid spall propagation rate at 278 ksi.

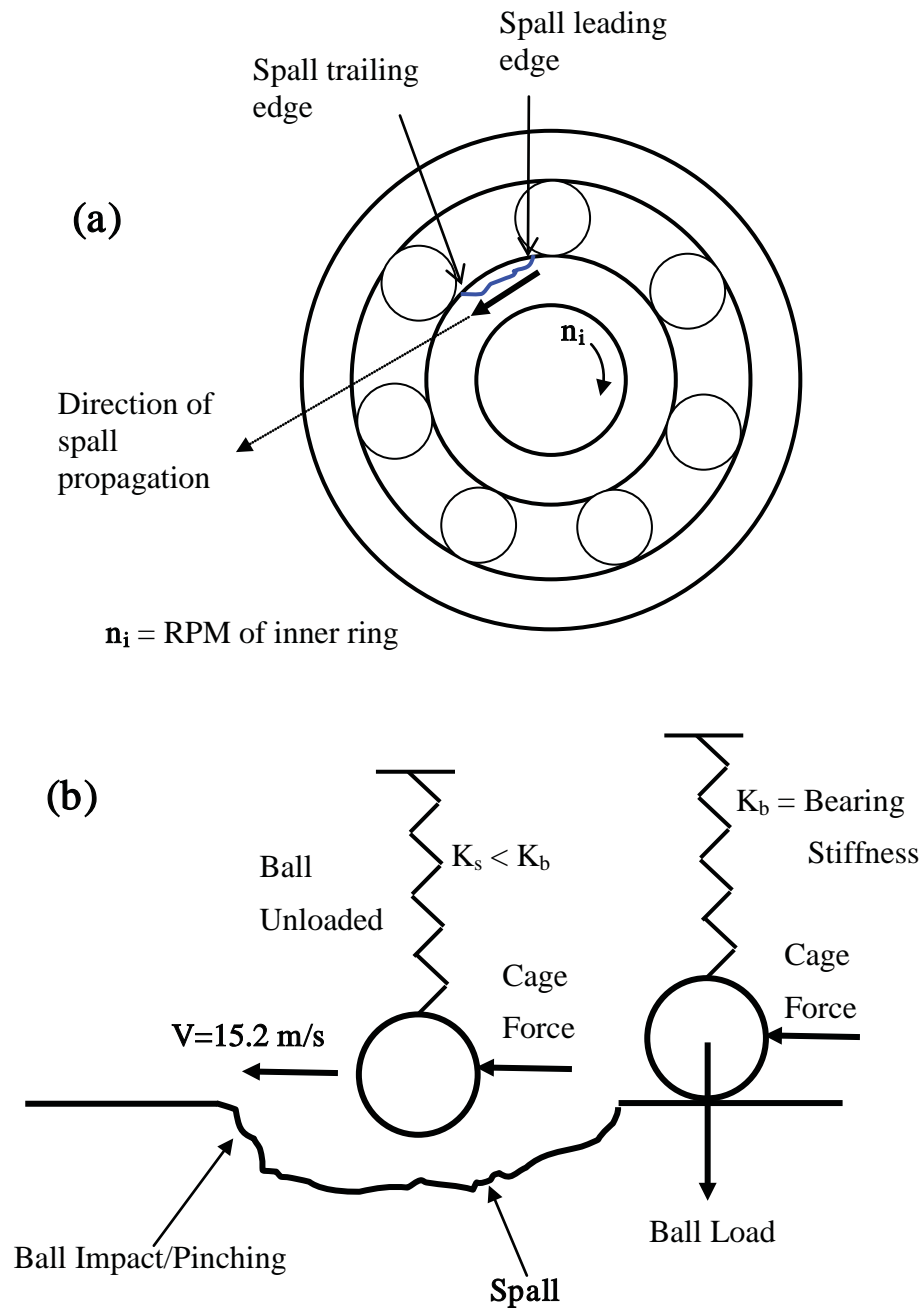


**Figure 3.** (a) Test bearing schematic showing the inner ring spall as a blue line. For  $n_i = 10,000$  RPM, cage RPM is 4,023 and ball RPM is 22,814. Inner raceway speed relative to the ball is 15.18 m/sec (49.8 ft/sec).  
 (b) Schematic explaining the unloading of ball in the spall and subsequent impact resulting in yielding at spall trailing edge.

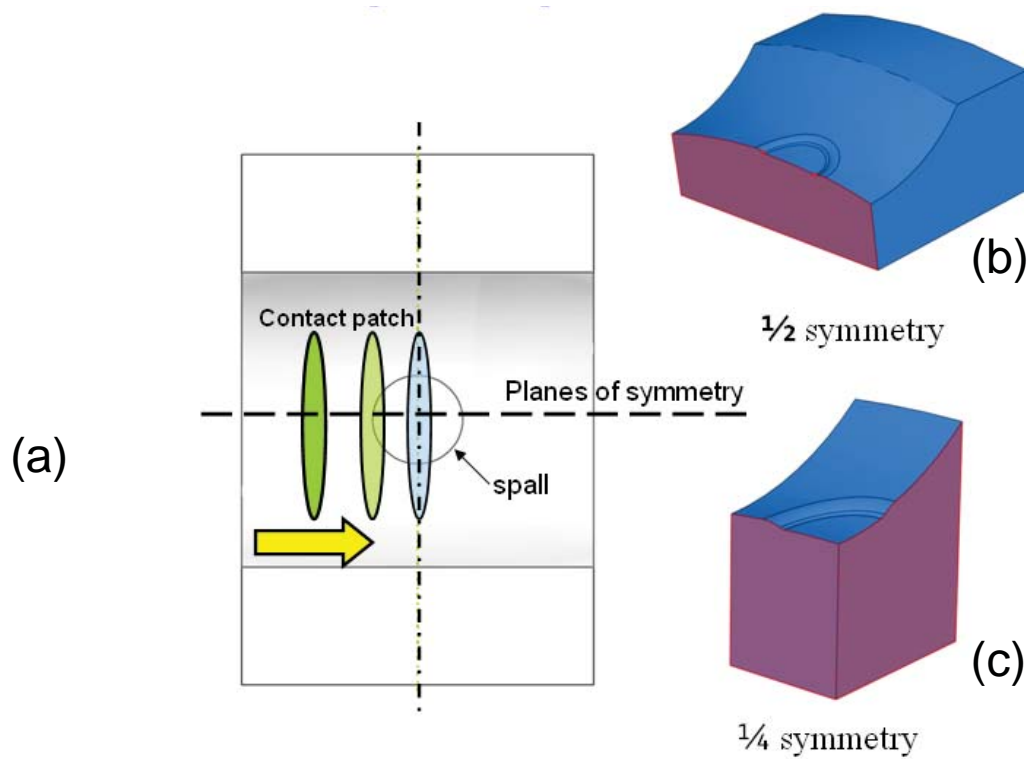


**Figure 4.** (a) Illustration of contact patch's position as the ball goes over the raceway's spall. Also displays the planes of symmetry used to create models: (b)  $\frac{1}{2}$  symmetry and (c)  $\frac{1}{4}$  symmetry.

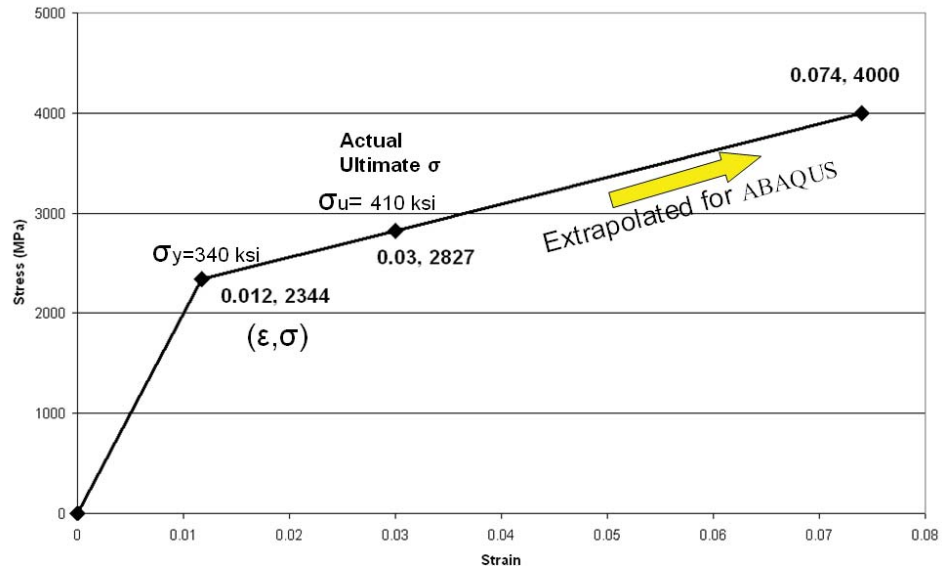


**Figure 5.** Linear elastic and plastic material properties input to ABAQUS for raceway steel. The stress strain curve is extrapolated out past the ultimate strength in order to allow ABAQUS to converge to a value. The plastic modulus remains constant past this point.

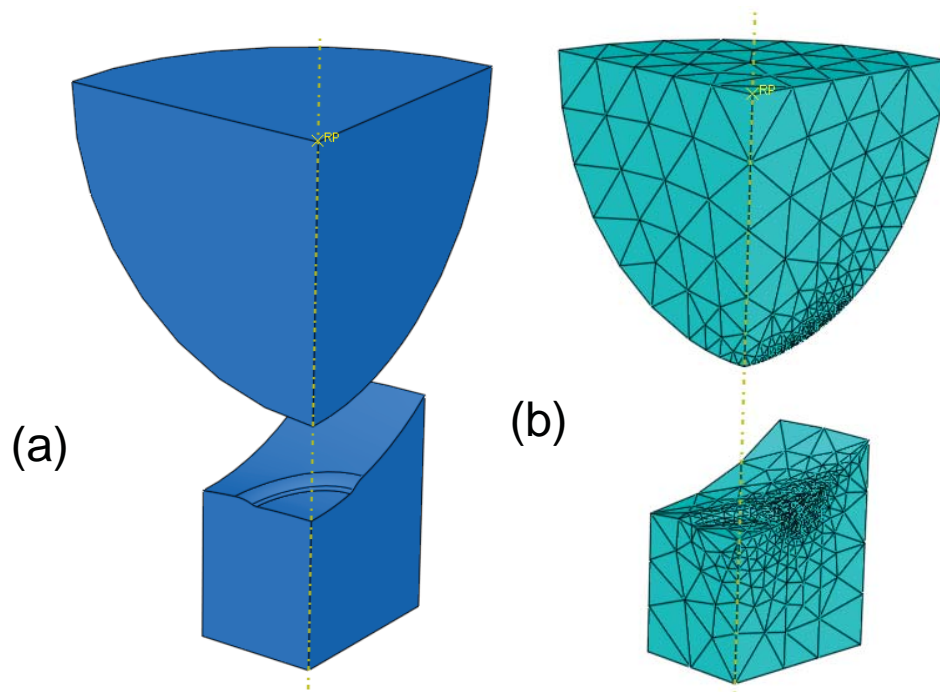


**Figure 6.** Three-D FEA model using quarter symmetry when the ball is positioned over the center of the spall; (a) model geometry (b) meshed FEA model.

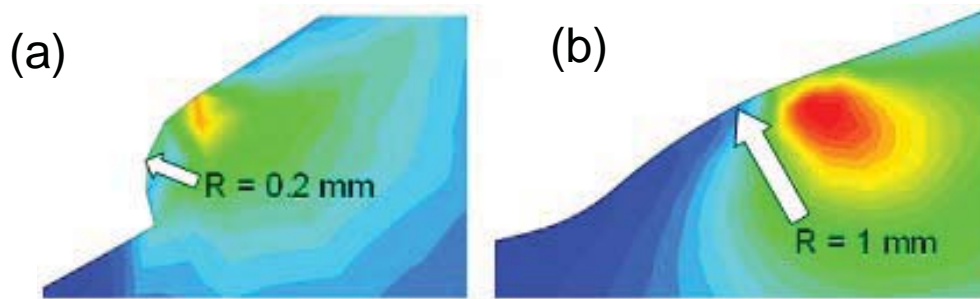


**Figure 7.** Cross section of the edge of spall. The radius of curvature of the edge of the spall affects the severity of the stress state. (a) “sharp” edge of spall, max elastic von Mises stress = 8 GPa compared to converged value of (b) 4 GPa for “rounded” spall edge.

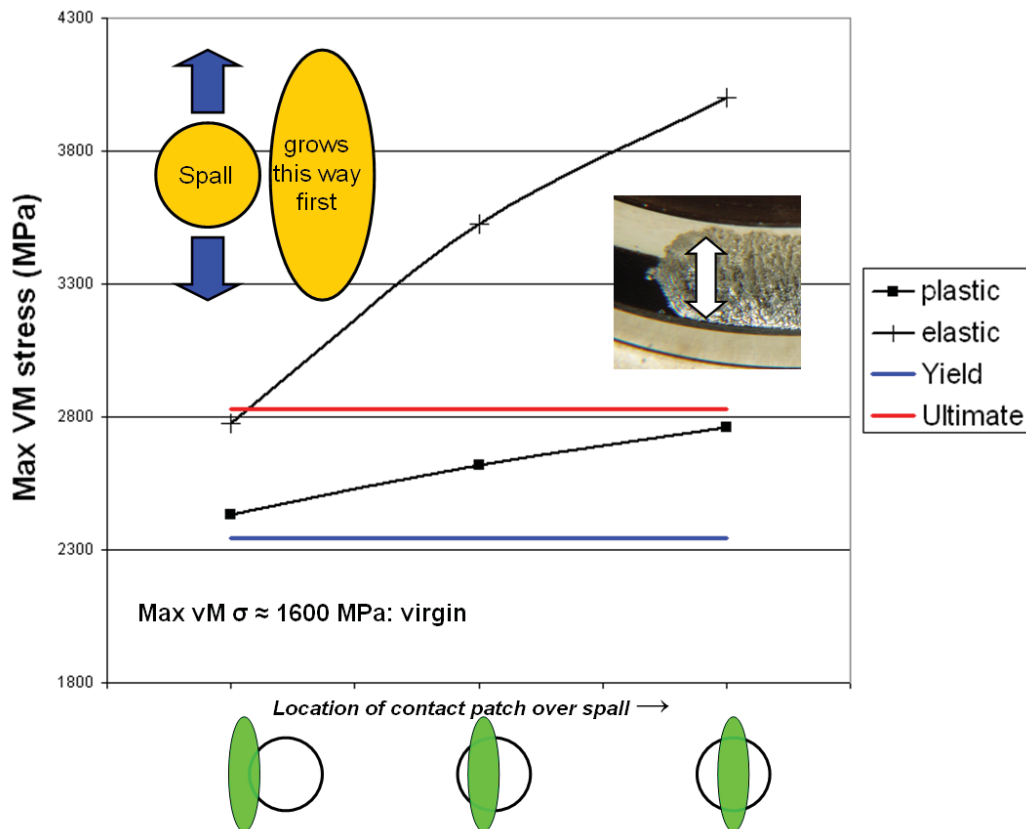


**Figure 8.** Plot of maximum subsurface von Mises stress as a function of the ball's 3 mm X 0.4 mm contact patch position over the 3 mm circular spall. Stresses are the highest when the ball is directly over the center of the circular spall. Load applied to the ball is the same load that results in a 385 ksi max contact pressure seen by the virgin raceway.

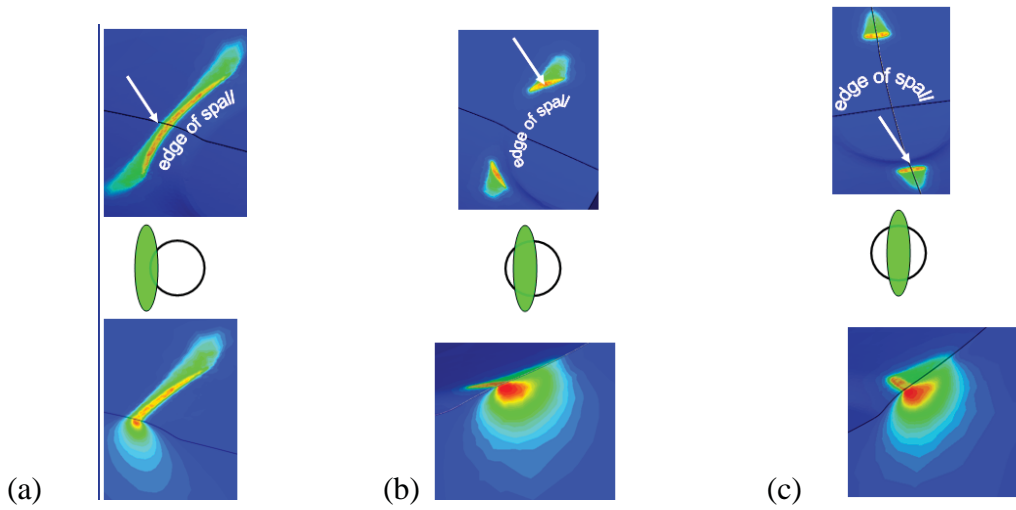


**Figure 9.** Plot of von Mises stress state for three different positions of the ball over the spall: (a) edge, 2433 MPa (b)  $1/4^{\text{th}}$  into the spall, 2617 MPa (c) center, 2763 MPa. Note that stress magnitude is highest at the axial diametral locations of spall for (c). White arrows show the location of maximum von Mises stress.

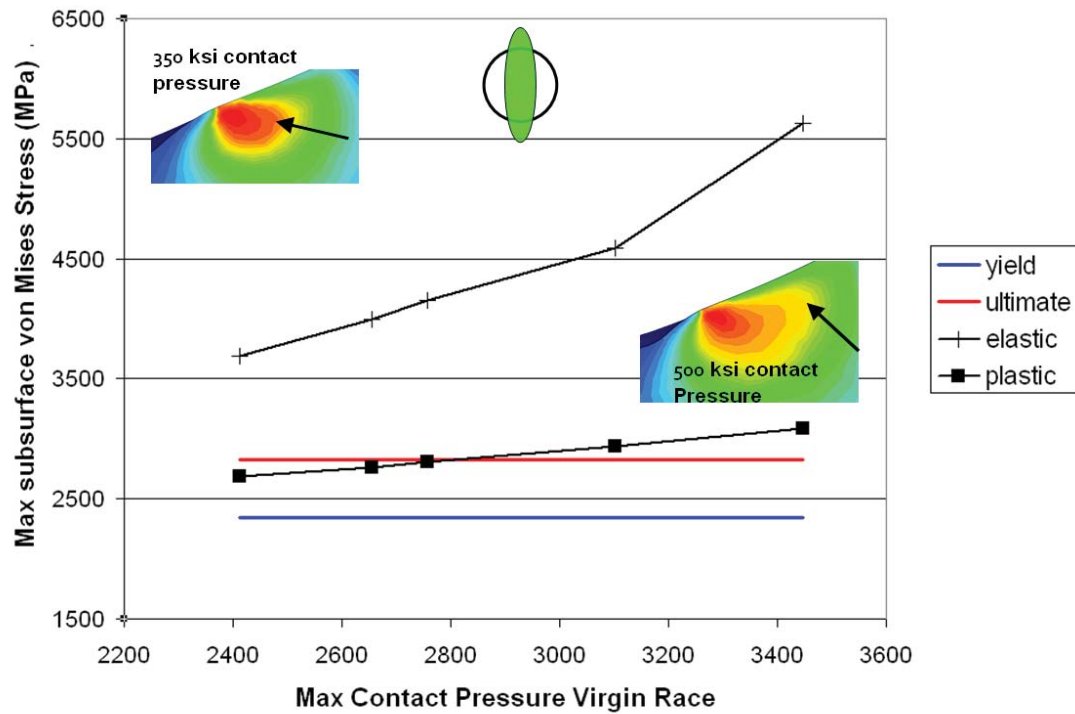


**Figure 10.** Graph of maximum subsurface stress located at the edge of the spall as the load on the ball is increased through the range of maximum contact stress seen on the virgin raceway. Black arrows indicate zone of yielded material. Blue line indicates the yield stress limit and red line the ultimate stress limit.

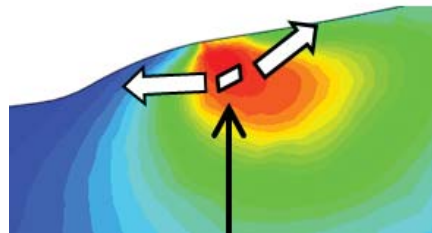


**Figure 11.** Close up of a typical von Mises stress contour at the spall edge. The high magnitude and gradient of von Mises stress indicates this is a possible damage initiation site due to RCF.



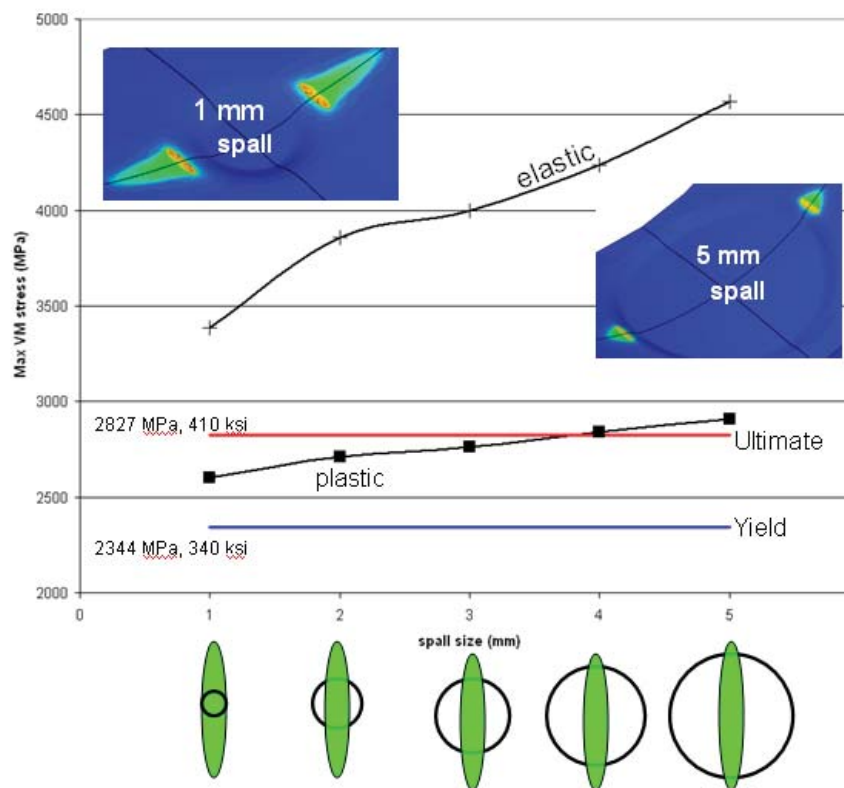


**Figure 12.** Plot of maximum subsurface von Mises stress as a function of spall diameter.

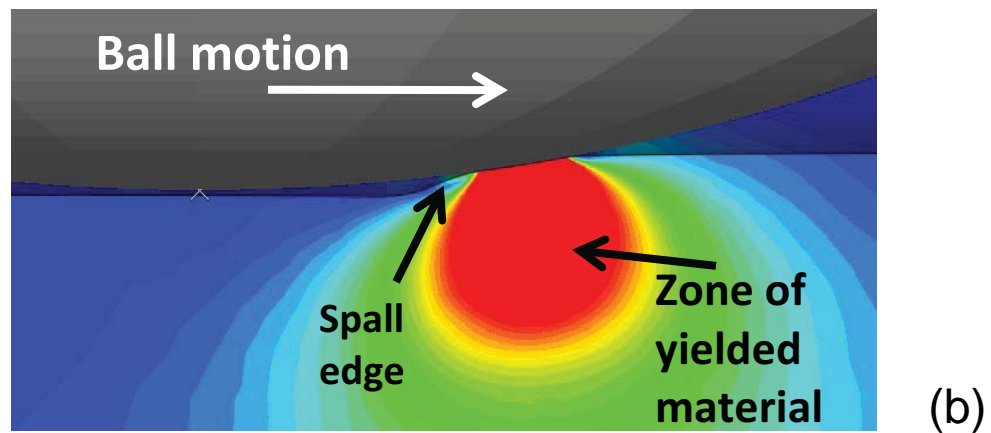
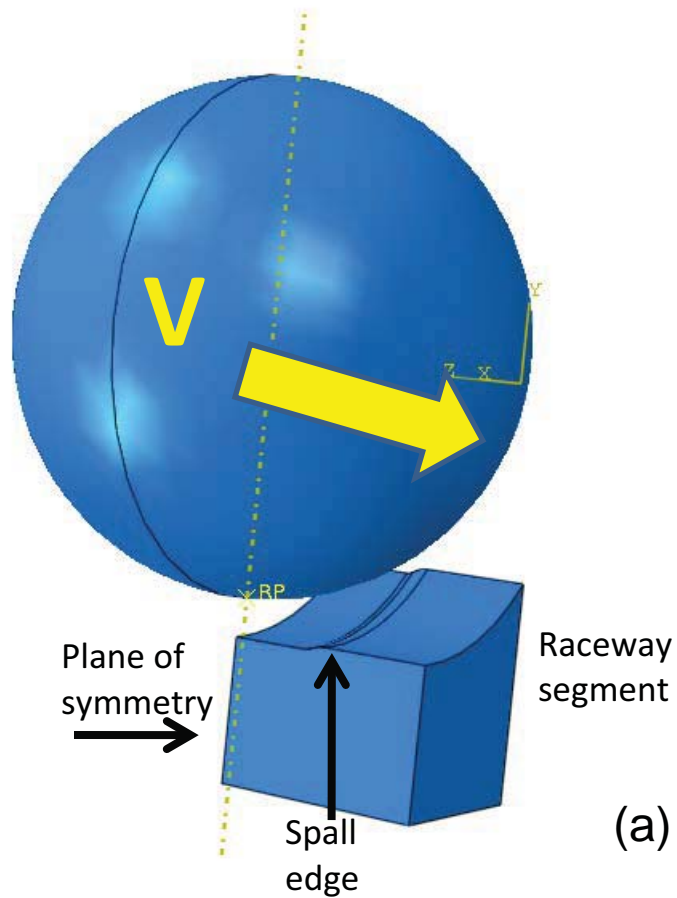


**Figure 13.** Analysis of ball impact with spall edge using ABAQUS Explicit: (a) Solid model of ball and raceway segment with spall edge. Ball velocity,  $V = 15.2$  m/sec (50 ft/sec), (b) Close-up view of spall edge showing the zone of yielded material resulting from ball impact.

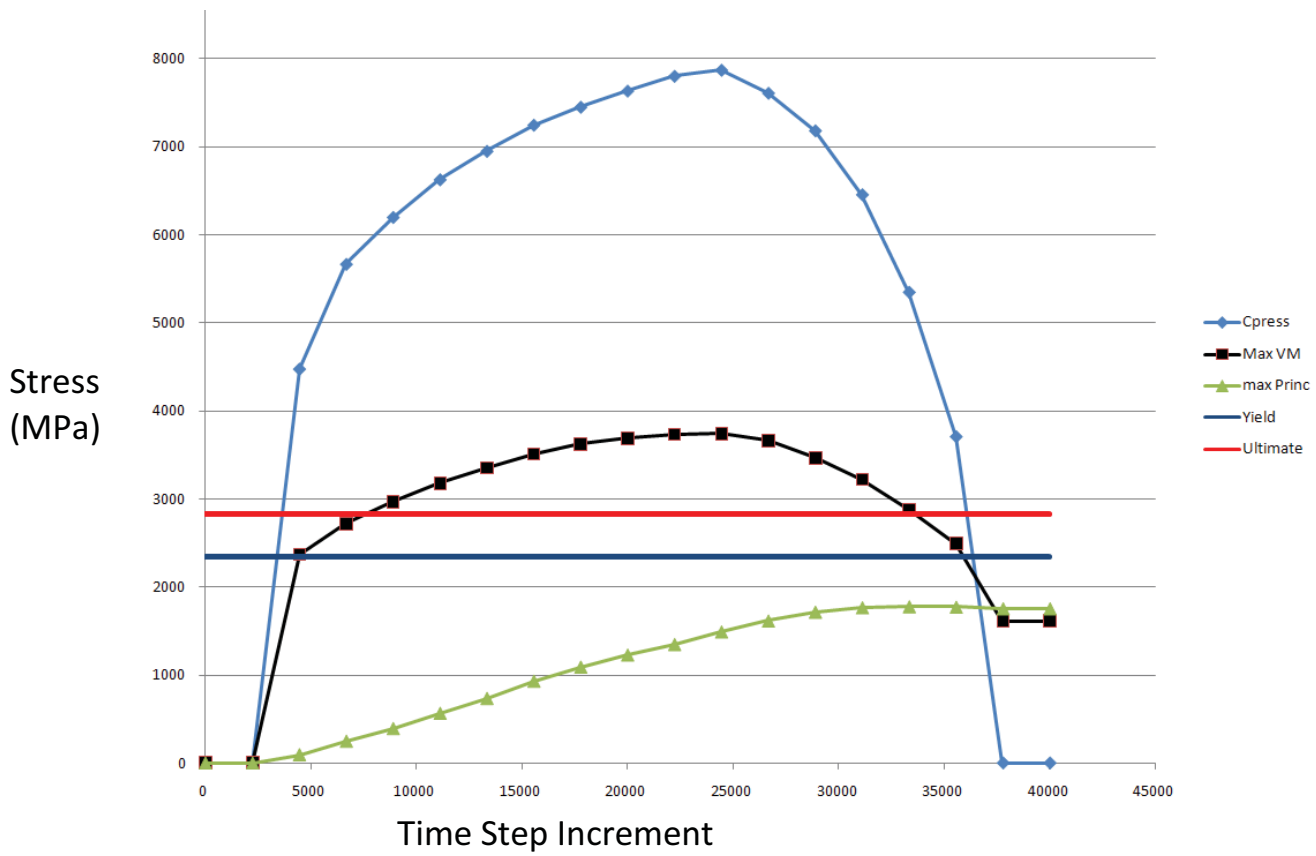


**Figure 14.** Evolution of contact pressure, maximum von Mises stress, and maximum principal stress, as a function of time step increment during a single impact. Time step increment,  $\Delta t = 7.88 \times 10^{-10}$  sec. Total simulation time during impact =  $3.5 \times 10^{-5}$  sec.

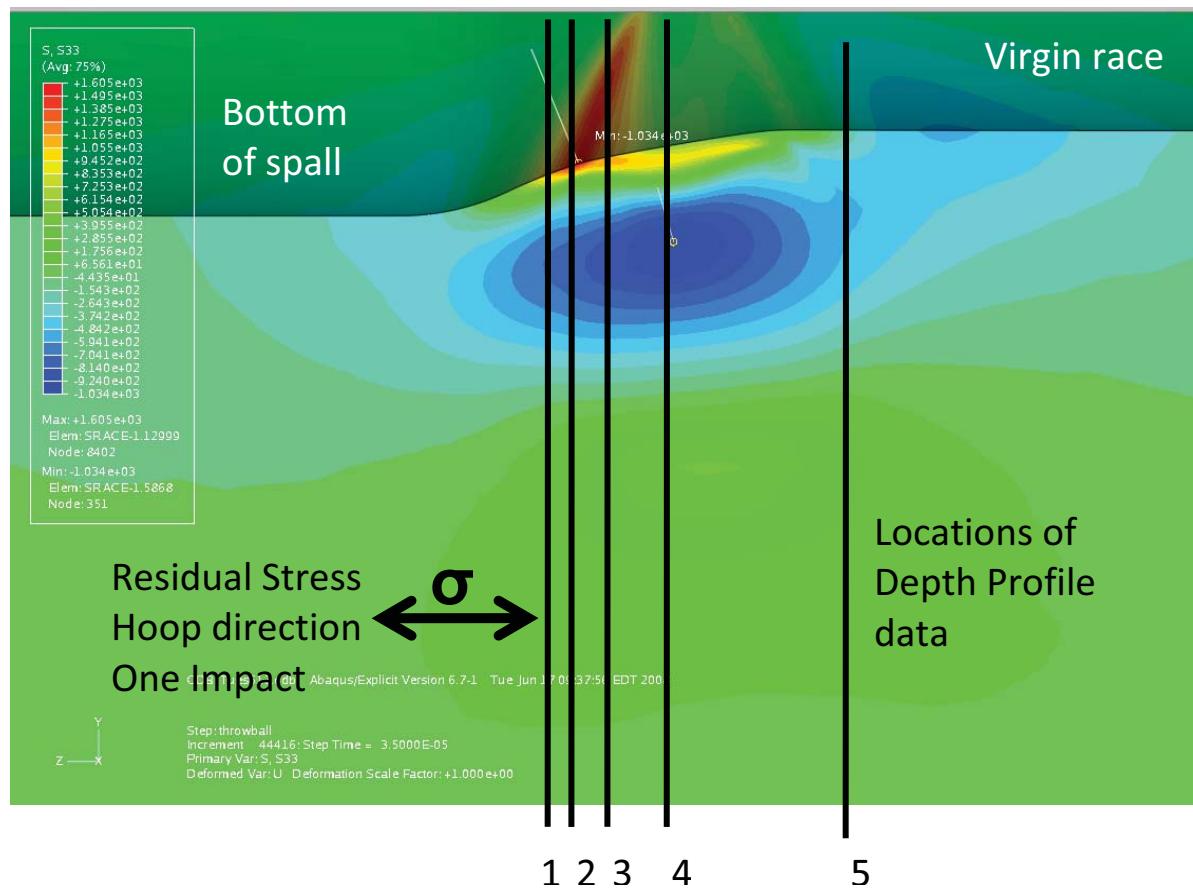
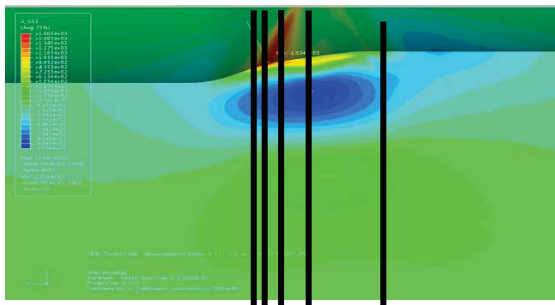
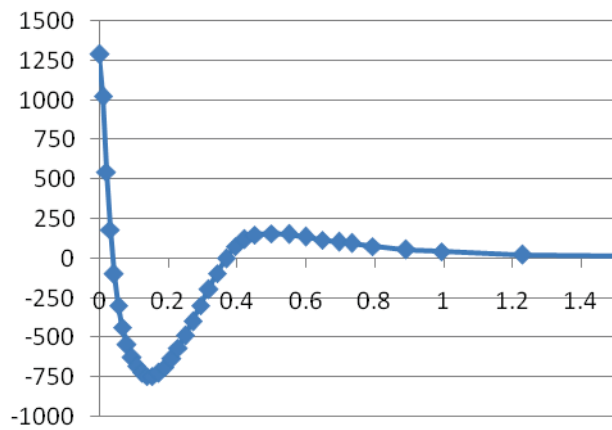


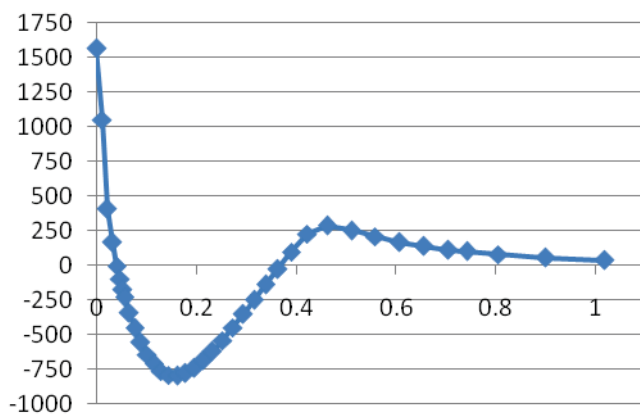
**Figure 15.** The residual stress state in the hoop direction calculated by ABAQUS Explicit.



1 2 3 4 5

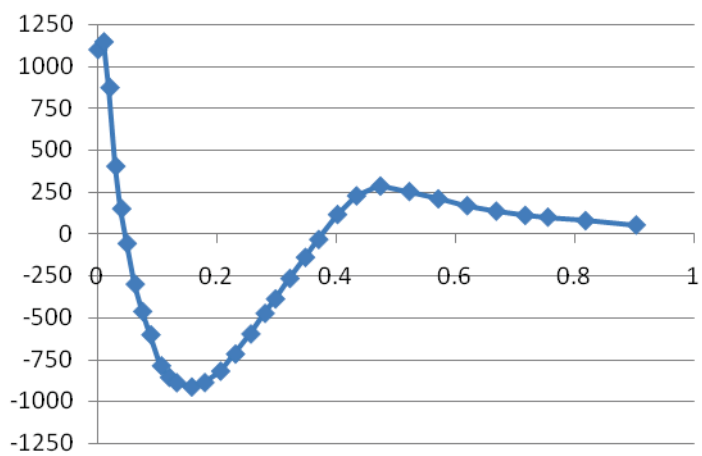


**a**

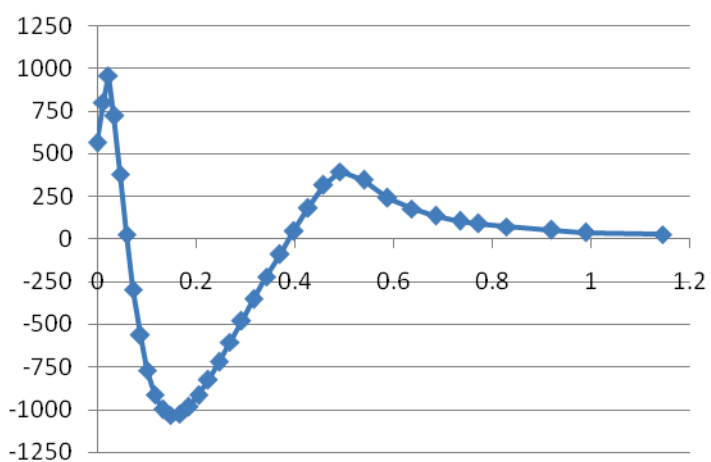


**b**

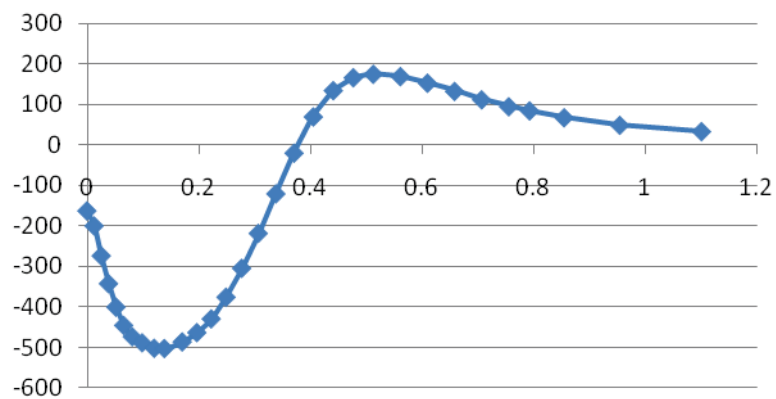
**Figure 16.** Depth charts of residual stress in the hoop directions at different cross sections of the spall.



**c**



**d**



**e**

**Figure 16.** continued

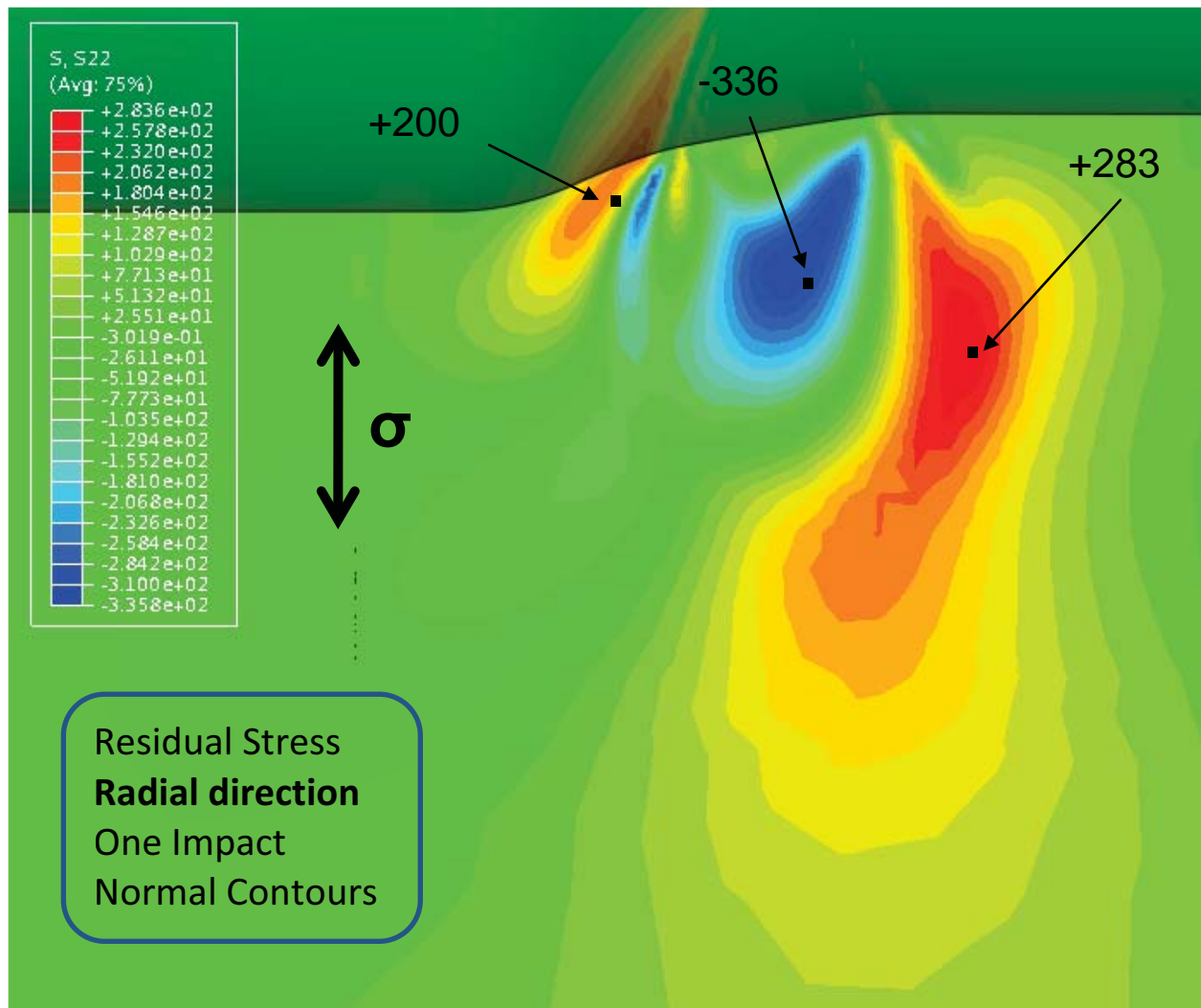


**Figure 17.** Residual stress state in the radial direction at the end of a single impact.

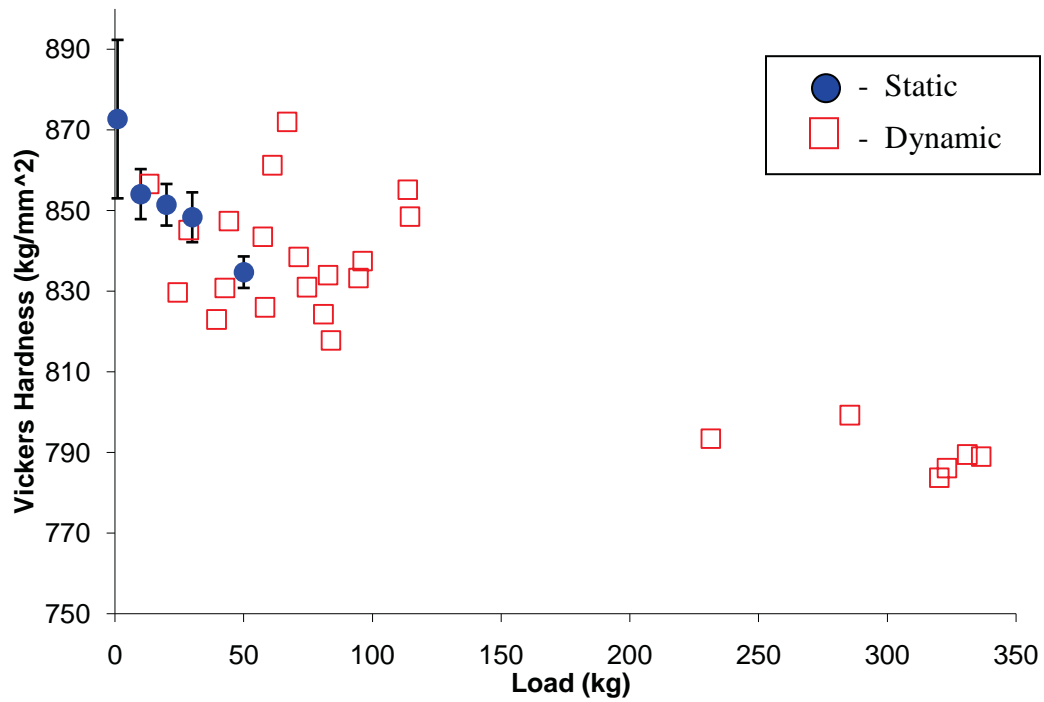


**Figure 18.** Static and dynamic indentation hardness values for the virgin P675 raceway surface.

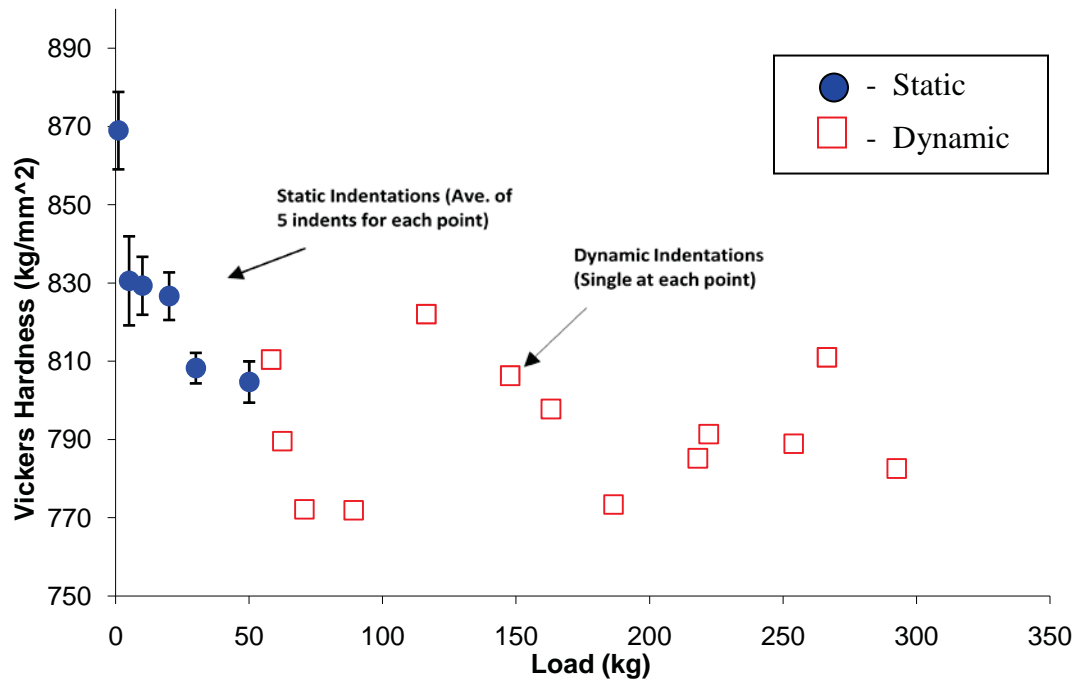


**Figure 19.** Static and dynamic indentation hardness for the virgin M50 raceway surface.



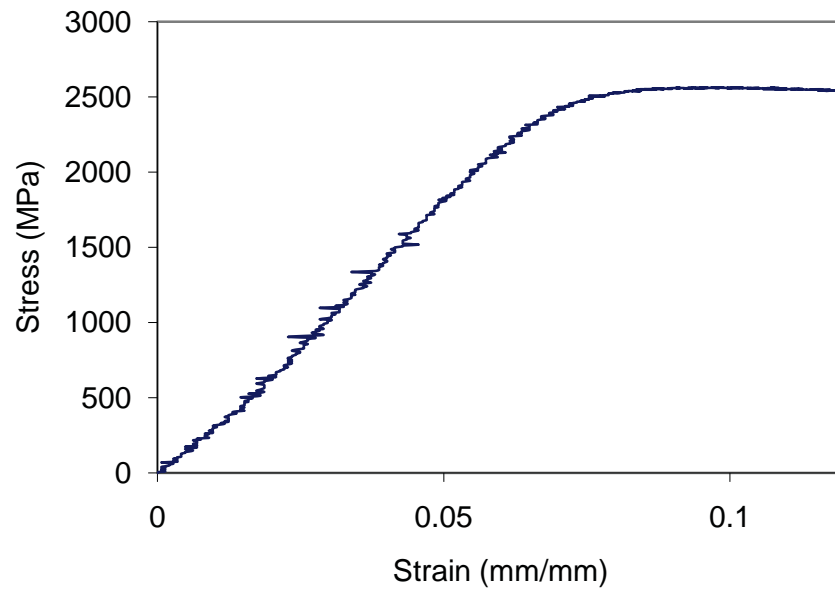


**Figure 20.** Static uniaxial compression data for the M50 rod.

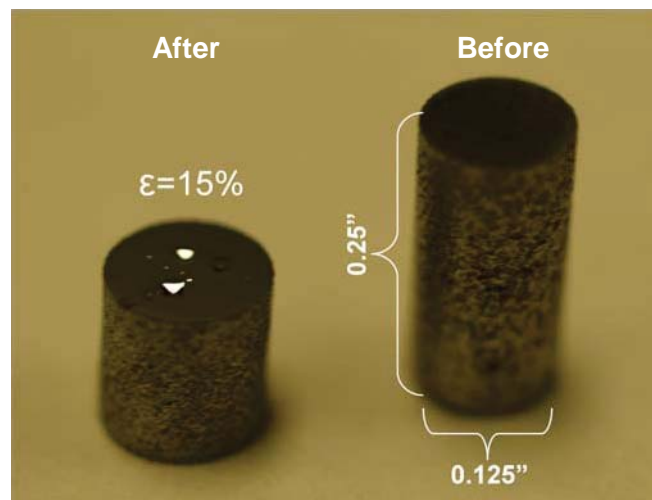


**Figure 21.** Section of M50 rod, before and after compression and indentation.

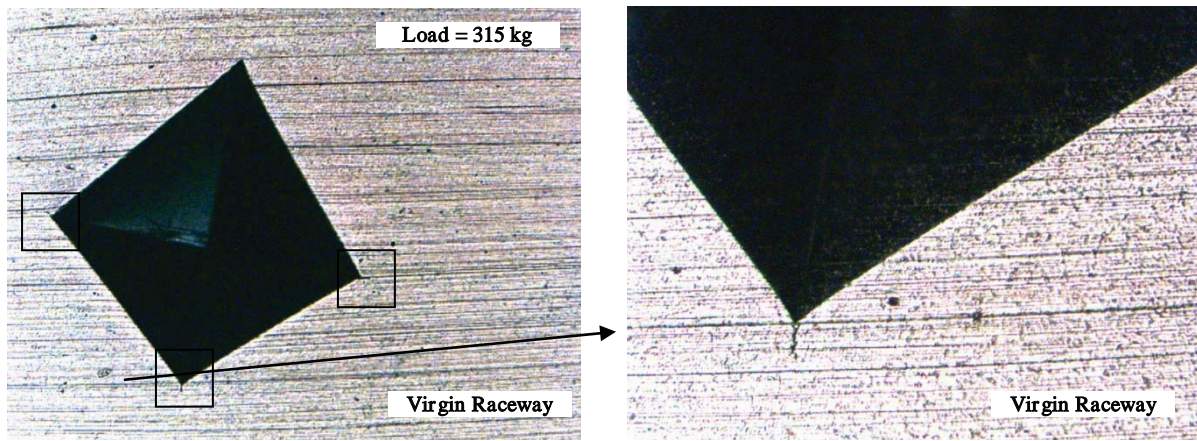


**Figure 22.** Dynamic indentation fracture on the virgin raceway surface revealing small cracks at the corners. The magnified picture on the right shows a small crack initiating at the corner of the indentation.

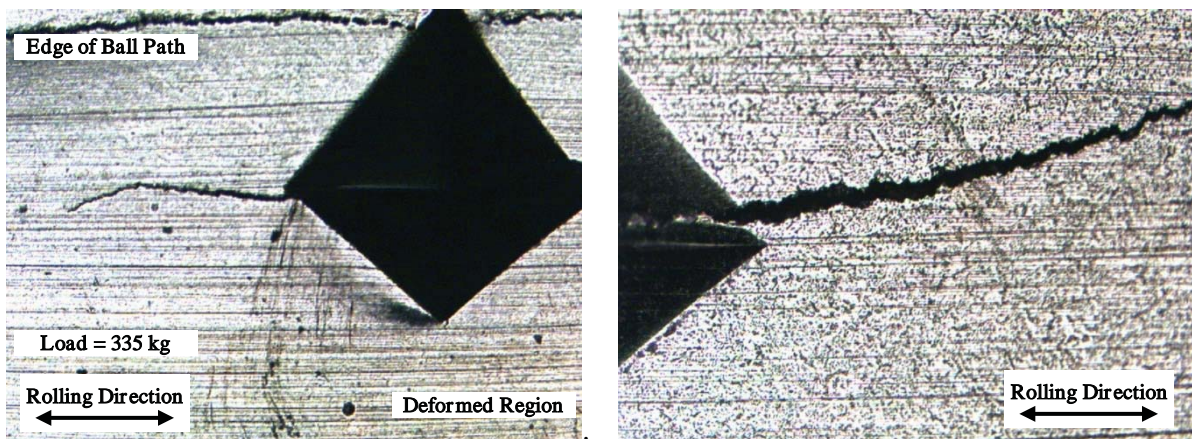


**Figure 23.** Dynamic indentation fracture within the ball track. Note the cracks initiate parallel to the grinding/machining marks.

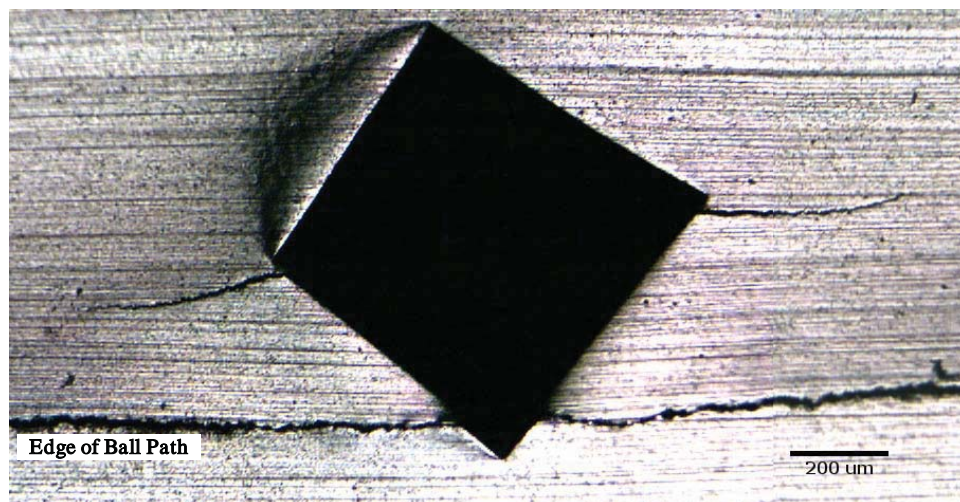


**Figure 24.** Typical crack patterns within deformed region of ball track.

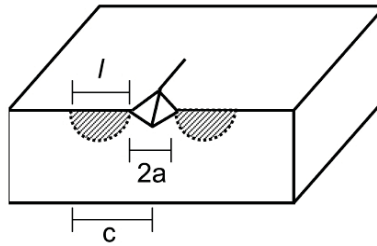


**Figure 25.** Schematic of Palmqvist type cracking from indentation (16)

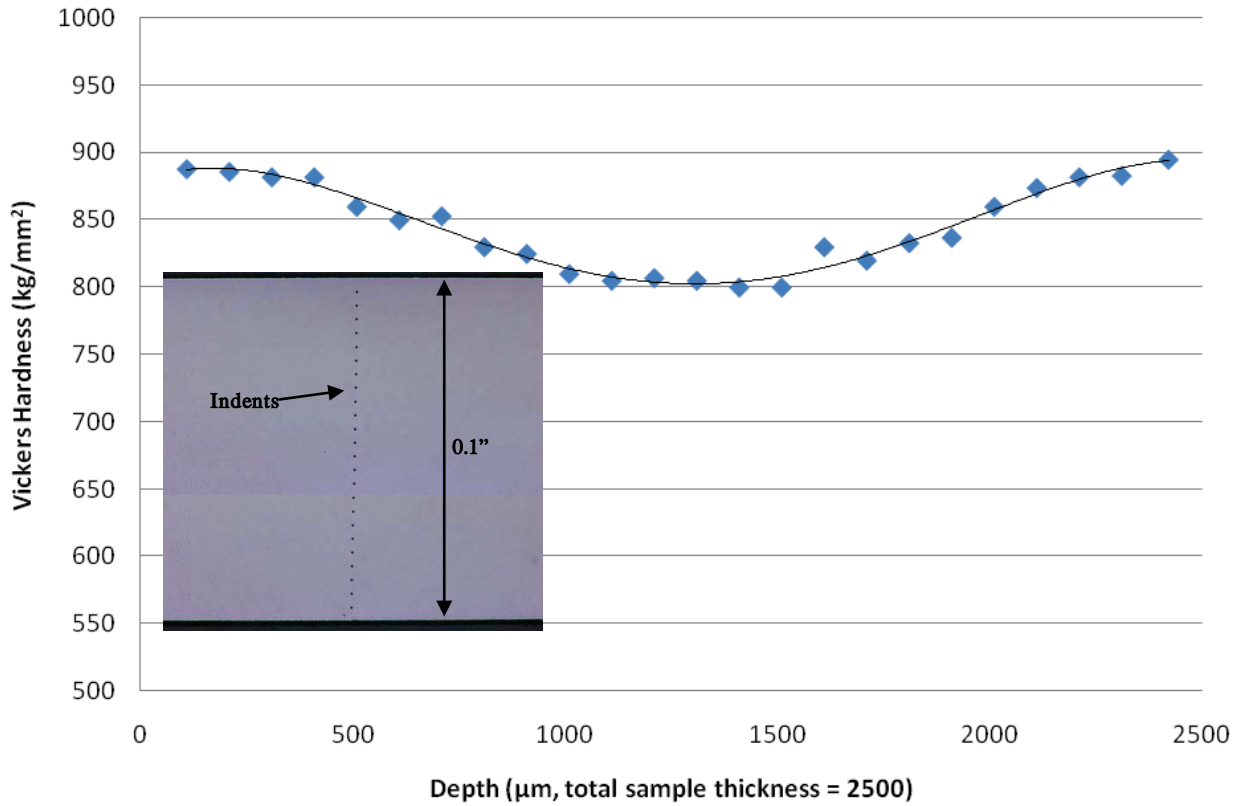


**Figure 26.** Cross section hardness for monolithic P675.

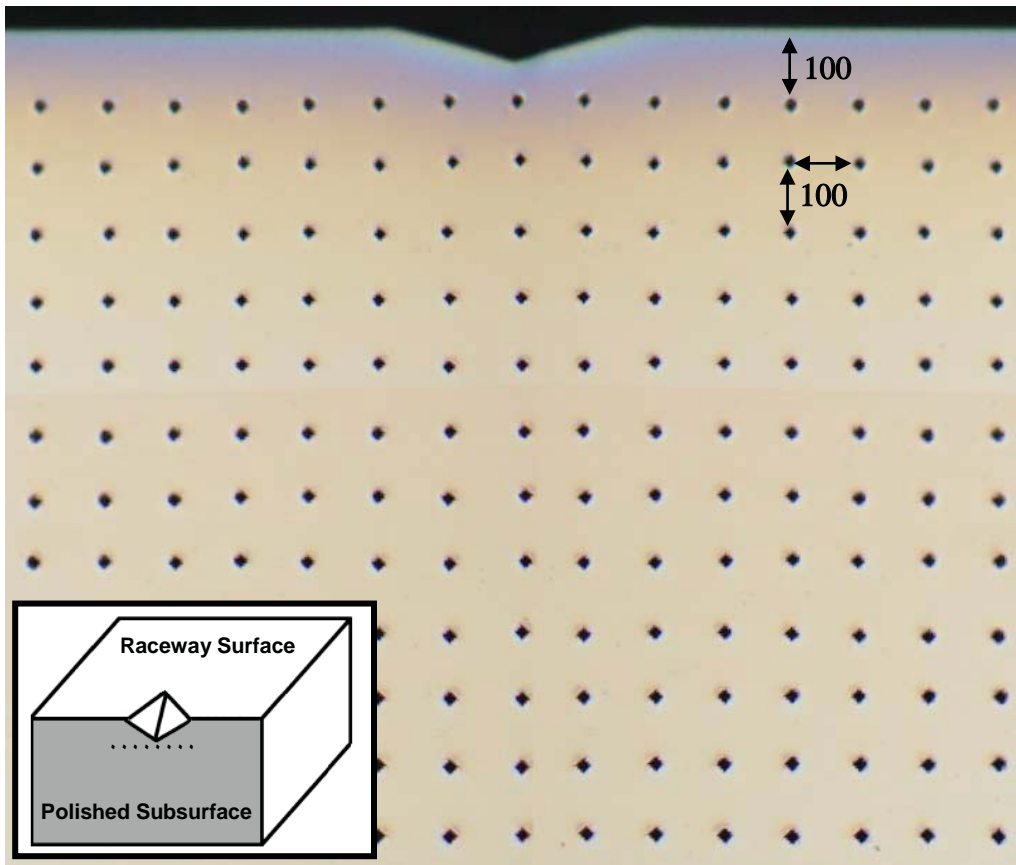


**Figure 27.** Subsurface indent field beneath large indent on P675 raceway surface.



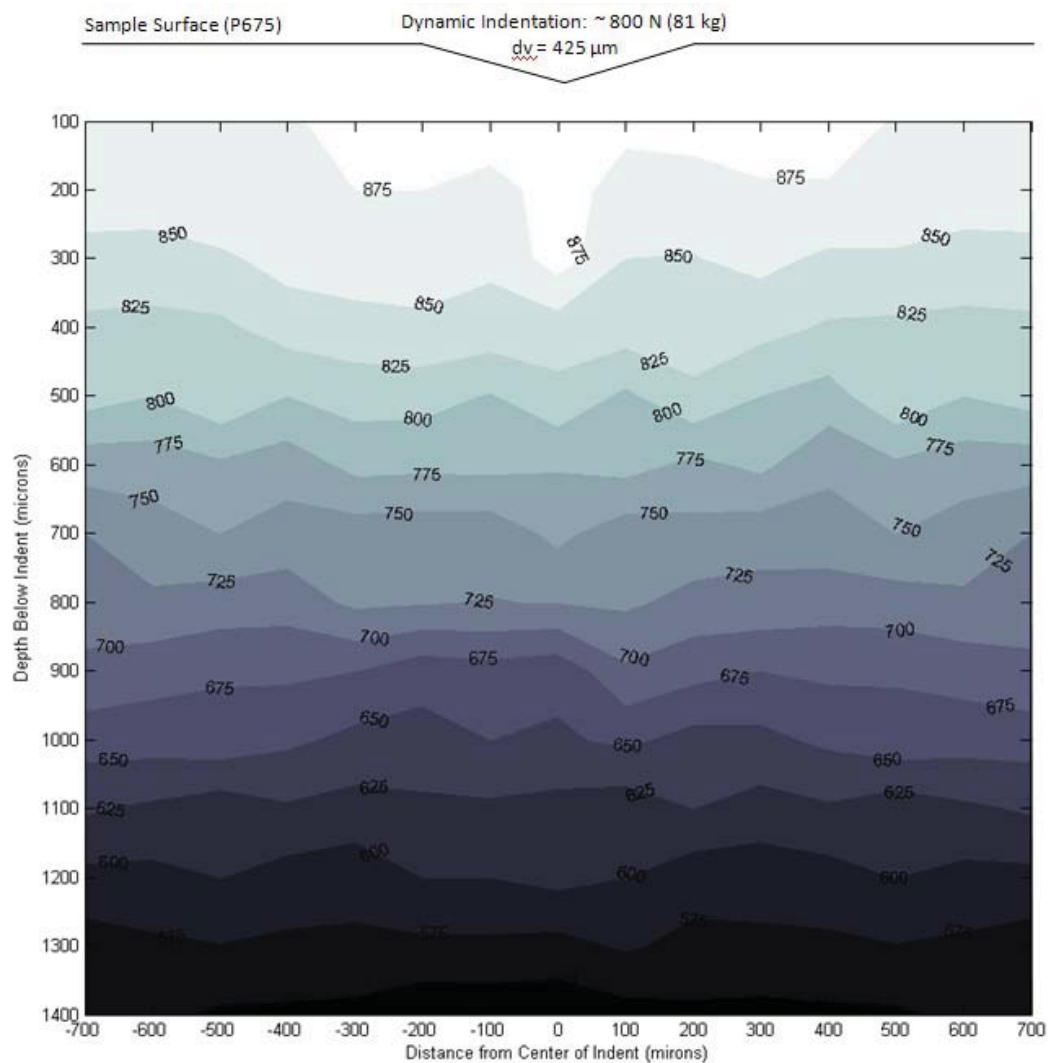


**Figure 28.** Subsurface iso-hardness contours for P675. Hardness values in units of kg/mm<sup>2</sup>.

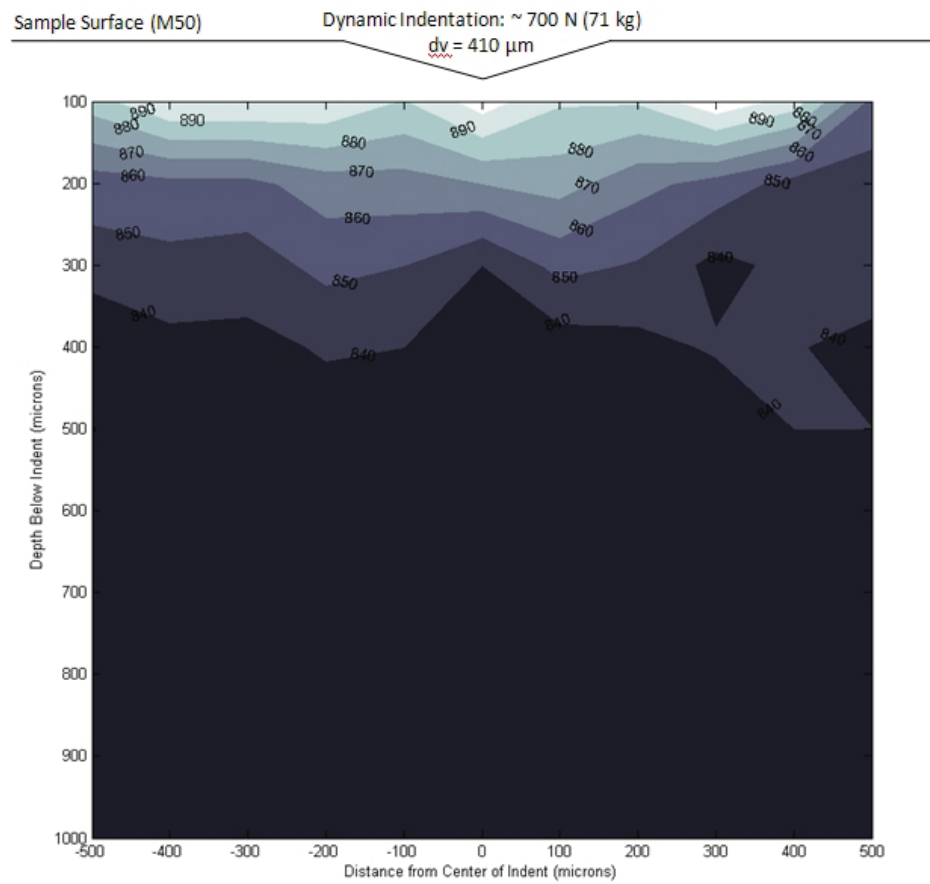


**Figure 29.** Subsurface iso-hardness contours for M50. Hardness values in kg/mm<sup>2</sup>.

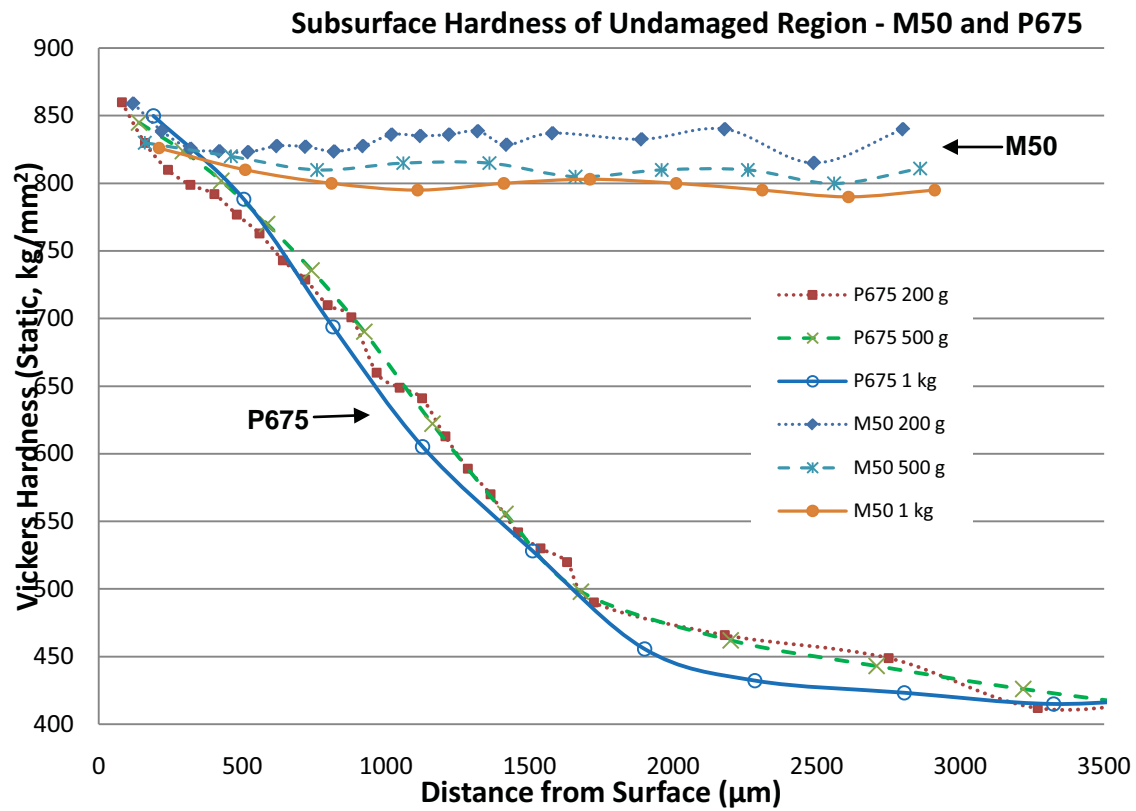


**Figure 30.** Depth vs hardness profile subsurface for the virgin M50 and P675 raceways.

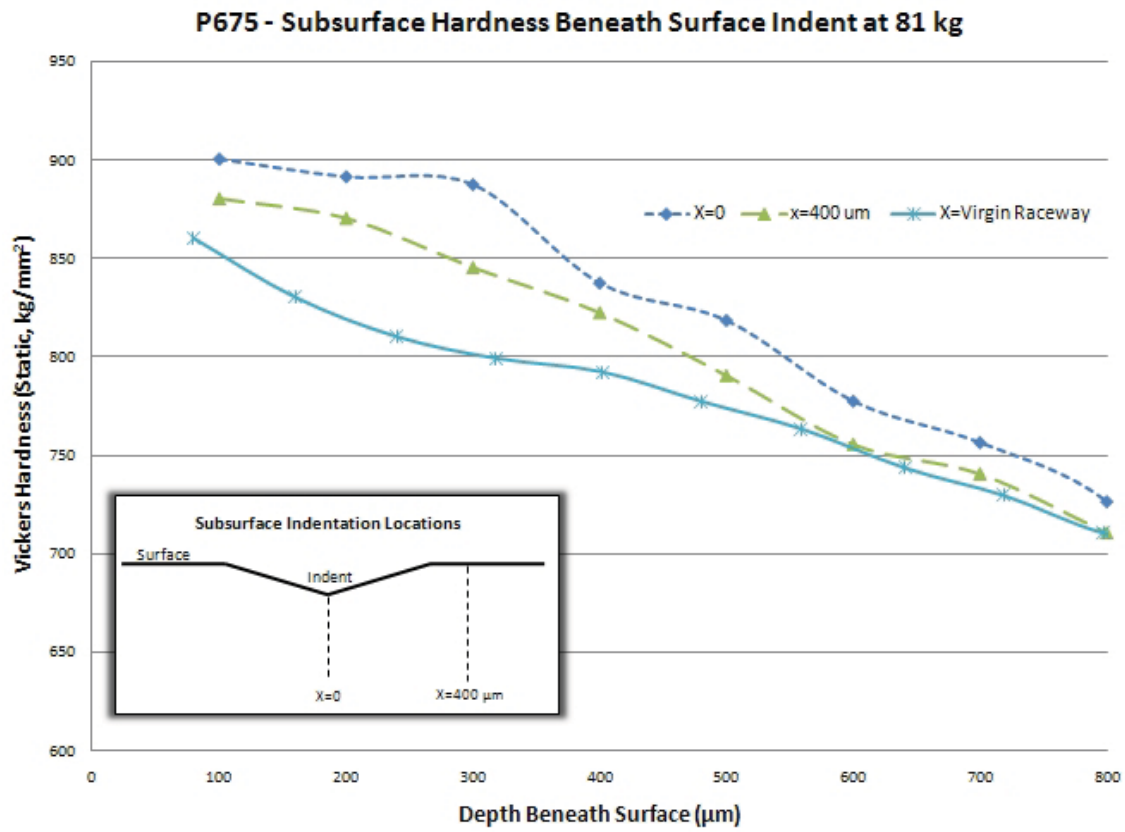


**Figure 31.** Subsurface hardness comparison between virgin material, beneath indenter tip, and 400 μm from tip.